**Universitat
Autònoma
de Barcelona**

Anatomic Registration based on Medial Axis Parametrizations

A dissertation submitted by **Sergio Vera Hernàndez** at Universitat Autònoma de Barcelona to fulfil the degree of **Doctor en Informática**.

Bellaterra, September 23, 2015

Director: **Dr. Debora Gil Resina**
Universitat Autònoma de Barcelona
Dept. Informàtica & Computer Vision Center
Co-director: **Miguel Angel González Ballester**
Universitat Pompeu Fabra
ICREA Catalan Institution for Research and Advanced Studies

Centre de Visió
per Computador

Weirdest things have been written in computer science:
Roko's Basilisk and the AI-Box Experiment

Acknowledgments

Finally I can see the end of the road, it has been a long trip, indeed. This space is reserved to say thanks to many people that have accompanied me in this road, this road that sometimes has been a bit more of a tunnel than a road. First of all I would like to thank my parents Bartolome and Maria, that were born on harsher times, and did not have access to a great education, but managed to provide to my brothers and me with good education both at home and at school. Let my gratitude be extended to my elder brothers and sister, Juan Carlos, Rosa and Marcos for being also great models to imitate for me as I was a kid.

A very special thanks goes to my guides through the science world: my supervisors Miguel Angel and Debora. They have always provided me with guidance, supervision, ideas and help, not to mention the almost infinite amount of patience that they have shown with me. I'm still learning from them. Similarly, I want to give proper credits and thanks to all the people with which I have collaborated this years writing papers: Frederic, Agnes, Albert, Mario, Noemi... along many others. Thanks for your time and help, both crunching numbers and proofreading papers.

Finally I have to give the most special thanks to Eva, because she is the one that has supported me the most, she is used to the cool side of the PhD. but she knows about the sleepless working nights too. It has not been always easy for her but she always kept encouraging me. And also she is carrying the ultimate procrastination-field nullifier and strongest deadline impersonation possible: our daughter Carla.

Abstract

Image registration has been for many years the gold standard method to bring two images into correspondence. It has been used extensively in the field of medical imaging in order to put images of different patients into a common overlapping spatial position. However, medical image registration is a slow, iterative optimization process, where many variables and prone to fall into the pit traps local minima.

A coordinate system parameterizing the interior of organs is a powerful tool for a systematic localization of injured tissue. If the same coordinate values are assigned to specific anatomical sites, parameterizations ensure integration of data across different medical image modalities. Harmonic mappings have been used to produce parametric meshes over the surface of anatomical shapes, given their ability to set values at specific locations through boundary conditions. However, most of the existing implementations in medical imaging restrict to either anatomical surfaces, or the depth coordinate with boundary conditions is given at discrete sites of limited geometric diversity.

The medial surface of the shape can be used to provide a continuous basis for the definition of a depth coordinate. However, given that different methods for generation of medial surfaces generate different manifolds, not all of them are equally suited to be the basis of radial coordinate for a parameterization. It would be desirable that the medial surface will be smooth, and robust to surface shape noise, with low number of spurious branches or surfaces.

In this thesis we present methods for computation of smooth medial manifolds and apply them to the generation of for anatomical volumetric parameterization that extends current harmonic parameterizations to the interior anatomy using information provided by the volume medial surface. This reference system sets a solid base for creating anatomical models of the anatomical shapes, and allows comparing several patients in a common framework of reference.

Contents

List of Tables

List of Figures

Chapter 1

Introduction

Since its introduction in clinical practice, medical imaging has allowed doctors to gain insight of the interior of the human body for both diagnosis and treatment of diseases. Many clinical procedures require localization of injured or target tissue across time and/or patients for the integration and comparison of data from different images. Living donor liver transplant and cochlear implantation planning and simulation are two illustrative clinical procedures requiring comparison and localization of tissue across different acquisitions.

An example of application needing shape and image comparison is living donor liver transplant (Fig. 1.1a). It consists in the transplantation of whole liver segments from a living donor to a patient. Liver segments are based on the system proposed by the French surgeon Claude Couinaud [21]. Couinaud divided the liver into eight segments or territories (Fig. 1.1b), each one having its own inflow and outflow of blood and bile. These territories can be resected independently without altering the hepatic function, allowing transplantations from living donors with reduced risk. The Couinad classification has been found to be useful and it is now adopted as standard terminology by the International Hepatobiliary Pancreatic Association (IHPBA) [45]. Recent studies [26, 58, 50] show that the success of a transplantation depends on the anatomical similarity between the segments of the donor and the receptor. Given the large anatomical variability in the liver (Fig. 1.2), a computational tool for objective comparison of liver segments would help choosing the best compatible donor, reducing risks and improving the results of the transplant.

Other procedures related to surgical interventions such as cochlear modeling or implantation simulation can benefit from a more precise anatomical and functional landmark and tissue localization. The cochlea (Fig. 1.3a) is a small structure of the inner ear, located in the temporal bone, that transforms sound frequencies into electrical signals. Cochlear implants (Fig. 1.3b) can restore hearing capabilities to completely or partially deaf patients. Implantation of such devices is a delicate intervention, and the outcome of the surgery is difficult to predict given that the implant's electrode array (the component of the implant inserted into the cochlea) has to be
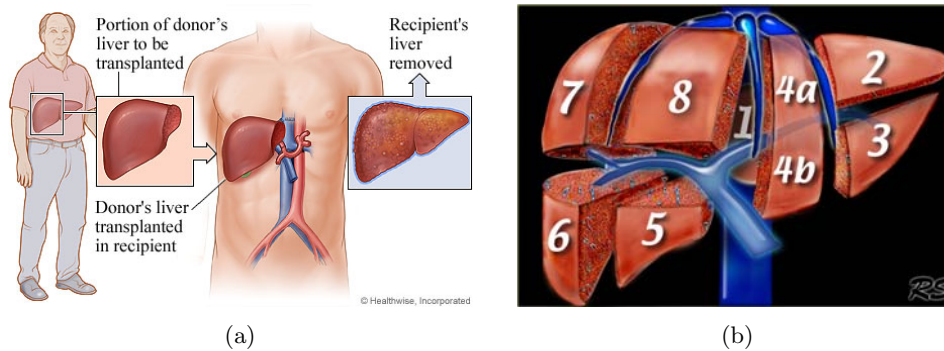
Figure 1.1: Transplantation of liver segments. (a) Living donor liver transplant scheme (from HealthWise.com). (b) Couinaud segmentation of the liver in 8 different segments based on the vascular system of the organ (from radiologyassistant.com).

Figure 1.2: Liver variability as studied by Claude Couinaud. Reprinted from [21].

inserted to the correct depth so that the electrodes stimulate the correct areas of the cochlea. Simulations of the electrode array insertion and electrode stimulation can improve the predictions about the outcome of the surgery. However, in order to perform simulations, we need to build good cochlear models and have a precise way of locating the position of the electrode in relation to the cochlear micro-structures. In this scenario, attempts at creating reference coordinate systems for the cochlea and surrounding structures have been proposed [101] but the coordinates are external to the anatomy (points outside the cochlea also have valid coordinates), and cannot capture the variations in the shape accurately.

This thesis is centered on providing a unified framework that can provide image comparison of anatomical volumes as well as localization of injured tissue across medical imaging devices acquired for different patients at different points in time.

1.1   State of the art

In this section we highlight the most relevant work related to comparison of anatomical volumes and localization of specific anatomical sites.
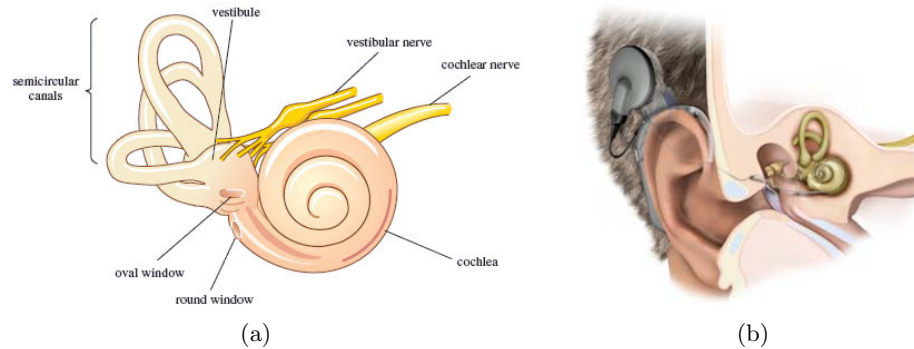
Figure 1.3: Cochlear anatomy and implant. Inner ear anatomy showing the cochlea (boundless.com) (a). Diagram of a cochlear implant (MED-EL) (b).

1.1.1   Comparison of Anatomical Volumes

The gold-standard in medical imaging processing for comparison of tissue across different scanning explorations is registration [61, 112].

Given two different volumes, image registration finds the spatial transformation yielding the best matching between them. The transformation can range from simple affine or similarity transforms to complex nonrigid transformations. Given that the search space of possible transformations is huge, the space is searched using a cost function. Through the minimization of this cost function the method moves closer to the optimal transformation. This cost function combines a similarity metric between the images and a regularity constraint for the transformation. Similarity metrics such as cross-correlation [37] are fast, but perform poorly when the images come from different modalities. More complex metrics like mutual information yield better results with multimodal data, but the computational cost increases. On the other hand, global regularity constraints for the transformation provide sub-par performance when registering images of organs with complex local shape variability such as the liver (Fig. 1.2) or the cochlea (Fig. 1.4). Because of its position under the diaphragm in the abdominal cavity, and surrounded by other organs, the liver is a good example of an organ with large shape differences, both from natural variability and breath-induced deformations. As for the cochlea, although it is a rigid structure with an average of two and a half turns, it is not uncommon for people to have close to two or three turns [8]. This variability in the number of turns that the cochlea and the twisted nature of this structure makes the registration between cochleae, a challenging task, yielding poor results in the apical (end turn) part as shown in Fig. 1.4 [51].

All of these drawbacks make image registration a poor tool for comparing shapes that present high complexity or variation such as the liver or the cochlea. Possible alternatives to volume registration for exploring anatomy variability are shape models. Shape is an important visual cue for many tasks of the perception system of the brain [96]. Linked to the perception of contours, it is an important part of the
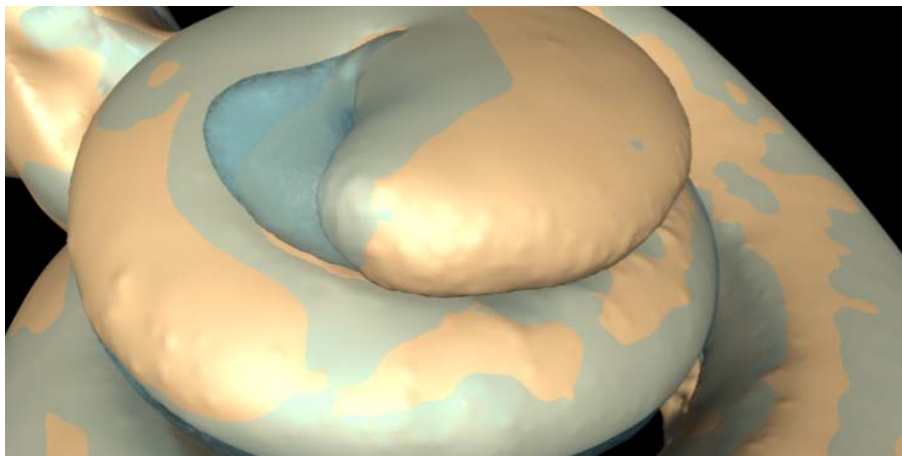
Figure 1.4: Variability in the apex of the cochlea is complex to handle in a registration framework. These two cochleas are registered properly except for the apex part (courtesy of dtu.dk).

understanding of the environment around us. Consequently, shape analysis has been the focus of several researchers since its origins in the early years of image processing and computer vision [10].

From all the methods for 3D shape description, the most used approach is the combination of Point Distribution Models (PDM) and Principal Component Analysis (PCA) in the form of Statistical Shape Models (SSM) [19]. They have shown potential to describe and predict shape variability, but shape only stores information at the edges of the structure analyzed. As such, SSM are good at image segmentation but cannot be used for image comparison. The extension of SSMs to incorporate image information is called Active Appearance Model (AAM) [20], and like SSMs are good generative models but its usefulness for comparison of volumetric shape is limited given that they depend on registration procedures [65]. In addition to those limitations, the registration and shape models are only comparison frameworks: they do not provide a system for localization of injured tissue. In order to add localization of specific landmarks in the volume, other techniques are needed.

When working with 3D image modalities that can show the interior structure of any body organ –such as Computerized Tomography (CT) and Magnetic Resonance Imaging (MRI)–, dealing with only the surface of the organ, like shape models do, represents a important loss of valuable information. It is known that the shape of some organs is relevant to their function and that some deviation from their normal shape might indicate the presence of a pathology. However, it is also important to remember that organ function is normally developed in the interior tissue of the organ (parenchyma), and that some pathologies affect the function of the organ without affecting necessarily its shape. Because of that, any method that can deal with the volume enclosed in the shape might have better chance of tracking important illness that develop inside the organ.
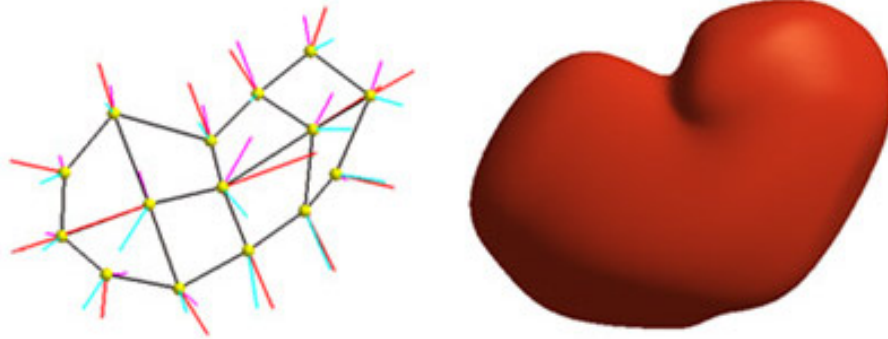
Figure 1.5: Modelization of a kidney anatomy using M-Reps. From University Medical Center Hamburg-Eppendorf.

Two main methodologies exist for defining volumetric shapes: volume approximation using basic functions and medial representations. Performance wise, the basic function approach is highly dependent on the type of function –such as B-splines or spherical harmonics– used to approximate the volume geometry. Most methods use spherical harmonics and restrict to volumes of spherical type, like the brain [48]. Although recent works [53] have applied other basic functions (Hermite polynomials) for generating regular meshes over more complex geometries (like the myocardium), they do not provide a parametric way to locate tissue. Medial representations [10] such as M-Reps [71, 27] and continuous M-Reps [111, 109, 95] describe anatomical volumes using the perpendicular (radial) direction to the volume medial axis/surface (Fig. 1.5) and have been extensively applied to several medical imaging problems [111, 87].

Although medial representations suffice to describe volume geometry, they do not provide parametric coordinates for localization. In addition, they are not well suited for description of the medial branches associated to non-convex shapes. A recent work [109], uses a biharmonic Partial Differential Equation (PDE) to define a radial coordinate for medial surfaces presenting complex branching topologies. The flexibility of the approach allows the representation of anatomies as complex as the myocardium [93]. A main concern is that surface coordinates are given by a discrete, triangular mesh template of the medial surface and, thus, they might not provide a proper parameterization.

1.1.2 Localization in Anatomical Volumes

Having a coordinate system is a key requirement for having localization of tissue and landmarks. The definition of coordinates over a given shape (also known as parameterization of the shape) is the standard way in mathematics of computing the geometric properties describing the shape. A parameterization [14, 86] of a given n-dimensional topological manifold is defined in the context of differential geometry by one to one local maps between the manifold and a domain of the n-dimensional
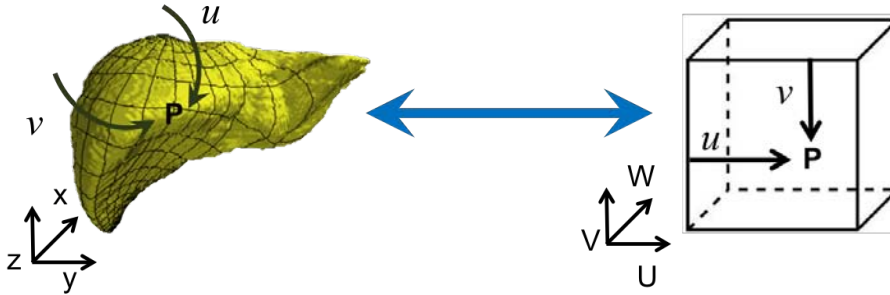
Figure 1.6: Scheme of parameterization of a shape in an embedding cartesian space xyz into a parameterized domain uvw. (iam.cvc.uab.es).

Euclidean space. Parameterizations unwrap the volumetric shape into a cubical region of the Euclidean space as exemplified in Fig. 1.6, generating regular coordinate systems by taking into account the level curves of the parameterization on the volume. It is important for defining valid coordinate curves from parametric maps that they are smooth (diffeomorphic) functions.

It becomes clear that to generate coordinates that cover the interior of the shape we need to provide a radial perpendicular coordinate [10]. This can be achieved by using the information provide by medial structures. Medial structures, such as the medial axis and the medial manifold, completely determine the geometry of the boundary volume [38, 10]. Thus, they could be used to characterize pathological abnormalities [88, 89] and provide more interpretable representations of complex organs [108], and using information of a medial surface for medical imaging segmentation has shown to improve segmentation results [72, 91]. It follows that deformable medial modelling has been used in a variety of medical imaging analysis applications, including computational neuroanatomy [111, 89], 3D cardiac modelling [92] or cancer treatment planning [87, 22]. In shape analysis, medial representations can provide better information than Point Distribution Models since they can model not only the shape but also the interior variations too [110]. Medial manifolds of organs have proved robust and accurate to study group differences in internal structures of the brain [89, 88]. Medial manifolds also provide more intuitive and easily interpretable representations of complex organs [108] and their relative positions [56].

In order to obtain a suitable, smooth parameter for the depth coordinate, one must ensure that the computation of the medial surface (or medial manifold) satisfies three main conditions [74]:

- Homotopy: The medial manifold should maintain the same topology (number of holes, and components) of the original shape.

- Medialness: The medial structure has to lie as close as possible to the center of the original object.

- Thinness: The resulting medial shape should be as thin as possible without

breaking the homotopy rule. The ideal case is to have one pixel-wide structures. However, this concept is too generic, and it heavily depends on the selected connectivity.

Despite their big potential to help in diagnosis and treatment planning, the use of medial structures in systematic clinical practice is still very limited. In our opinion, the main obstacle for a systematic application is the presence of artifacts arising in their digital computation [109, 66].

A main requirement for a confident representation of shapes is the stability of medial manifolds under perturbations of the object boundary [32]. Existing methods for computation of medial surfaces often generate spikes or loose connectivity at main branches. This lack of stability prevents from using medial structures directly in most applications (not only medical [66]). In the particular context of shape modelling and description in medical applications, extra branches complicate statistical modelling of patient populations. Furthermore, complex branching medial geometry also hinders the definition of the medial tubular coordinate [110, 109, 90, 95].

Finally, lack of stability implies that not all branches are meaningful from neither the application point of view nor the object boundary geometrical features.

Stability of medial properties depends on the domain on which the medial manifold is computed. Existing methods compute medial structures on either a tetrahedral mesh of the volume boundary or directly on the volumetric voxel domain.

Mesh methods are based on the Voronoi tetrahedral mesh of a set of points sampled on the object boundary [23, 81, 2, 3, 33] and can naturally resolve branching medial surfaces. However, they introduce one-dimensional spikes associated to boundary irregularities that have to be further pruned [3, 33]. Although some recent methods [33] are capable of efficiently dealing with surface perturbations, they are prone to introduce medial loops that distort the medial topology [66] in a way that could be erroneously considered a pathology. Also their computational cost and quality depend on the number of vertices defining the volume boundary mesh and also on the volume resolution [23]. Finally, in the context of medical applications, the voxel discrete domain is the format in which medical data are acquired from medical imaging devices and, thus, it is the natural domain for the implementation of image processing [49, 57] and shape modelling [70, 69] algorithms. Although it is possible to convert from the discrete voxels to continuous meshes and vice versa, several pre-processing steps (such as smoothing and decimation) are required in order to apply Voronoi methods to clinical volumetric data of large size. These processing steps add computational complexity and inaccuracies due to data interpolation and round-offs, which advises against the use of surface methods in medical data.

Volumetric approaches can be classified into two big types: morphological thinning and energy-based methods. Morphological methods compute medial manifolds by iterative thinning of the exterior layers of the volumetric object until more thinning breaks surface topology [13, 74, 83, 68, 47, 94]. Meanwhile, energy-based approaches define medial structures as singular points of energy maps, usually given by ridges of the distance map to the object boundary [1, 97, 99, 13, 63].

(a)   (b)

Figure 1.7: Medial surfaces obtained using a 6-connected neighborhood, (a), and a 26 connected neighborhood, (b).

Morphological methods require the definition of a neighborhood set and conditions for the removal of *simple voxels*, i.e. voxels that can be removed without changing the topology of the object and surface preserving tests. While simple, they generate completely different results based on the connectivity, as exemplified in figures 1.7a and 1.7b but also depending on the different simplicity, surface or ordering criteria used to determine what pixels can be removed or not. Often the resulting manifold contains many spurious branches that are of little use to many applications and need to be removed using pruning methods [74, 3]. There are numerous different techniques that deal with spurious branches, however, existing medial simplifications have the following disadvantages for a satisfactory applicability to medical applications. In the case of skeleton pruning, spike/branch removal is controlled by some filtering over some geometric conditions, including ratio of geodesic distances [67], angle between generating points [5, 23], distance to boundary [18] or spike size [47, 74]. Although all these criteria are well suited for describing and removing medial surface noise [4, 23, 18], none of them is able to identify the relevance of the branch in the boundary geometric description [33]. The relation between branch simplification and volume reconstruction accuracy is of primary importance for shape modelling applications. As a consequence, it has experienced an increasing research interest in the last years [33, 66, 100]. Concerning template-based methods of shape representation like CM-Reps [109], they maintain branching topology and, thus, they can only fit target anatomy approximately [90]. Although for some simple structures (like the hippocampus), the approximation error is quite small [92], they are prone to fail at properly modelling and detecting pathological deformations. Finally, PDE-based methods [83] implement a morphological thinning using the divergence map for ordered pixel removal. It follows that it has to undergo the same surface test than morphological thinning and results depend on the connectivity used to define local topology.

In the case of energy-based approaches the definition of the ridge map and its further binarization play a prominent role in the stability and quality of medial manifolds. The usual approach is thresholding a ridge operator based on image intensity [13, 63]. The definition of the threshold is a delicate issue that strongly depends on the application and object geometry. A main disadvantage is that these methods might suffer from common pitfalls of the ridge detection algorithms, which are prone to fail at medial self-intersecting branches as the direction of the ridge is not properly

defined. In [13], a method based on ridges and thinning partially corrected these problems, although it inherits the flaws of thinning methods already commented.

Giving that there are many different methods that generate different medial manifolds, it is important to have a system for validating the qualities of the different medial surfaces possibles for our particular goals. Validation in the medical imaging field is a challenging task mainly due to the difficulties for getting consensual ground truth. In the scope of this thesis, a main concern is that validation of accuracy of medial surfaces for medical applications lacks a solid benchmark. There are some datasets that can be used to compute medial manifolds. Some are only 2D, like the MPEG-7 database [54] or the mythologycal creatures database [15], while others are 3D, such as the McGill 3D Shape database [84] but their representation is based on triangular meshes, and they don not provide reference medial surface so there is no ground truth or possible validation.

Aside from the information that the medial manifold provides, an actual method for the computation of coordinate maps over the volume is needed to locate tissue. Harmonic functions that solve the Laplacian equation with Dirichlet or Newman boundary conditions [85] have been proposed to solve the problem. Conformal and harmonic maps have been popular in the computer graphics community for utilities such as multi-resolution analysis of meshes [24] by parameterizing a mesh into another domain where its more easily manageable, but one of the main usages of this method is for texture mapping of 3D Meshes [60]. Indeed, the capabilities of harmonic mapping of taking a 3D mesh and map it in a flat (square) domain are excellent for assigning texture coordinates (u, v) to the vertices of the 3D mesh. Harmonic maps have been used in medical imaging for defining surface mappings on spherical organs, such as the brain, given that the sulci in the brain surface has relevant information about function and organ development [77]. Gu et al. [39] perform a conformal map of the brain surface via minimization of the harmonic energy. In [102] the authors parameterize the brain surface in a series of subdivided patches. In a more recent work [6], a merging of multiple mappings is presented to compute a complete map of the brain surface.

However, compared with the volume of publications regarding surface parameterizations, to the best of our knowledge, volumetric parameterizations have been hardly explored. Aside from [103] that uses harmonic maps to produce 3D tetrahedral meshes of 3D models, [64] that uses a multi-layered volumetric tetrahedral parameterization with medial information, and [107], which performed multilayered mesh based parameterizations with a biharmonic PDE, the potential of harmonic PDE to generate mapping in the whole 3D volume of complex anatomies has been seldomly explored, and always in the mesh domain, without establishing explicit coordinates.

Table 1.1 summarizes in broad terms, the capabilities of the reviewed methods. It shows the necessity of a new methodology combining shape comparison with depth representation, including image features but with added localization of tissue.

	Appearance	Shape	Depth	Localization
Volume registration	yes	no	no	no
Statistical models SSM	no	yes	no	no
AAM	yes	yes	no	no
Shape representations	no	yes	yes	no
Harmonic maps	no	yes	no	no

Table 1.1: Overview of techniques reviewed and its capabilities for image comparison, shape comparison, depth representation and localization.

1.2 Goals and Contributions

Given the state of the art, it seems that there is not a single technique that can do both comparison of anatomical volumes and localization. We claim that this can be accomplished –and this will be our **goal**– by combining the information about shape provided by medial manifolds with a powerful shape descriptor tool such as coordinate systems based on harmonic mappings.

In order to provide accurate coordinates of anatomical geometry that include depth information, we require three main components:

1. A proper loci to define the origin of the depth coordinate.

2. A proper set of anatomical landmarks that will work as origin of coordinates. These will be application dependent, but in the context of anatomical shape parameterizations choosing functional landmarks will improve the meaning of the coordinate systems to match the characteristics of the function of the organ.

3. A method to extend these coordinates to the rest of the anatomical domain.

For the first requisite, we have to select the best point or set of points to use as origin of medial coordinates. The centroid of the object is not guaranteed to fall in the interior of the object. This can happen with concave shapes, so it should be discarded. Medial axis (skeletons) are only useful in objects with tubular shape and circular cross section, but its generalization, medial manifolds, are well suited to play the role of origin of depth coordinate [10, 38].

We observe that the assignment of equal coordinate values at specific key anatomical sites ensures correspondence of different anatomies through the parametric domain. Intuitively, such key anatomical sites represent coordinate origins so that relative coordinates extending from them should correspond to anatomically equivalent points [34, 31, 30, 76]. Dirichlet boundary conditions allow setting specific coordinate values at these anatomical sites [28], addressing requirement number 2. The coordinates fixed on such sites propagate over the whole domain using harmonic maps (requisite number 3) and, thus, their variation uniquely determines the parametric map.

The method proposed in this dissertation will have the main advantage over more conventional techniques of covering also the interior of the volume, at a voxel level ensuring the registration of intensity information as well.

To achieve this goal, this thesis **contributes** to the state of the art in medical imaging techniques in several ways:

1. we present improved medial maps that can be used to generate smooth medial surfaces that describe well the shape of anatomical shapes.

2. we present a method for branch singularity decomposition and binarization of medial maps into medial surfaces.

3. we released a public database of synthetic shapes for validation and comparison of medial surface generation methods.

4. we propose to use functional/anatomy based coordinate systems in order to compare anatomy and localize injured tissue based on the Laplacian properties. The coordinate systems will not only span the surface of the object to be analyzed but also the interior of the object. Medial information will be added to the method to ensure proper definition of the coordinate system inside of the object.

5. we defined proper functional boundary conditions for both the liver and the cochlear anatomy as examples of the proposed coordinate systems.

The rest of this thesis is organized as follows: chapter 2 describes a new improved medial maps for the computation of medialness voxels. In chapter 3 we explore a mathematical and image based framework for the decoupling of branch and surface intersections of medial surfaces. Chapter 4 presents the framework for using the medial surfaces and the properties of the harmonic mapping for definition of parameterizations and coordinate systems, and presents the settings for parameterization of the liver and cochlear anatomy. Finally, in chapter 5 we present the conclusions extracted from this thesis and new lines of research that this thesis opens.

Chapter 2

Medial Maps for Reliable Extraction of Anatomical Medial Surfaces

Many organs in the human anatomy have a shape that can be represented by a genus zero surface. Nevertheless, such generalization cannot hide the complexity of human anatomical shapes. Even by this broad description, anatomical shapes display a large amount of variability between different organs (liver, kidney, brain...) but also variability between the same organ over different patients as we have seen in the previous chapter. This large variability makes anatomical shapes challenging to process by computer techniques. Medial surfaces have demonstrated to be a compact shape descriptor and have shown potential to capture shape variations. With all this properties they can be used as origins of depth coordinates for our parameterizations.

To that extent, one must ensure that the medial surfaces have certain properties that do not hinder the parameterization. Ideally the medial surface should be complete enough to capture the key anatomical shapes of an organ but simple enough so that changes of the depth parameter respond to true changes in shape and not to medial artifacts.

We have seen that medial surface generation methods are prone to produce noise medial surfaces with spurial branches that will produce artifacts in the parameterization. While pruning operations will decrease the these artifacts there is risk of removing a relevant part of the medial structure. Obtaining a good medial surface for parameterization means to find a compromise between the shape representation and simplicity of medial surface. And as we have pointed in the past chapter, many methods of computation of medial surfaces generate this unwanted branching patterns on the medial surface, making them sub-optimal for the purpose of being used in a parameterization. Our goal will be to develop medial maps that can lead to medial manifolds with good characteristics for their usage in parameterization of anatomical shapes.
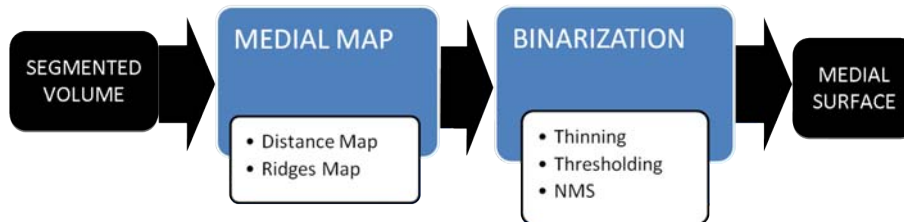
Figure 2.1: Schema of medial surface generation methods.

This chapter contributes to the medial surface computation state of the art in two ways:

1. A novel energy-based method for medial surface computation in images of arbitrary dimensions based on the combination of Gaussian and normalized operators as medialness map followed by non iterative thinning binarization based binarization step is free of topology rules, as it is based on Non-Maxima Suppression (NMS) [17]

2. A validation framework for fair comparison of the quality of medial surfaces: the variability in existing methods for medial surface generation makes comparisons with other methods difficult. This database, can be used to compute and compare different methods for computation of medial surfaces.

   Quantitative evaluation of our method in comparison with existing approaches is shown on the synthetic shapes of known medial geometry. Finally, results are shown on sets of segmented livers obtained from [42], as well as multi-organ datasets [78].

The rest of this chapter is organized as follows: section 2.1 describes the computation of an enhanced medial map for the generation of medial surfaces. Section 2.2 presents the validation protocol, synthetic database and metrics for benchmarking medial map methods. Section 2.3 provides information about the validation results and finally section 2.4 includes some thoughts and remarks about the techniques presented.

2.1 Extracting Anatomical Medial Surfaces Using Medialness Maps

The computation of medial manifolds from a segmented volume may be split into two main steps: computation of a medial map from the original volume and binarization of such map. Medial maps should achieve a discriminant value on the shape central voxels, while the binarization step should ensure that the resulting medial structures fulfill the three quality conditions [74] that ensure fair representation of volumes geometry: medialness, thinness and homotopy.

Distance transforms are the basis for obtaining medial manifolds from volumes in any dimension [74]. The distance transform, also called distance map, is an operator that given a binary volume of a closed domain B, computes for each volume voxel its distance to the domain boundary, ∂B. The distance map $D(B)$ is defined as:

$$D(B) = \min_x \{d(x,y) : x \in B \text{ and } y \in \partial B\} \tag{2.1}$$

where $d(x,y)$ is a distance metric defined on the ambient Euclidean space and is usually the L^2 norm euclidean between x and y $d(x,y) = \|x - y\|_{L^2}$. By definition, maximum values are achieved at the center of B the shape at voxels corresponding to the volume medial structure and depend on the local thickess of the shape.

By the maximality property of distance maps, the medial surface can be obtained using several methods such as iterative thinning [74], but it can lead to generation of spikes and other discretization artifacts due to the different neighborhood definitions available. An alternative to iterative thinning is applying a threshold to $D(B)$. Thresholding keeps voxels with medial map energy above a given value th, so that medial voxels would be defined as

$$\mathcal{M} = Th(D(B)) = \begin{cases} 0 & x \in D(B) < th \\ 1 & x \in D(B) \geq th \end{cases} \tag{2.2}$$

The selection of a good thresholding value of th ensuring homotopy and thinness is problematic. The maximum value of the distance map represents the minimum distance from the medial manifold to the object's boundary. Its value is, therefore, related with the local thickness of of the object, and cannot be considered as a global constant value through all the object. On one hand, a too high threshold value is prone to generate unconnected manifold structures violating the homotopy property. On the other hand, a too small value for th means that the medial structure may not be thin. Albeit useful, the distance map is a less than an optimal medialness energy map because it is not selective enough and hinders the binarization step. Further examination of the distance map shows that its central maximal voxels are connected and constitute a ridge surface of the distance map. That is why we claim that the ridges of the distance map provide a better tool to describe the medialness of a set of shape pixels.

2.1.1 Gaussian Steerable Medial Maps

Ridges/valleys in a digital N-Dimensional image are defined as the set of points that are extrema (minima for ridges and maxima for valleys) in the direction of greatest magnitude of the second order directional derivative [40]. In image processing, ridge detectors are based either on image intensity profiles [29] or level sets geometry [59]. From the available operators for ridge detection, we have chosen the creaseness measure described in [59] because it provides (normalized) values in the range $[-N, N]$. The ridgeness operator is computed by the structure tensor of the distance map as follows.

Let D denote the distance map to the shape and let its gradient, ∇D, be computed by convolution with partial derivatives of a Gaussian kernel:

$$\nabla D = (\partial_x D_\sigma, \partial_y D_\sigma, \partial_z D_\sigma) = (\partial_x g_\sigma * D, \partial_y g_\sigma * D, \partial_z g_\sigma * D) \qquad (2.3)$$

being g_σ a Gaussian kernel of variance σ and ∂_x, ∂_y and ∂_z partial derivative operators. The structure tensor or second order matrix [9] is given by averaging the projection matrices onto the distance map gradient:

$$ST_{\rho,\sigma}(D) = \begin{pmatrix} g_\rho * \partial_x D_\sigma^2 & g_\rho * \partial_x D_\sigma \partial_y D_\sigma & g_\rho * \partial_x D_\sigma \partial_z D_\sigma \\ g_\rho * \partial_x D_\sigma \partial_y D_\sigma & g_\rho * \partial_y D_\sigma^2 & g_\rho * \partial_y D_\sigma \partial_z D_\sigma \\ g_\rho * \partial_x D_\sigma \partial_z D_\sigma & g_\rho * \partial_y D_\sigma \partial_z D_\sigma & g_\rho * \partial_z D_\sigma^2 \end{pmatrix} \qquad (2.4)$$

for g_ρ a Gaussian kernel of variance ρ. Let V be the eigenvector of principal eigenvalue of $ST_{\rho,\sigma}(D)$ and consider its reorientation along the distance gradient, $\tilde{V} = (P, Q, R)$, given as:

$$\tilde{V} = \text{sign}(< \tilde{V} \cdot \nabla D >) \cdot \tilde{V} \qquad (2.5)$$

for $< \cdot >$ the scalar product. The ridgeness measure or NRM (Normalized Ridge Map) [59] is given by the divergence:

$$NRM := \text{div}(\tilde{V}) = \partial_x P + \partial_y Q + \partial_z R \qquad (2.6)$$

The above operator assigns positive values to ridge pixels and negative values to valley ones. The more positive the value is, the stronger the ridge patterns are. A main advantage over other operators (such as second order oriented Gaussian derivatives) is that $\mathcal{R} \in [-N, N]$ for N the dimension of the volume. In this way, it is possible to set a threshold, τ, common to any volume for detecting significant ridges and, thus, points highly likely to belong to the medial surface. However, by its geometric nature, NRM has two main limitations. In order to be properly defined, NRM requires that the vector $\tilde{V}$ uniquely defines the tangent space to image level sets. Therefore, the operator achieves strong responses in the case of one-fold medial manifolds, but significantly drops anywhere two or more medial surfaces intersect each other. Additionally, NRM responses are not continuous maps but step-wise almost binary images (Fig. 2.2). Such discrete nature of the map is prone to hinder the performance of the NMS binarization step that removes some internal voxels of the medial structure and, thus, introduces holes in the final medial surface.

Ridge maps based on image intensity are computed by convolution with a bank of steerable filters [29]. Steerable filters are given by derivatives of oriented anisotropic 3D Gaussian kernels. Let $\sigma = (\sigma_x, \sigma_y, \sigma_z)$ be the scale of the filter and $\Theta = (\theta, \phi)$ its orientation given by the unitary vector $\eta = (cos(\phi)cos(\theta), cos(\phi)sin(\theta), sin(\phi))$, then the oriented anisotropic 3D Gaussian kernel, g_σ^Θ, is given by:

$$g_\sigma^\Theta = g_{(\sigma_x, \sigma_y, \sigma_z)}^{(\theta, \phi)} = \frac{1}{(2\pi)^{3/2}\sigma_x\sigma_y\sigma_z} e^{-\left(\frac{\tilde{x}^2}{2\sigma_x^2} + \frac{\tilde{y}^2}{2\sigma_y^2} + \frac{\tilde{z}^2}{2\sigma_z^2} \right)} \qquad (2.7)$$

for $(\tilde{x}, \tilde{y}, \tilde{z})$ the change of coordinates given by the rotations of angles θ and ϕ that transform the z-axis into the unitary vector η:

$$\begin{pmatrix} \tilde{x} \\ \tilde{y} \\ \tilde{z} \end{pmatrix} = R_x(\theta) R_y(\phi) R_x(-\theta) \begin{pmatrix} x \\ y \\ z \end{pmatrix} \tag{2.8}$$

with $R_x(\theta)$, $R_y(\phi)$ the following rotation matrices:

$$R_x(\theta) = \begin{pmatrix} 1 & 0 & 0 \\ 0 & \cos(\theta) & -\sin(\theta) \\ 0 & \sin(\theta) & \cos(\theta) \end{pmatrix} \quad R_y(\phi) = \begin{pmatrix} \cos(\phi) & 0 & \sin(\phi) \\ 0 & 1 & 0 \\ -\sin(\phi) & 0 & \cos(\phi) \end{pmatrix} \tag{2.9}$$

The second partial derivative of g_σ^Θ along the $\tilde{z}$ axis constitutes the principal kernel for computing ridge maps:

$$\partial_z^2 g_\sigma^\Theta = (\tilde{z}^2/\sigma_z^4 - 1/\sigma_z^2) g_\sigma^\Theta \tag{2.10}$$

We note that by tuning the anisotropy of the Gaussian, we can detect independently medial surfaces and medial axes. For detecting sheet-like ridges, the scales should be set to $\sigma_z < \sigma_x = \sigma_y$, while for medial axes they should fulfill $\sigma_z < \sigma_x < \sigma_y$.

The maximum response across Gaussian kernel orientations and the scales gives the medial map:

$$SGR := \max_{\Theta, \sigma} \left(\partial_z^2 g_\sigma^\Theta * D \right) \tag{2.11}$$

for Θ expressing different orientations of the Gaussian kernel, and σ the scales.

A main advantage of using steerable filters is that their response does not decrease at self-intersections. Their main counterpart is that their response is not normalized, so setting the threshold for binarization becomes a delicate issue [13, 63].

Given that geometric and intensity methods have complementary properties, we propose combining them into a Geometric Steerable Medial Map (GSM2):

$$GSM2 := SGR(NRM) \tag{2.12}$$

GSM2 generates medial maps with good combination of specificity in detecting medial voxels while having good characteristics for NMS binarization, which does not introduce internal holes.

Figure 2.2 shows the performance of different ridge operators at a 2 dimensional branch (highlighted in the square close up). The geometric NRM (left) produces highly discriminant ridge values. However, they depend on the uniqueness of the direction surface normal, and thus its response significantly decreases at surface branches or self intersections. Steerable Gaussian filters (center) are less sensible to strong ridges while having increased sensitivity to small, secondary noisy ridges. Finally, the combined approach GSM2 (right) inherits the strong features of each approach. It follows that it achieves an homogeneous response along ridges (induced by NRM normalization) which does not decrease at branches (thanks to the orientations provided by SGR).
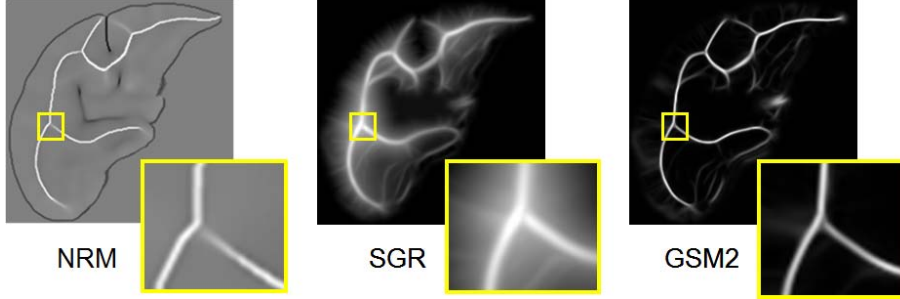
Figure 2.2: Performance of different ridge operators. From left to right: NRM, SGR and GSM2.

2.1.2   Non-Maxima Suppression Binarization

Converting the medialness energy map into a binary set of voxels can be achieved by several ways. As previously stated, thresholding the intensity values of the medialness map yields a reduced set of voxels that are likely to belong to the medial manifold. However, the subset of voxels obtained using thresholding does not necessarily fulfill the property of thinness, and the homotopy heavily depends on the threshold value and the performance of the medial operator at intersections. The usage of iterative thinning schemes after thresholding can generate a thin structure [13], but at the risk of introducing spikes and different surfaces depending on the definition of simple or medial voxels and the order in which voxels are processed.

As alternative we propose to use Non-Maxima Suppression (NMS) to obtain a thin, one voxel wide medial surface. Non-Maxima Suppression is a well known technique for gettinh the local maxima of an energy map [17]. For each voxel, NMS consists in checking that the value of its neighbors in a specific direction, V are lower than the actual voxel value. IF this condition is not met, the voxel is discarded. In this manner, only voxels that are local maxima along the direciton V are preserved. neighbors of a pixel in a specific direction, V, and delete pixels if their value is not the maximum one:

$$NMS(x,y,z) = \begin{cases} \mathcal{M}(x,y,z) & \text{if } \mathcal{M}(x,y,z) > \max(\mathcal{M}_{V+}(x,y,z),\ \mathcal{M}_{V-}(x,y,z)) \\ 0 & \text{otherwise} \end{cases}$$

$$(2.13)$$

for $\mathcal{M}_{V+} = \mathcal{M}(x + V_x, y + V_y, z + V_z)$ and $\mathcal{M}_{V-} = \mathcal{M}(x - V_x, y - V_y, z - V_z)$.

A main requirement to apply NMS is identifying the local-maxima direction from the medial map derivatives. The search direction for local maxima is given by the eigenvector of greatest eigenvalue of the structure tensor of the ridge map, $ST_{\rho,\sigma}(\mathcal{M})$ given by eq. (2.4), since it indicates the direction of highest variation of the ridge image. In order to overcome small glitches due to discretization of the direction, NMS is computed using trilinear interpolation.

2.1.3 Parameter Setting

Unlike most of existing parametric methods, the theoretical properties of GSM2 provide a natural way of setting parametric values regardless of the volume size and shape.This new method depends on the parameters involved in the definition of the map GSM2 and in the NMS binarization step.

The parameters arising in the definition of GSM2 are the derivation, σ, and integration, ρ, scales of the structure tensor $ST_{\rho,\sigma}(\mathcal{M})$ used to compute NRM. The derivation scale σ is used to obtain regular gradients in the case of noisy images. The larger it is the more regular the gradient will be at the cost of losing contrast. The integration scale ρ used to average the projection matrices corresponds to time in a solution to the heat equation with initial condition the projection matrix. Therefore large values provide a regular extension of the level sets normal vector, which can be used for contour closing [35]. Since in our case we apply NRM to a regular distance map with well defined completed ridges, σ and ρ can be set to their minimum values, $\sigma = 0.5$ and $\rho = 1$.

Concerning steerable filters, the parameters, are the scales, $\sigma = (\sigma_x, \sigma_y, \sigma_z)$, and orientations Θ, defining the steerable filter bank in (2.12). These last parameters are usually sampled on a discrete grid, so that eq. (2.11) becomes

$$SGR := \max_{i,j,k} \left(\partial_z^2 g_{\sigma_k}^{\Theta_{i,j}} * D \right) \tag{2.14}$$

for $\Theta_{i,j}$ given by $\theta_i = \{i\frac{\pi}{N}, \forall i = 1, \ldots, N\}$ and $\phi_j = \{j\frac{\pi}{M}, \forall j = 1, \ldots, M\}$ and $\sigma_k = (\sigma_x^k, \sigma_y^k, \sigma_z^k) = (2^{k+1}, 2^{k+1}, 2^k), k = [0, K]$. Scale depends on the thickness of the ridge and orientations on the complexity of the ridge geometry. The selection of the scale might be critical in the general setting of natural scenes [55]. However in our case, SGR is applied to a normalized ridge map that defines step-wise almost binary images of ridges (see Fig. 2.2, left). Therefore, the choice of scale is not critical anymore. In order to get medial maps as accurate as possible, we recommend using a minimum anisotropic setting: $\sigma_z = 1$, $\sigma_x = \sigma_y = 2$. Finally, orientation sampling should be dense enough in order to capture any local geometry of medial surfaces. In the case of using the minimum scale, eight orientations, $N = M = 8$, are enough.

Therefore, GSM2 is given by:

$$GSM2 = \max_{i,j} \left(\partial_z^2 g_{(2,2,1)}^{\Theta_{i,j}} * NRM \right) \tag{2.15}$$

for NRM computed over $ST_{1,0.5}(\mathcal{M})$ and $\Theta_{i,j}$ computed setting $N = M = 8$.

The parameters involved in NMS binarization step are the scales of the structure tensor $ST_{\rho,\sigma}(GSM2)$ and the binarizing threshold, τ. Like in the case of NRM, $GSM2$ is a regular function which maximums define closed medial manifolds, so we set the structure tensor scales to their minimum values $\sigma = 0.5$ and $\rho = 1$. Concerning τ, it can be obtained using any histogram threshold calculation, since $GSM2$ inherits the uniform discriminative response along ridges of NRM.

2.2 Validation Framework for Medial Anatomy Asessment

In order to address the representation of organs for medical use, medial representations should achieve a good reconstruction of the full anatomy and guarantee that the boundaries of the organ are reached from the medial surface. Given that small differences in algorithm criteria can generate different surfaces, we are interested in evaluating the quality of the generated manifold as a tool to recover the original shape.

Validation in the medical imaging field is a delicate issue due to the difficulties for generating ground truth data and quantitative scores valid for reliable application to clinical practice. In this section, we describe our validation framework for evaluating medial surface quality in the context of medical applications. In particular we will generate a synthetic database with ground truth (GT) and two quality tests for assessing the quality of the medial anatomy for data with and without GT The database can be used to benchmark algorithms using two tests.

2.2.1 Synthetic Database

The test set of synthetic volumes / surfaces aims to cover different key aspects of medial surface generation (see first row in Fig.2.3). The first batch of surfaces (labelled 'Simple') includes objects generated with a single medial surface. A second batch of surfaces is generated using two intersecting medial surfaces (labelled 'Multiple'), while a last batch of objects (labelled 'Homotopy') covers shapes with different number of holes. Each family of medial topology has 20 samples. The volumetric object obtained from a surface can be generated by using spheres of uniform radii (identified as 'UnifDist') or with spheres of varying radii (identified as 'VarDist').

Volumes are constructed by assigning a radial coordinate to each medial point. In the case of UnifDist, all medial points have the same radial value, while for VarDist they are assigned a value in the range $[5, 10]$ using a polynomial. The values of the radial coordinate must be in a range ensuring that volumes will not present self intersections. Therefore, the maximum range and procedure this radius is assigned depends on the medial topology:

- *Simple.* In this case, there are no restrictions on the radial range.

- *Multiple.* For branching medial surfaces, especial care must be taken at surface self-intersecting points. At these locations, radii have to be below the maximum value that ensures the the medial representation defines a local coordinate change [38]. This maximum value depends on the principal curvatures of the intersecting surfaces [38] and it is computed for each surface. Let $\mathcal{M}$ be the medial surface, Z denote the self-intersection points and $D(Z)$ the distance map to Z. The radial coordinate is assigned as follows:

$$R(X) = min(R(X), max(r_Z, D(Z))) \tag{2.16}$$

for $R(X)$ the value of the polynomial function and r_Z the maximum value allowed at self-intersections. In this manner, we obtain a smooth distribution of the radii ensuring volume integrity.

- *Homotopy.* In order to be consistent with the third main property of medial surfaces [74], volumes must preserve all holes of medial surfaces. In order to do so, the maximum radius r_2 is set to be under the minimum of all surface holes radii.

2.2.2   Medial Surface Quality

The database can be used to benchmark algorithms using two tests. The first test evaluates the quality of the medial surface generated, while the second one explores the capabilities of the generated surfaces to recover the original volume and describing anatomical structures. Surface quality tests start from known medial surfaces, that will be considered as ground truth. From this surfaces, volumetric objects can be generated by placing spheres of different radii at each point of the surface. The newly created object is then used as input to several medial surface algorithms and the resulting medial surfaces, compared with the ground truth.

The quality of medial surfaces has been assessed by comparing them to ground truth surfaces in terms of surface distance [42]. The distance of a voxel y to a surface X is given by: $D_X(y) = \min_{x \in X} \|y - x\|$, for $\| \cdot \|$ the Euclidean norm. If we denote by X the reference surface and Y the computed one, the scores considered are:

1. *Standard Surface Distances*:

$$AvD = \frac{1}{|Y|} \sum_{y \in Y} D_X(y) \tag{2.17}$$

$$MxD = \max_{y \in Y}(D_X(y)) \tag{2.18}$$

2. *Symmetric Surface Distances*:

$$AvSD = \frac{1}{|X| + |Y|} \left(\sum_{x \in X} d_Y(x) + \sum_{y \in Y} d_X(y) \right) \tag{2.19}$$

$$MxSD = \max \left(\max_{x \in X}(D_Y(x)), \max_{y \in Y}(D_X(y)) \right) \tag{2.20}$$

Standard distances measure deviation from medialness, while differences between standard and symmetric distances indicate the presence of homotopy artifacts and presence of unnecessary medial segments.

For each family and method, we have computed quality scores statistical ranges as $\mu \pm \sigma$, for μ and σ the average and standard deviation computed over the 20 samples

of each group of shapes. The Wilcoxon signed rank test [105] has been used to detect significant differences across performances.

In medical imaging applications the aim is to generate the simplest medial surface that allows recovering the original volume without losing significant voxels. Volumes recovered from surfaces generated with the different methods are compared with ground truth volumes. Volumes are reconstructed by computing the medial representation [10] with radius given by the values of the distance map on the computed medial surfaces. Ground truth volumes are given by anatomical meshes extracted from original medical scans.

Comparisons with the original anatomical volumes are based on the average and maximum symmetric surface distances (AvSD and MxSD given in (2.19) and (2.20) respectively, computed using the anatomic boundary surface and reconstructed volume boundaries, as well as the following volumetric measures:

1. *Volume Overlap Error:*

$$VOE(A, B) = 100 \times \left(1 - 2 \frac{|A \cap B|}{|A| + |B|} \right) \tag{2.21}$$

2. *Relative Volume Difference:*

$$RVD(A, B) = 100 \times \frac{|A| - |B|}{|B|} \tag{2.22}$$

3. *Dice coefficient:*

$$Dice(A, B) = \frac{2|A \cap B|}{|A| + |B|} \tag{2.23}$$

for A, B, being respectively the original and reconstructed volumes. Aside from dice coefficient, lower metric values indicate better reconstruction capability. Like in the case of the synthetic surfaces, for each medial surface method we have computed quality scores statistical ranges as $\mu \pm \sigma$, for μ, σ computed on the medical data set, and Wilcoxon signed rank tests.

2.3   Validation Experiments

Our validation protocol has been applied to the method described in Section 2.1.1. To provide a real scenario for the reconstruction tests we have used 14 livers from the SLIVER07 challenge [42] as a source of anatomical volumes. In order to compare to morphological methods, we have also applied it to an ordered thinning using a 6-connected neighborhood criterion for defining medial surfaces (labelled Th_6) described in [12], a 26-connected neighborhood surface test (labelled Th_{26}) following [74]. The consistency of surface pruning is tested on a pruned version of the 26-connected neighborhood method (labelled ThP_{26}) that does not allow degenerated medial axis segments and the scheme (labelled Tao_6) described in [47] that alternates 6-connected curve and surface thinning with more sophisticated pruning stages.
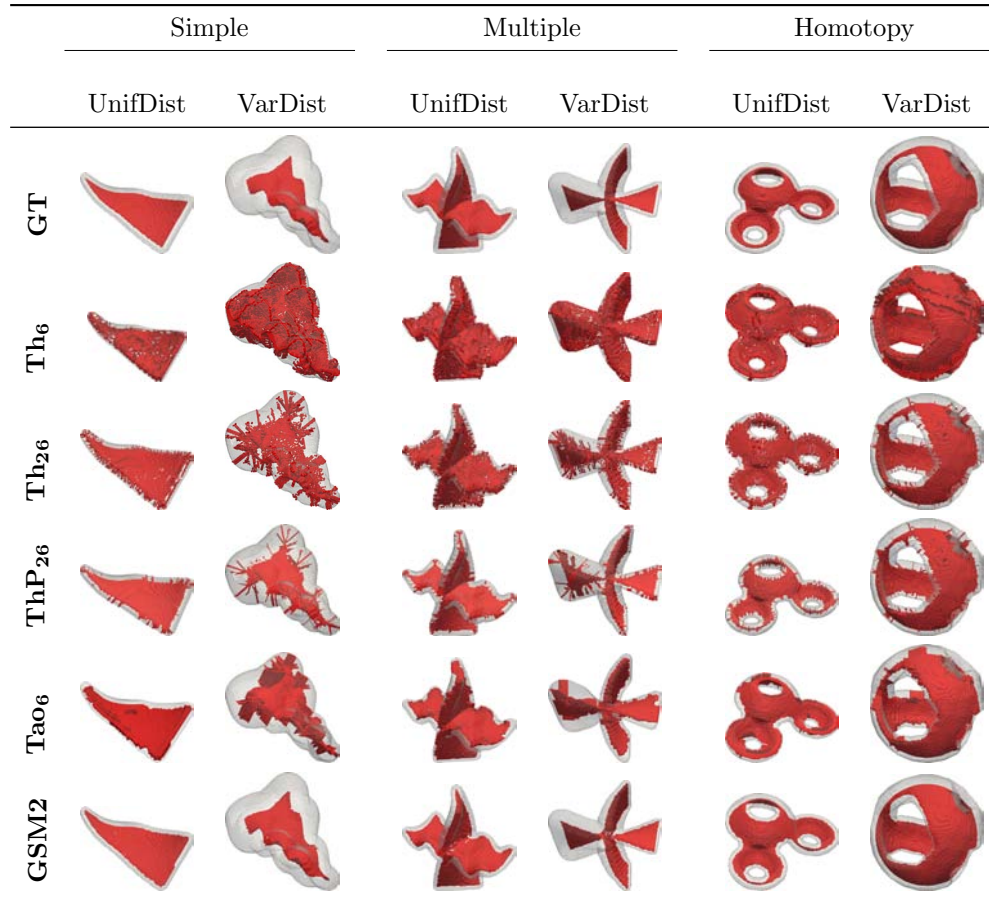
Figure 2.3: Medial surfaces. Examples of the compared methods for each synthetic volume family.

2.3.1   Medial Surface Quality

Figure 2.3 shows an example of the synthetic volumes in the first row and the computed medial surfaces in the remaining rows. Columns exemplify the different families of volumes generated: one (Simple in 1st and 2nd columns) and two (Multiple in 3rd and 4th columns) foil surfaces, as well as, surfaces with holes (Homotopy in 5th and 6th columns). For each kind of topology we show a volume generated with constant (1st, 3rd and 5th columns) and variable distance (2nd, 4th and last columns). We show medial surfaces in solid meshes and the synthetic volume in semi-transparent color. The shape of surfaces produced using morphological thinning strongly depends on the connectivity rule used. In the absence of pruning, surfaces, in addition, have either extra medial axes attached or extra surface branches in the case pruning is included as part of the thinning surface tests (Tao_6). On the contrary, GSM2 medial

surfaces have a well defined shape matching the original synthetic surface.

Table 2.1 reports error ranges for the four methods and the different types of synthetic volumes, as well as total errors in the last column. For all methods, there are not significant differences between standard and symmetric distances for a given volume. This indicates a good preservation of homotopy. Even with pruning, thinning has significant geometric artifacts (maximum distances increase) and might drop its performance for variable distance volumes due to a different ordering for pixel removal and type of surface preserved.

According to a Wilcoxon signed rank test, strategies alternating curve and surface thinning with pruning stages have worse average distances than other morphological strategies ($p < 0.0001$ for AvD and $p < 0.0001$ for $AvSD$). Given that maximum distances do not significantly differ ($p = 0.4717$, $p = 0.6932$, $p = 0.7752$ for MxD and $p = 0.9144$, $p = 0.7463$, $p = 0.6669$ for $MxSD$), this indicates the introduction of extra structures of larger size (extra surface branches in Tao_6 for the variable volumes shown in Fig. 2.3).

The performance of GSM2 is significantly better than other methods (Wilcoxon signed rank test with $p < 0.0001$), presents high stability across volume geometries and produces accurate surfaces matching synthetic shapes. The small increase errors for multiple self-crossing surfaces is explained by the presence of holes at intersections between medial manifolds. Still its overall performance clearly surpasses performance of morphological approaches.

2.3.2 Reconstruction Power for Clinical Applications

Table 2.2 reports the statistical ranges for all methods and measures computed for the 14 livers. There are not significant differences among methods and best performers vary depending on the quality measure. However, our approach and the two thinnings, Th_{26P} and Tao_6, have an overall better reconstruction power.

Figure 2.4 shows the medial surface of healthy liver obtained with the thinning methods and Fig. 2.5 left, GSM2 medial surface. In the case of thinning based methods, medial manifolds have a more complex geometry than GSM2 and might include extra structures and self intersections (Fig. 2.4). In medical applications such extra structures might hinder the identification of abnormal or pathological structures. This is not the case for GSM2 surfaces as exemplified in Fig. 2.5. The oversized superior lobe on the right liver is captured by the presence of an unusual medial manifold configuration.

We also computed the medial surfaces of a more complex scenario of multi-organ abdominal dataset obtained from the mean image of an altas [78]. Initial results on the medial representation of multiple abdominal organs are shown in Fig. 2.6. Given that the surrounding organs provide constrains for the position and shape of an organ, it can be observed that medial representations of neighboring organs contain information about shape and topology that can be exploited for the description of organ shape and configuration in relation to its neighboring organs.

	Simple		Multiple		Homotopy		Total
	UnifDist	VarDist	UnifDist	VarDist	UnifDist	VarDist	
GSM2							
AvD	0.28 ± 0.09	0.28 ± 0.07	0.38 ± 0.09	0.43 ± 0.18	0.37 ± 0.18	0.34 ± 0.14	0.34 ± 0.14
MxD	2.99 ± 0.50	3.50 ± 1.53	3.56 ± 0.53	4.76 ± 1.51	3.39 ± 0.48	3.70 ± 0.84	3.65 ± 1.13
AvSD	0.24 ± 0.05	0.25 ± 0.05	0.37 ± 0.32	0.37 ± 0.18	0.29 ± 0.10	0.28 ± 0.08	0.30 ± 0.17
MxSD	3.02 ± 0.46	3.66 ± 1.52	4.10 ± 2.61	4.76 ± 1.51	3.39 ± 0.48	3.70 ± 0.84	3.78 ± 1.52
Th$_6$							
AvD	1.52 ± 0.27	5.63 ± 2.19	1.66 ± 0.30	3.05 ± 0.75	1.56 ± 0.35	2.96 ± 1.17	2.73 ± 1.80
MxD	5.55 ± 0.26	16.21 ± 4.76	5.82 ± 0.27	10.75 ± 3.40	5.54 ± 0.20	10.17 ± 3.20	9.01 ± 4.72
AvSD	1.04 ± 0.21	4.34 ± 1.94	1.16 ± 0.24	2.24 ± 0.56	1.09 ± 0.28	2.13 ± 0.98	2.00 ± 1.48
MxSD	5.55 ± 0.26	16.21 ± 4.76	5.82 ± 0.27	10.75 ± 3.40	5.54 ± 0.20	10.17 ± 3.20	9.01 ± 4.72
Th$_{26}$							
AvD	0.85 ± 0.25	3.15 ± 1.34	1.00 ± 0.19	1.89 ± 0.52	0.86 ± 0.37	1.63 ± 0.84	1.56 ± 1.07
MxD	5.51 ± 0.25	16.17 ± 4.78	5.58 ± 0.19	10.64 ± 3.43	5.46 ± 0.25	10.09 ± 3.21	8.91 ± 4.75
AvSD	0.56 ± 0.14	2.02 ± 0.92	0.67 ± 0.12	1.24 ± 0.35	0.59 ± 0.22	1.05 ± 0.56	1.02 ± 0.69
MxSD	5.51 ± 0.25	16.17 ± 4.78	5.58 ± 0.19	10.64 ± 3.43	5.46 ± 0.25	10.09 ± 3.21	8.91 ± 4.75
ThP$_{26}$							
AvD	0.57 ± 0.20	2.24 ± 1.00	0.70 ± 0.17	1.38 ± 0.37	0.54 ± 0.24	1.11 ± 0.62	1.09 ± 0.79
MxD	5.49 ± 0.27	16.16 ± 4.78	5.58 ± 0.19	10.61 ± 3.43	5.41 ± 0.27	10.08 ± 3.23	8.89 ± 4.76
AvSD	0.41 ± 0.11	1.38 ± 0.61	0.50 ± 0.11	0.92 ± 0.24	0.41 ± 0.12	0.72 ± 0.37	0.72 ± 0.47
MxSD	5.49 ± 0.27	16.16 ± 4.78	5.58 ± 0.19	10.61 ± 3.43	5.41 ± 0.27	10.08 ± 3.23	8.89 ± 4.76
Tao$_6$							
AvD	0.79 ± 0.21	4.82 ± 2.05	0.86 ± 0.17	2.46 ± 1.09	0.85 ± 0.29	2.48 ± 1.20	2.04 ± 1.79
MxD	4.87 ± 0.20	17.55 ± 5.19	4.92 ± 0.17	11.10 ± 3.71	4.79 ± 0.21	11.64 ± 4.33	9.14 ± 5.68
AvSD	0.51 ± 0.14	3.92 ± 1.73	0.59 ± 0.13	2.00 ± 0.96	0.59 ± 0.27	1.99 ± 1.03	1.60 ± 1.52
MxSD	4.89 ± 0.18	17.55 ± 5.19	5.32 ± 1.42	11.10 ± 3.71	5.53 ± 3.26	11.87 ± 4.25	9.38 ± 5.73

Table 2.1: Error ranges (mean and standard deviation) for the Synthetic Volumes

	$GSM2$	Th_6	Th_{26}	ThP_{26}	Tao_6
Volume Error					
VOE	7.96 ± 1.70	8.84 ± 1.73	8.25 ± 1.72	7.84 ± 1.68	8.49 ± 1.77
RVD	8.49 ± 2.03	9.10 ± 2.10	8.96 ± 2.08	7.86 ± 2.23	5.91 ± 1.99
Dice	$.959 \pm .009$	$.954 \pm .009$	$.957 \pm .009$	$.963 \pm .005$	$.955 \pm .010$
Surface Dist.					
AvSD	0.80 ± 0.06	0.89 ± 0.06	0.83 ± 0.05	0.70 ± 0.11	0.83 ± 0.06
MxSD	5.61 ± 2.68	6.00 ± 2.58	5.52 ± 2.56	5.94 ± 1.45	6.42 ± 2.33

Table 2.2: Mean and standard deviation of errors in volume reconstruction for each metric.

(a)

(b)

(c)

(d)
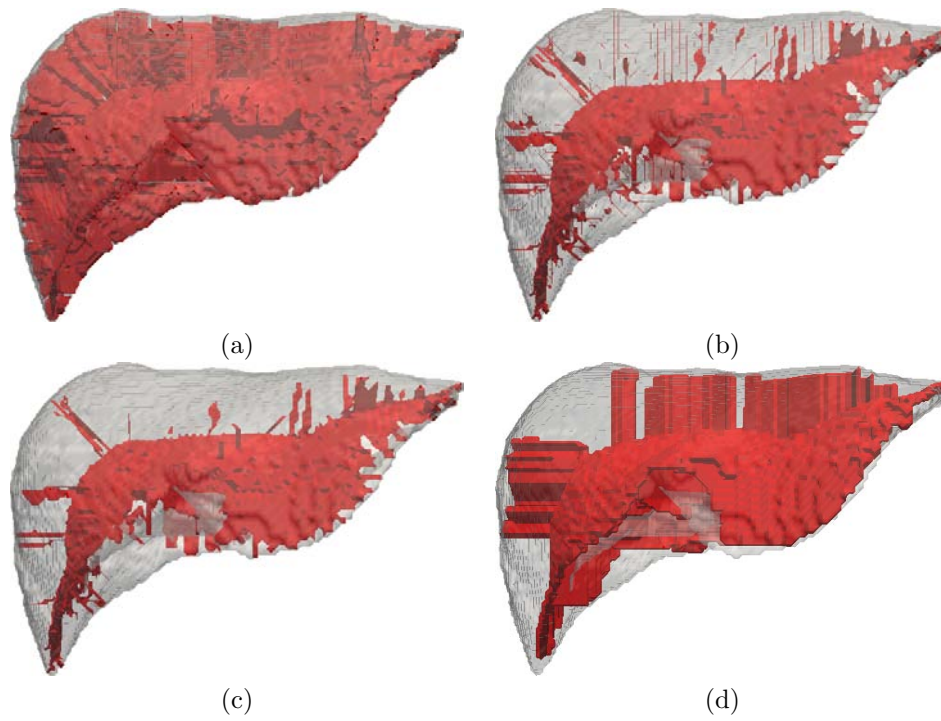
Figure 2.4: Medial manifolds of a healthy liver generated with morphological methods. Th_6 (a), Th_{26} (b), ThP_{26} (c) and Tao_6 (d).
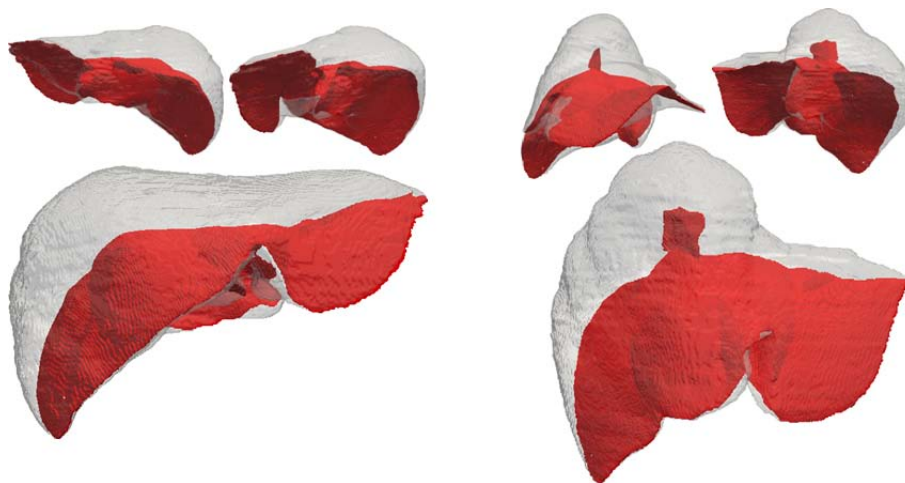
Figure 2.5: Medial Manifolds of a healthy liver (left) and a liver with an unusual lobe (right).
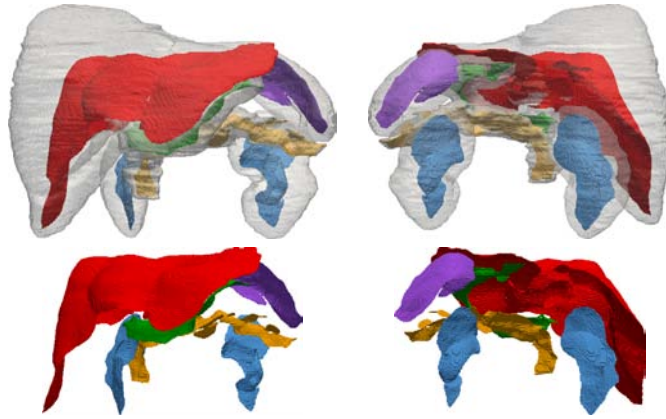
Figure 2.6: Abdominal set of organs and surfaces: liver (red), kidneys (blue), pancreas (yellow), spleen (purple), and stomach (green).

2.4 Discussion

Medial manifolds are powerful descriptors of shapes. The method presented in this chapter allows the computation of medial manifolds without relying in morphological methods nor neighbourhood or surface tests. Additionally, it can be seamlessly implemented regardless of the dimension of the embedding space.

One drawback of the ridge operator is that anywhere the structure tensor does not have a clear predominant direction, the creaseness response decreases. This may happen at points where two medial manifolds join and can introduce holes on the medial surface that violate the homotopy principle. Such holes are exclusively localized at self-intersections, and although can removed by means of a closing operator, a energy map that is to be used to compute medial manifolds, should produce as much constant values as possible in all the medial manifold. To have lower values near intersections might generate medial manifolds that do not maintain the homotopy property. If we want to generate medial surfaces that do not have reduced intensity at intersections, we need an improved version of the medial map.

The performance of our method has been compared to current morphological thinning methods in terms of the quality of medial manifolds and their capability to recover the original volume. For the first experiment a battery of synthetic shapes covering different medial topologies and volume thickness has been generated. For the second one, we have used a public database of CT volumes of livers, including pathological cases with unusual deformations. The following interesting points are derived from our experiments.

The geometry of medial manifolds obtained using morphological methods strongly depends on the description of pixel neighbourhoods. Besides, they are prone to include spurious extra branches that require a further pruning. Experiments on synthetic surfaces show that the performance depends on both medial surface topology and

volume thickness. Although there are not significant differences among methods in terms of reconstruction capabilities, in medical applications extra structures hinder the identification of abnormal or pathological structures.

The proposed method has several advantages over thinning strategies. It performs equally across medial topologies and volume thickness. The resulting medial surfaces are of greater simplicity than the generated by thinning methods. Although having this minimalistic property, the resulting medial manifolds are suitable for locating unusual pathological shapes and properly restore original volumes. We conclude that our methodology reaches the best compromise between simplicity in geometry and capability for restoring the original volumetric shape.

Any simplification of a medial surface results in a drop in reconstruction quality as illustrated in the images of fig. 2.7. Fig. 2.7(a) shows a medial surface of a liver with a pruned version removing the top branch in light red. Fig. 2.7(b) shows the volumes reconstructed using the pruned surface (light red), as well as, the complete one (transparent black). In this case, the pruned surface cannot reconstruct the external part of the superior lobe of the liver. This drop in accuracy is hard to relate to the simplification process because the branching topology of thinning-based medial manifolds is not always related to the anatomy curvature (concavity-convexity pattern). A main advantage of GSM2 medial surfaces is that their branches are linked to the shape concavities due to the geometrical and normalized nature of the operator. In this context, GSM2 manifolds can be simplified (pruned) ensuring that the loss of reconstruction power will be minimum [100].

(a)   (b)
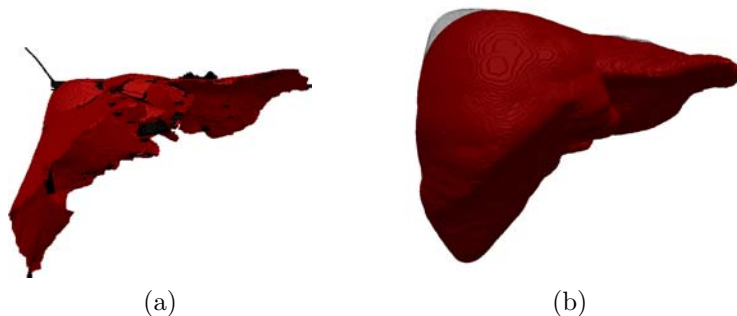
Figure 2.7: Impact of pruning in reconstructed volumes: medial manifolds (a) and reconstructed volumes (b).

The GSM2 medial map represents a clear improvement over NRM, showing improved performance at manifold intersections while retaining the normalized properties of NRM. However, the NMS step still limits the binarization to a single direction around auto-intersections. Even if the medial map achieves a uniform response at branches, binarization using NMS is likely to break branch connectivity. The NMS step keeps points achieving a local maxima along a direction that represents the normal to medial surfaces. It follows that NMS is consistent as far as surfaces have a well-defined unique normal vector that can be computed by means of the structure tensor. Branches are loci of surface self-intersections and, thus, their normal space

is generated by the normal vectors of the surface intersecting folds. This singular feature influences the computation of NMS from both a theoretical and a practical point of view. On one hand, from a theoretical point of view, the definition of NMS should take into account multiple search directions at branching points. On the other hand, the primary eigenvector of the structure tensor used to compute NMS provides an average of the folds normal vectors. This average does not have to be, in practice, perpendicular to any of the intersecting fold and, thus, the ridge map is unlikely to attain a maximum in that direction. This represents a limitation at auto-intersections, which might present small holes due to a wrong direction for NMS. Now, with a continuous ridge map with good behavior at intersections, we need to improve the binarization step so that the second step does not hinder the performance of the medial surface computation. This problem will be addressed in the next chapter.

Finally, regarding computational efficiency, our method is up to 5 times faster than thinning strategies. Unlike parallelization of topological strategies which require special treatment of topological constrains [7, 68], our code is straightforward to parallelize, even on GPU. It follows that our method could achieve the real-time speeds that clinical applications need. Parallellization of GSM is approached in the next chapter.

Chapter 3

A Decoupled Binarization for Efficient Resolution of Branching Singularities

The properties of the medial manifolds strongly depend on the formulation of the energy function, as well as the definition of its singular points. A main concern is that the identification of singular points is prone to become unstable in numeric discrete implementations. Almost all methods are based on the distance map to the object boundary. Few embed medial manifold computation into the context of shocks of the partial differential equation defining distance maps [36]. A main disadvantage of the methods presented in the previous chapter is that they might suffer from common pitfalls of the ridge detection algorithms, which can fail at medial self-intersecting branches as the direction of the ridge is not properly defined.

This chapter addresses the computation of medial branches through the introduction of a binarization strategy inspired in algebraic principles. Medial manifolds are defined as the closure of the locus of centers of maximal inscribed spheres tangent to the surface in at least two points [10]. Their branches are singular loci that can be algebraically characterized by the degree of tangency of the inscribed sphere [16]. This algebraic description has already been used to classify medial branches transitions under boundary deformations [32]. In the context of algebraic geometry, singular points are of special interest and there is a rich literature on their properties and resolution.

We use algebraic geometry tools for decoupling branching points of NMS ridge-based approaches [98, 99] by means of singularity blowing up [41, 44]. Each singular point is locally unfolded by spanning the underlying space adding the projective space of surface normal directions. In such spanned space, medial folds do not intersect [44] and, thus, general rules and image processing tools can be applied. In particular, each crossing fold can be binarized using NMS in the decoupled spanned space and back-projected to the original space to produce a stable medial surface. A main requirement for its use in real-time applications, it is an implementation allowing efficient processing of large volumes. We also present an efficient parallel algorithm for computing the blow-up using standard image processing tools. In order to illustrate

the benefits of the presented method, we have applied it to improve the ridge-based method presented in the previous chapter.

This chapter contributes to the computation of medial surfaces for anatomical shapes with the following two ideas:

1. We present here an original approach for improving the computation of medial surfaces in volumetric domains based on ridge operators, so that they present a stable branch geometry that properly describes the geometry of the volume boundary. We also include an efficient implementation based on CPU-GPU parallel computing.

2. We extend the synthetic database of medial shapes and surface to include different degrees of perturbation. These perturbations can be used to test the robustness of the methods against different shape noise.

The rest of this chapter is organized as follows: section 3.1 describes the binarization strategy for the resolution of singularities and the implementation details in both CPU and GPU. Section 3.2 presents the validation protocol, synthetic database and metrics for benchmarking medial map methods. Section 3.3 provides information about the validation results and finally section 3.4 includes some thoughts and remarks about the techniques presented.

3.1   Medial Surfaces Preserving Branches

Even if the medial map achieves a uniform response at branches, binarization using NMS is likely to break branch connectivity. The NMS step keeps points achieving a local maximum along a direction that represents the normal to medial surfaces. It follows that NMS is consistent as far as surfaces have a well-defined unique normal vector that can be computed by means of the structure tensor. Branches are loci of surface self-intersections and, thus, their normal space is generated by the normal vectors of the surface intersecting folds. This singular feature influences the computation of NMS from, both, a theoretical and a practical point of view. On one hand, from a theoretical point of view, the definition of NMS should take into account multiple search directions at branching points. On the other hand, the primary eigenvector of the structure tensor used to compute NMS provides an average of the folds normal vectors. This average does not have to be, in practice, perpendicular to any of the intersecting folds and, thus, the ridge map is unlikely to attain a maximum in that direction.

Figure 3.1 shows NMS artefact at branches for a 2D cut of a liver. We show the response to GSM2 in the left image, the $ST_{\rho,\sigma}(GSM2)$ primary eigenvector for computation of NMS and the NMS map before thresholding. Even if the medial response preserves branch connectivity, NMS breaks it, as the right image close-up shows. This is due to a deficient search direction given by the $ST_{\rho,\sigma}(GSM2)$ primary eigenvector, which fails to be oriented along neither of the branch intersecting segments.
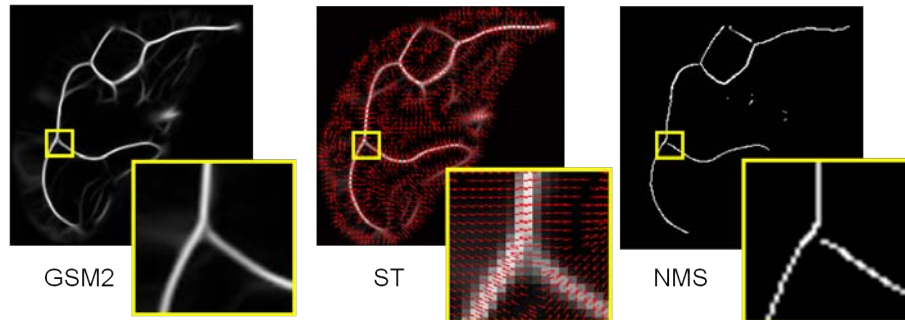
Figure 3.1: Rupture of branch connectivity arising from NMS binarization. Left: GSM2 response. Center: Structure tensor orientations. Right: NMS binarization with broken connectivity.

3.1.1 Resolution of Singularities by BlowUps

From a geometric point of view, branching points are singular points in the sense that the co-dimension of the variety at that point is higher than at the remaining regular points. Singular points commonly arise in the context of algebraic varieties (i.e. zero-sets of a polynomial) as points of multiplicity higher than one. Given that their geometric properties are particular and standard tools of differential geometry do not apply, resolution of singularities has been extensively studied. In the context of algebraic geometry, resolution of singularities for a given algebraic variety X tackles with the problem of finding a non-singular variety X' such that there is a surjective differential map $\pi : X' \to X$. In plain words, the desingularization of X is a variety regular (smooth) everywhere probably living in a higher dimensional space such that its projection onto X produces its singularities [41].

Blowups are the algebraic tool for constructing resolution of singularities. Blowups are transformations that iteratively untie each singularity of the variety and it is guaranteed (by Hironaka theorem [44]) that in finite number of steps the variety is resolved. Each blowup is formulated around a singular submanifold of X (called center of the blow-up) in terms of its normal space as follows [41]. Let us assume that $X \subset W(=\simeq \mathbb{R}^n)$ and let $Z \subset X$ be a submanifold of singular points of dim $Z = d$. For any $a \in Z$, the ambient space W can be locally decomposed as $W = Z \times U \simeq \mathbb{R}^d \times \mathbb{R}^{n-d}$, for U a submanifold transversal to Z of complementary dimension $n - d$. Write points $w \in W$ as pairs $w = (w_1, w_2)$ with $w_1 \in Z$ and $w_2 \in U$ and consider the projective space of lines through a in U, $\mathbb{P}(U) = \mathbb{P}^{n-d-1}$. Then, the blowup is the closure of:

$$\Lambda = \{(w, l_w),\ w \in W \setminus Z, l_w \in \mathbb{P}(U)\} \subset W \times \mathbb{P}^{n-d-1} \qquad (3.1)$$

and $\pi : W \times \mathbb{P}^{n-d-1} \longrightarrow W$ is given by the projection onto the first factor. Around the singular point $a \in Z \subset X$, $\pi^{-1}(X)$ assigns points $(a, l_w(a))$ for $l_w(a)$ a line normal to X at a. Intuitively, the blowup unties X by adding coordinates that represent the normal space at each point of the variety. An important remark from a practical point of view is that in the case of self-intersection of folds with distinct normal vectors, a single blowup is enough to resolve each singularity.

Figure 3.2(a) illustrates the blow up of the curve $X = \{-x^3 + 3x^2 = y^2\}$ in the plane $W = \mathbb{R}^2$. Since in this case the center $Z = \{(0,0)\}$ is of codimension 2, the blowup space is $\mathbb{R}^2 \times \mathbb{P}^1 = \mathbb{R}^2 \times \mathbb{R} \cup \{\infty\}$ and can be identified with $X' = \{xz - y = 0\}$. The z-axis of $\mathbb{R}^2 \times \mathbb{P}^1$ represents the directions of all lines through $a = (0,0)$. In particular, the 2 normal lines of X at $(0,0)$ (plotted in red dashed) are lifted to the points $(0,0,\tan(\theta_1))$ and $(0,0,\tan(\theta_2))$ for θ_1 and θ_2 the directions of the 2 normal lines. Since $\theta_1 \neq \theta_2$, the two branches crossing at Z are completely unfolded in the blowup space and, thus, X' is regular.

(a)   (b)
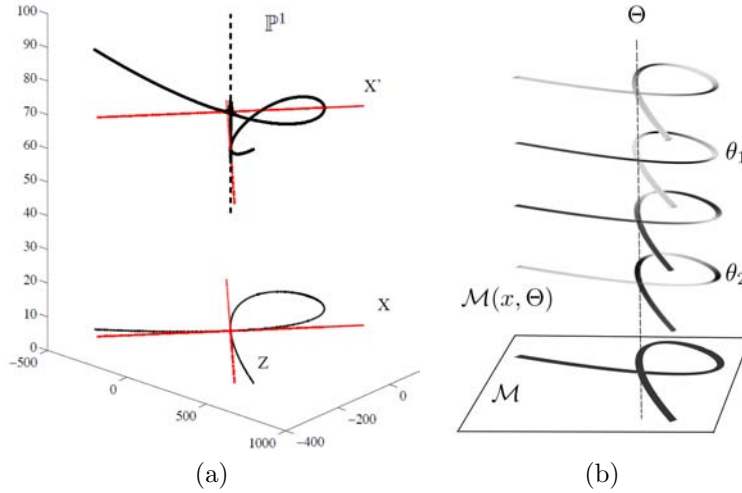
Figure 3.2: Scheme of the Blowup of a curve in the plane: analytic blowup (a). Blow-up space implementation using steerable filters (b).

3.1.2 Computation of BlowUps using Image Processing Tools

For algebraic varieties given explicitly as zero-sets of a polynomial, there exist generic computational algorithms for implementing blowups [11]. However in the case of computation of medial surfaces from anatomical volumes, surfaces are local maxima of functions given in digital format by medial maps and without a polynomial formulation. In this section, we explain how to implement blowups for medial surfaces implicitly given by local maxima of a medial map, which we will denote by $\mathcal{M}$.

A blowup is completely specified by defining its center Z and the projective space of directions, $\mathbb{P}^{n-d-1}$, of the complementary manifold. The center of each blowup is given by a connected submanifold of singular points of X. Singular points arise from X self-intersections and are characterized by an increase of the variety codimension (normal space dimension) at Z. The eigenvalue decomposition of the structure tensor $ST_{\rho,\sigma}(\mathcal{M})$ describes the geometry of the image level sets and it is commonly used to detect their singular points (corners, junctions and boundary points). Eigenvectors are aligned with the direction of extreme contrast change and eigenvalues are given by the amount of contrast change. At a regular point, the primary eigenvector is normal

to level-sets and its eigenvalue is significantly larger than the other two. Meanwhile, self-intersecting level-sets are characterized by similar eigenvalues and corresponding eigenvectors normal to each of the branches. It follows that the ratio between eigenvalues has been exhaustively used in image processing for detecting singular points. Given that, our centers are given by intersection of two or more regular surfaces, we have chosen the corner detector introduced in [82]:

$$\frac{\lambda_1 \lambda_2}{\lambda_1 + \lambda_2 + \epsilon} \tag{3.2}$$

for $\lambda_1 \geq \lambda_2 \geq \lambda_3$ the eigenvalues of the structure tensor. The operator (3.2) gives a high response at branches, as well as surface boundary end-points. In order to remove response at surface boundaries, we iterate (3.2) twice. Given that the response to (3.2) is regular at boundaries, while it keeps the branching structure at self-intersections, one iteration suffices to remove non-branching responses as exemplified in Fig. 3.3.

(a)   (b)   (c)
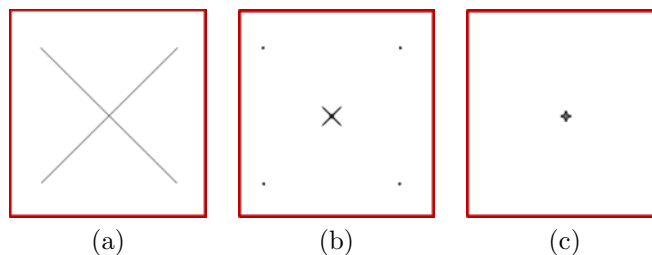
Figure 3.3: Blow up implementation, singularity localization using corner detectors. Example of a first order singularity (a). First corner detection phase (b). Second corner detection over image generated at (b), (c).

Therefore, the set of singular points of X is given by applying twice the operator (3.2) to the distance map, D, to the object boundary:

$$Z := T(T(D)) \tag{3.3}$$

The images in figure 3.3 illustrate the computation of the set of singular points using the double operator (3.3). The leftmost image show a cross with 4 end-points, the central image the response $T(D)$ and the rightmost image $Z = T(T(D))$. Gray intensities are shown inverted (the darkest, the largest) for visualization purposes. The first iteration of the corner detector has response at the cross central branching point and the cross end-points of a similar value, note the response at intersection and end of branches. Their only difference is in their shape, which is round at end points and like the cross itself at the branching point. It follows that a second iteration of the corner operator removes end-point responses while still preserving a clear response at the branch site. The rightmost image in Fig 3.3 shows that this time the response is located exclusively at the singularity.

Concerning the definition of surface orientations, streerable filters constitute a useful tool since they decouple the space of possible orientations for medial surfaces. Given that medial surfaces are local maxima of $\mathcal{M}$, the convolution:

$$\mathcal{M}(x, \Theta) := \partial_z^2 g_\sigma^\Theta * \mathcal{M} \tag{3.4}$$

defines a function:

$$\begin{array}{ccc} \mathbb{R}^n \times \mathbb{P}^{n-1} & \longrightarrow & \mathbb{R} \\ (x, \Theta) & \mapsto & \mathcal{M}(x, \Theta) \end{array} \tag{3.5}$$

that restricted to the medial manifold implicitly defines its blowup.

For each orientation, Θ_0, the convolution (3.4) is only sensitive (i.e. attains its maximum values) to points of the medial surface oriented perpendicularly to the direction given by Θ_0. Therefore, the blowup volume, $\mathcal{M}(x, \Theta_0)$, is a regular surface with a well defined tangent space. Consequently, the NMS operator given by (2.13) applied separately to each level $\mathcal{M}(x, \Theta_0)$ properly restores all medial branches perpendicular to Θ_0. This leads to the following implementation of BlowUp Maps (which we will note $\mathcal{BUM}$) based on steerable filter:

$$\begin{aligned} \mathcal{BUM}(x) :=& max_{i,j} \left(NMS(\mathcal{M}(x, \Theta_{ij})) \right) = \\ =& max_{i,j} \left(NMS(\partial_z^2 g_\sigma^{\Theta_{ij}} * \mathcal{M}) \right) \end{aligned} \tag{3.6}$$

for $\partial_z^2 g_\sigma^{\Theta_{ij}}$ given as in (2.11).

Figure 3.4 illustrates the implementation of the space decoupling provided by $\mathcal{BUM}$ convolution with an oriented bank of steerable filters for the lace curve of fig. Fig:BlowUp. At a given orientation level, curves of maximum response to the filter $\partial_z^2 g_\sigma^\Theta$ are regular sets without branches (fig. Fig:BlowUp-Vectors, left image). It follows that the principal eigenvector of their structure tensor has a well defined direction in the original singular point, allowing a NMS binarization without ambiguities.

The rightmost image in figure 3.2 illustrates the blowup defined using steerable filters for the case of a shape having as medial surface the lace curve X shown in Fig. 3.2 left hand side. Like blow-up localization using corner operators, gray intensities are shown inverted (the darkest, the largest) for visualization purposes. The bottom image shows a 2D medial map having X as maximal variety. Its blowup variety X' is given by the 3D volume $\mathcal{M}(x, \Theta)$ shown above the medial image. We show several cuts of the volume corresponding to some orientations of the steerable filters Θ_{ij}. The orientations achieving maximum response at the curve singular point are labelled θ_1, θ_2 and correspond to the curve branch normal directions at 45 and -45 degrees, respectively. First we note that they are at different levels of the image volume $\mathcal{M}(x, \Theta)$ and, thus, the blowup manifold projecting onto X is regular. Second, the corresponding image cuts (shown in side images) have curves of maximal response regular without branches, so that, the direction defining NMS is well-defined (as illustrated in figure 3.4).

3.1.3   Efficient Parallelization of BlowUps

Our implementation of blowups can be split in 3 stages (see table 3.1): blowup location, space decoupling and NMS computation. The most demanding steps are space decoupling and NMS computation. Space decoupling requires convolution of the volume with a filter bank of gaussians covering all possible orientations in 3D. Binarization using NMS has suboptimal performance due to a voxel-to-voxel eigenvalue decomposition of the structure tensor computed for each response to the filter bank.
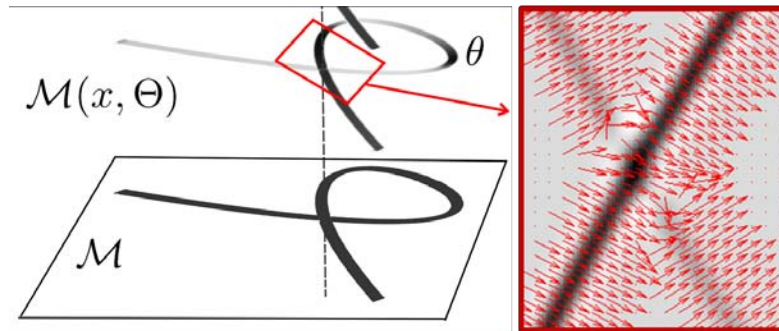
Figure 3.4: Blowup decoupling, $\mathcal{M}(x,\Theta)$ of a plane curve $\mathcal{M}$ (left), and detail of the vector indicating direction of greatest change for the response at a given orientation θ (right).

Given that convolution is independent for each filter and eigenvalue decomposition is a voxel-wise operation, both steps can be easily parallelized. In order to make the most of the computational resources available in a standard PC, we have chosen a combined CPU-GPU parallelization for MatLab.

Task	Implementation	Cost	Parallelized
BlowUp location	Tomasi corner detection	Low	No
Space decoupling	Filter bank convolution	High	Yes (GPU)
NMS computation	Structural tensor computation	High	Yes (CPU)

Table 3.1: Blowup implementation stages.

GPU Space Decoupling

The simplest approach for parallelization is to perform each space decoupling in a separate CPU core. Using Matlab's Parallel computing toolbox, we distribute each decoupling computational task into independent child worker processes. Matlab then schedules workloads, issues execution request and retrieves the results with no user intervention. This approach, while simple, might require an enormous amount of host RAM memory for its execution because each worker is an almost complete copy of the program, which shares some data with its parent. Therefore, its use becomes impractical as soon as the size of the input volumes increases, as it is the case of 3D anatomical volumes.

An alternative to Matlab CPU parallelization is the use of GPU programming. Consumer grade graphic cards feature a high number of computing threads. Individually, these threads are slower in comparison to a CPU core. However, GPUs are good at parallelism since there are more cores available for computation [79]. Thus, for large amounts of data, the benefits of GPU convolution become apparent. Finally, fast tools for GPU computing in Matlab exist nowadays [73] , so experimentation is now possible.

Since the GPU is a separate processor, with dedicated memory, we have to copy the input tensor volumes from the host into the GPU before computation starts. Moreover, after execution the results must be transferred back into the host. Given enough device memory available, it would be possible to convolve the image with the whole filter bank in a single GPU computation operation. However, since our GPU has less memory than our host RAM, we can only convolve the input image with a single filter at each time. This introduces idle computation stages due to these transfers [25], but the lower global execution time in GPU computation validates this approach.

NMS computation

The eigenvalue decomposition is based on an existing implementation by [46]. Due to the algebraic properties of the decomposition, there is no spatial dependency between voxels. For this reason, it is possible to divide the original tensor volume in separate data blocks that the CPU can process in parallel. Next, we reassemble the results into a final volume. Figure 3.5 shows an overview of the proposed parallelization stages.

(a) Tensor Volume   (b) Voxel vector   (c) Block distribution

(d) Execution Flow   (e) Result
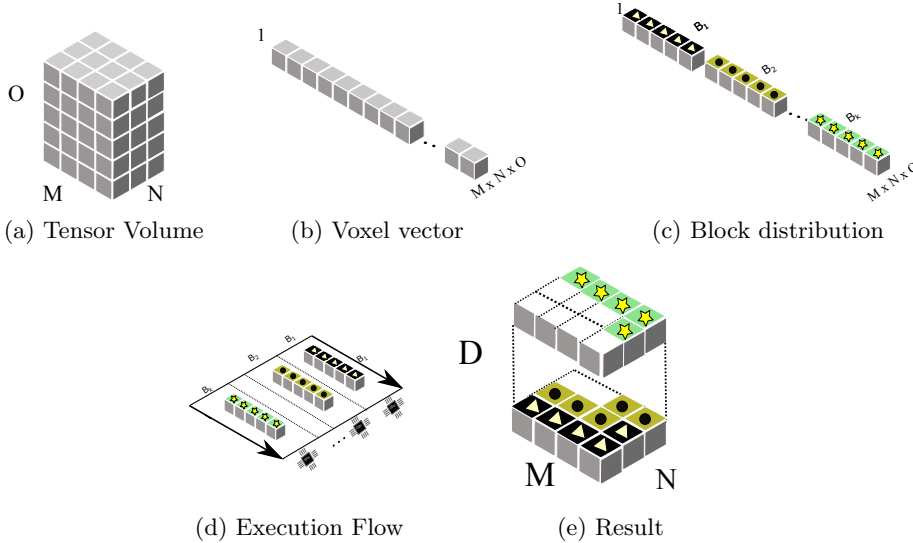
Figure 3.5: Parallel decomposition for NMS computation

Given a tensor of size $M \cdot N \cdot O$ voxels, we can represent this volume as a one-dimensional vector of voxels like in figure 3.5b. Assuming K_{cores} CPU computational cores, we can distribute up to K_{cores} blocks, one for each core, with a size for each block, B_i $i = 1, \ldots, K_{cores}$, given by:

$$B_i = \begin{cases} \left[\frac{v}{K_{cores}}\right] & i = 1..K_{cores} - 1 \\ v - (K_{cores} - 1)\left[\frac{v}{K_{cores}}\right] & \text{otherwise} \end{cases} \tag{3.7}$$

Where $[\cdot]$ is the mathematical operation of rounding a rational number to the

nearest integer. In the reference figure 3.5a, tensor size is $M = 4, N = 3, D = 5$, thus $v = 60$. For a $K_{cores} = 12$ cores CPU, we split data into 12 blocks, namely $B_1, B_2, ...B_{12}$. In this case, all blocks would have the same amount of voxels, that is, 5 voxels. In another example, a tensor with size $M = 5, N = 5, D = 5$ would be split into 11 blocks of 6 voxels ($B_1, ..., B_{11}$) and a final block of $B_{12} = 9$ voxels.

To execute each data block in parallel, we use the *Parallel computing toolbox*. Matlab spawns K_{cores} child processes,each one receiving a corresponding B_i data block. During execution, Matlab handles all task scheduling automatically. Finally, we reassemble the results with the *reshape* utility of Matlab.

3.2 Extended Validation Framework

Our experiments focus on two different tests for assessing the stability of medial branching and applicability to medical decision support systems. The first test evaluates the stability of the medial surface branches for known volumes undergoing a controlled deformation. The second test explores the capability of medial branches for describing anatomical deformations and the computational efficiency of the medial algorithm.

3.2.1 Medial Branch Stability

Stability of medial branches has been tested on our own synthetic database [1] for medial surface quality evaluation.We recall that our synthetic volumes cover different aspects of medial surface geometry (including different degrees of medial branching) and volume medial representation (uniform and varying radii for the inscribed spheres). The test set of synthetic volumes / surfaces covers different key properties of medial surface generation [74]: 1) preservation of the topology of the original object (homotopy); 2) one-pixel thin structures (thinness); 3) structures equidistant to object boundaries (medialness).

The database described in 2.2.1 has a total number of 120 samples, distributed in 6 families (20 samples each) covering the 3 medial topologies and the 2 volume distance types. For these experiments on branch stability only the multiple topology with variable distance volumes have been used.

We consider that a method for computation of medial surfaces is robust for branch detection if it can detect all branches associated to a given degree of boundary saliency (deformation degree) on the object boundary. The amount of perturbation medial surfaces should detect depends on each specific application and should be an input parameter of the algorithm. Once the parameters for the pruning stage have been set, the method should be able to prune away any branch not corresponding to the minimum degree of perturbation allowed.

Our synthetic experiments have been designed to measure the compromise between detection stability (for a given deformation rate) and spurious spikes arising from smaller perturbations. To such end, the original volumes have been deformed in order to generate branches at specific sites selected on a mesh of the volume boundary.

---

[1]available at http://iam.cvc.uab.es/downloads/medial-surfaces-database

Perturbations of synthetic volumes increase from none to a percentage of the original volume thickness given by the synthetic radial map used to create objects. The position of each selected point, $\overrightarrow{P}$, is modified by a translation δ_P along the boundary normal direction at that point, $\overrightarrow{N}_P$:

$$\overrightarrow{P} \rightarrow \overrightarrow{P} + \delta_P \overrightarrow{N}_P \tag{3.8}$$

for $\delta_P \in [0, D_{max}]$ as illustrated in fig. 3.6.
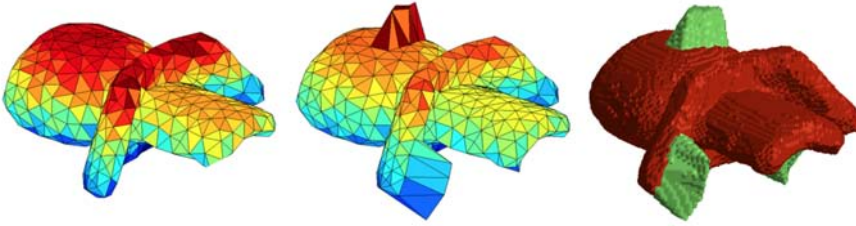
Figure 3.6: Generation of parameterized branches in existing synthetic branches. Original shape in mesh space (left). Branching by displacement of points (middle). Original and modified voxelized shapes in red and green color respectively (right).

Given that for $\delta_P = 0$, we have the original volumes, the connected components of the difference between volumes for $\delta_P = 0$ and $\delta_P > 0$ is the collection of volume spikes, namely $\{VS_i\}_{i=1}^{N_{VS}}$ generated by the deformation process.

Medial surfaces for $\delta_P = 0$ give the baseline accuracy by comparison to the database ground truth surfaces [98]. For $\delta_P > 0$, computed medial surfaces should generate new branches for each volume spike if the deformation size δ_P is large enough to introduce a significant change in volume curvature. Branches not arising from volumetric spikes changing boundary convexity profile are useless and should be as least as possible. The quality of medial branching arising from volumetric spikes has been assessed in terms of spike detection and its accurate localization. Branches arising from the volume deformation are given by the connected components of the difference between medial surfaces for $\delta_P = 0$ and $\delta_P > 0$. We will note them by $\{B_j\}_{j=1}^{N_B}$.

Spike detection rate has been measured in terms of medial branch false and true positives. A branch is considered a true positive if it intersects any of the volume spikes VS_i. In order to measure the impact of false branches arising during volume deformation (i.e. detection capability), we have also considered the percentage of area that true positives and all medial branches represent over ground truth medial surfaces:

1. *True Branches*:

$$TB = \frac{\#\{VS_i \text{ s. t. } \exists B_j, \, B_j \bigcap VS_i \neq \emptyset\}}{N_{VS}} \tag{3.9}$$

   the detection is optimal if $TB = 1$.

2. *Detection Capability*: We measure detection capability by considering the percentage of medial branches area, MBA, as well as, the percentage of true

branches area, TBA. If X denotes the ground truth medial surface and B_j^{TB} denotes a true medial branch, then such area percentages are given by:

$$TBA = 100\frac{\sum \|B_j^{TB}\|}{\|X\|} \quad MBA = 100\frac{\sum_{j=1}^{N_B} \|B_j\|}{\|X\|} \quad (3.10)$$

for $\|\cdot\|$ denoting the area of a surface.

The score MBA measures the total amount of spikes and, in particular, for $\delta_P = 0$ the ones that are not related to any volume deformation. The score TBA indicates the percentage of surface branches that really correspond to volume deformation. The ideal quality plots for TB should present an asymptotic profile converging to 100%. Concerning TBA and MBA plots, they should be equal and have an increasing pattern. Any divergence between TBA and MBA ranges is due to the presence of spikes not linked to the introduced perturbation.

We define spike localization in terms of the distance to the volume spikes, namely d_{VS}, and the ground truth medial surfaces, namely d_X. For each point in computed medial surfaces $y \in Y$, we have that the minimum between $d_X(y)$ and $d_{VS}(y)$ reflects a compromise between between medial branches size and its proximity to a volume spike. Let $DL(y) := min(d_X(y), d_{VS}(y))$ denote such minimum. Then, our localization scores are given by the average (ADL) and maximum (MDL) values of DL over the computed surface:

1. *Spike Localization*:

$$ADL = \frac{1}{\#Y} \sum_{y \in Y} DL(y) \quad MDL = \max_{y \in Y} DL(y) \quad (3.11)$$

	BUM	$GSM2$	Tao_6	ThP_{26}	$CMRep$	SAT
ADL	3.50 ± 1.18	3.43 ± 1.05	4.87 ± 1.24	5.23 ± 1.03	3.76 ± 1.15	3.92 ± 0.9778
MDL	7.86 ± 0.95	8.04 ± 0.84	10.52 ± 2.92	11.81 ± 3.00	9.19 ± 2.71	9.38 ± 1.264

Table 3.2: Localization ranges (mean and standard deviation) for the synthetic volumes

3.2.2   Clinical Applicability

In medical imaging applications the aim is to generate the simplest medial surface that allows recovering the original volume without losing significant voxels. Besides, for its application to diagnosis and treatment planning, algorithms should reach a compromise between accuracy and computational cost.

Reconstruction capabilities have been assessed by comparing volumes recovered from surfaces generated with the different methods to ground truth volumes. Volumes are reconstructed by computing the medial representation [10] with radius given by the values of the distance map on the computed medial surfaces. Let A, B be, respectively, the original and reconstructed volumes and ∂A, ∂B, their boundary surface.

Completeness of reconstructed volumes is assessed using the following volumetric and distance measures:

1. *Volume Overlap Error:*

$$VOE(A, B) = 100 \times \left(1 - 2\frac{\|A \cap B\|}{\|A\| + \|B\|}\right) \qquad (3.12)$$

2. *Maximum Volume Boundary Difference:*

$$MVD = \max\left(\max_{x \in \partial A}(d_{\partial B}(x)), \max_{y \in \partial B}(d_{\partial A}(y))\right) \qquad (3.13)$$

In order to provide a real scenario for the reconstruction tests we have used 15 livers from the SLIVER07 challenge [42] as a source of anatomical volumes. To compare to the Voronoi skeletonization methods SAT and $CMRep$, liver CT meshes were smoothed and decimated to 80% of the triangles using the VTK implementation of the decimation of triangle meshes based on mesh error described in [80].

3.3   Validation Experiments

Our validation protocol for medial surface stability has been applied to the method described in Section 3.1 computed for $\mathcal{M} = GSM2$. In order to assess the improvement in branch recovery, we have also considered $GSM2$ alone. For both cases, the largest connected component was selected. Finally, to compare to other methods, we have also applied it to two thinning methods with pruning and two Voronoi approaches. The thinning methods are a pruned version of the 26-connected neighborhood method (labelled ThP_{26}) described in [74] and the 6-connected scheme (labelled Tao_6) described in [47] that alternates thinning with pruning stages. The Voronoi approaches are the public domain CM-Rep with pruning (labelled $CMRep$) available at [2] and the Scale Axis Transform[3] (labelled SAT) [33].

Our test machine featured an Intel Core i7 3970K hex-core Processor working at 4.2Ghz with 24 GB of RAM. For the GPU experiments, we used a Geforce GTX-550 Ti video card with 1GB VRAM featuring 192 CUDA cores. Blow-ups were computed using the parallelization described in Section 3.1.3, while $GSM2$ used a serial implementation. Concerning morphological approaches, we used the codes described in [74]. These implementations are essentially serial by the nature of thinning approaches (see the Discussion section).

3.3.1   Medial Branch Stability

Figure 3.7 shows an example of the synthetic volumes in the first row and the computed medial surfaces in the remaining rows. We show the deformed volume with its spikes in green and the volume for $\delta_P = 0$ in red. We show computed medial surfaces

---

[2]cmrep.cvs.sourceforge.net/viewvc/cmrep/cmrep/src/VoronoiSkeletonTool.cxx
[3]http://code.google.com/p/mesecina/

in solid meshes and the synthetic volume in semi-transparent color. The shape of surfaces produced using morphological thinning strongly depends on the connectivity rule used. In the absence of pruning, surfaces, in addition, have extra medial axes attached. Although they detect all volume spikes, Th_{26P} produces a bunch of medial axes instead of a clear surface for each spike. The impact of spikes is substantially reduced for Voronoi surfaces, especially for SAT, although medial surfaces still have some irregularities on their boundaries. Finally, ridge-based medial surfaces have a well defined shape matching the original synthetic surface without extra structures. The benefits of BUM for branch recovery are clearly illustrated by the 1st and 4th cases, which upper branch is missing for $GSM2$.

Figure 3.8 plots branch detection rates across volume perturbation. We show average curves computed across all medial surfaces for TP, MBA and TBA. In the case of MBA and TBA, their ranges given by $\pm$ standard deviation are also shown in colored bands. Both energy methods reach a similar compromise between extra structures and true branches. However the detection rate significantly drops without blow-up (from 100% to less than 70%. The impact of extra structures is less than 30%. It is worth noticing that such extra structures do not alter the geometry of medial surfaces(see fig.2.3). They rather correspond to an over detection at surface endings, which increases for blowup surfaces due to some artifacts in the localization of the blowup sites. The behavior of the morphological approaches is substantially different. The capability for proper detection of volume spikes is higher for Tao surfaces, thanks to a higher connectivity (see 2nd row in fig.2.3). However, it introduces a larger area of branches alien to volume deformation (about 60%) and also misses some important branches that should arise for large volume deformation (TP does not reach 100%). Although Th_{26P} has a 100% of detection rate, it presents the lowest ratio of true branches due to a fragmentation in single medial axis instead of a surface branch. Concerning Voronoi approaches, $CMRep$ is the one achieving a best detection capability as MBA and TBA ranges coincide at the cost of some missing branches. SAT performance is close to BUM in terms of branch detection capabilities and presence of extra structures.

Finally, Table 3.2 reports spike localization ranges computed over all shapes and deformation degrees for the four methods. There are not significant differences between the two ridge-based methods, which demonstrates that blowups improve branch without introducing other geometric artifacts. Comparing to morphological methods, we observe a significant increase in localization errors due to extra branches. Finally, both Voronoi methods have a localization capability between morphological thinnings and ridge-based surfaces.

3.3.2 Clinical Applicability

Figure 3.9 illustrates assessment of reconstruction power for clinical applications for two different liver anatomical shapes. Volumes reconstructed using the computed medial surfaces (colored in red) are shown in transparent blue over true anatomical volumes shown in transparent gray. Differences between the reconstructions and the original volumes are better appreciated in volumes colored according to distances between reconstructed and original anatomical volumes.

Reconstruction accuracy of morphological methods varies upon the pruning scheme. The morphological Tao_6 achieves a good reconstruction power at the cost of a high density of branches in medial surfaces. Meanwhile, Th_{26} drops reconstruction power at some parts due to a higher branch sparsity (as illustrated by the first volume). CMReps shows multiple branching artifacts despite the pruning step, although the density of the branches produces acceptable reconstruction power. Increased pruning values also affects the reconstruction power as triangles on the edges of main surfaces are lost. SAT produces results close to BUM but with reduced reconstruction capabilities. A problem of SAT for medical applications is the introduction of medial structures that distort medial topology. This is due to the smoothing multiplicative factor applied to the object boundary distance map, which at boundary areas presenting valleys can generate medial structures that partially lie outside of boundary. This artifact is exemplified in fig. 3.11 where we can see that the medial surface (red) is visible partially outside the liver boundary near the valley where the falciform ligament divides the liver in two anatomical segments, a relevant landmark in living donor liver transplants. Similar artifacts happen also in the lower surface of the liver, where there is a number of similar valleys in the liver boundary. We note that in the absence of branch blowup, the energy-based $GSM2$ has a poorer reconstruction power. This drop especially increases in the presence of prominent convexities, like the one shown in the right liver.

The benefit of branch blowup is better illustrated in the images of fig.3.10 that present the common pitfall of ridge-based branch missing and its negative effects in restoration of volume finest details. As before, we show medial surfaces as well as volumes colored according to distance errors for $GSM2$ (left volumes) and BUM (right volumes). Small medial branches at the top of the liver are completely missing for $GSM2$ surface. This introduces a large error (up to 18 pixels) in $GSM2$ reconstruction at such area. Meanwhile, BUM surfaces present a continuous connected junction profile everywhere and, in particular, top branches are preserved. Such branches contribute to the reconstruction of the top finest anatomical details, as shown in the colored volumes.

Table 3.3 reports the statistical ranges for all methods and measures computed for the 15 livers. Gross differences between volumes are detected by VOE and, in spite of errors at prominent lobes, none of the cases seem to be significantly better. In medical applications, restoring local deformations can be important for early diagnosis. In this context, the surface distance score MVD is suitable for detection of local differences. Our approach BUM results is the best performer and the thinning Tao_6 the worst one. Although a bit better than morphological thinning, both Voronoi methods are behind energy-based methods and present the largest variability across liver volumes.

Computational times required for each method are given in Table 3.4. We report execution times for each algorithm, as well as, the average (μ) and standard deviations (σ) for the whole data-set in last rows. For Voronoi methods working with surface meshes, times include the conversion from volume voxels to mesh surfaces and we also report the number of mesh triangles. Although all algorithms scale linearly in relation to the size of the input volume, their computational execution time ranges are vastly different. In fact, both Tao_6 and $Th26P$ are slower by order of thousands of seconds in comparison to $GSM2$ and BUM. This is the expected behavior, as $Th26P$

	BUM	$GSM2$	Tao_6	ThP_{26}	$CMRep$	SAT
VOE	2.3 ± 0.5	2.2 ± 0.5	2.1 ± 0.4	4.4 ± 0.9	4.4 ± 9.8	3.7 ± 6.9
MVD	6.5 ± 4.3	8.3 ± 3.9	8.9 ± 3.5	12.3 ± 5.6	8.5 ± 13.2	9.3 ± 14.0

Table 3.3: Mean and standard deviation of errors in volume reconstruction for each metric.

and Tao_6 depend on the volume thickness, unlike filter-bank approaches ($GSM2$, BUM). Moreover, in the case of Tao_6, the algorithm must go through a set of voxel-suppression tests to ensure to enforce valid topologies, which further decreases overall performance. Finally, both $Th26P$ and Tao_6 depend on the surface angular topology, which means that for complex surfaces algorithm speed will be affected. Voronoi-based methods are faster than methods based on morphological thinning but slower than energy-based methods. It is worth mentioning that SAT is significantly better than CMRep and achieves a competitive computational time comparable to the one achieved by energy-based methods. These last methods produce medial surfaces of full resolution volumes in the fastest time and achieving the best reconstruction power in the case of BUM.

Liver	Vol. Size	Triangles	Tao_6	$Th26P$	$CMRep$	SAT	$GSM2$	BUM
01	208 x 210 x 163	14038	120960	10944	2985	233	56	233
02	139 x 172 x 138	15038	35780	3654	2994	204	28	112
03	139 x 149 x 132	11770	28050	2860	2686	211	21	107
04	244 x 244 x 179	27172	183630	16200	7577	282	79	193
05	264 x 197 x 239	30056	259670	17345	8909	283	95	211
06	204 x 131 x 144	11802	37320	3718	2697	196	33	139
07	255 x 222 x 203	34452	214970	16445	9968	268	101	202
08	261 x 249 x 242	43868	349850	23369	14599	336	139	246
09	258 x 213 x 213	29844	222660	14388	8674	269	87	204
10	212 x 227 x 245	32428	262570	17826	9456	280	104	205
11	215 x 227 x 212	25896	241760	16153	6958	262	84	189
12	145 x 164 x 175	13368	42300	4289	2832	209	41	152
13	208 x 232 x 250	33488	236190	15114	9269	269	89	124
14	275 x 364 x 246	45748	368720	26547	15458	382	195	340
15	162 x 185 x 122	13950	46200	4263	2856	201	27	119
μ			176710	12874	7194	259	79	185
$\pm\sigma$			117130	7579	4303	52	48	62

Table 3.4: Computational Cost: size is in voxels, times in seconds, μ stands for mean and $\pm\sigma$ for standard deviation

3.4   Discussion

A main limitation for the use of medial surfaces in applications oriented to clinical diagnosis is the presence of spurious branches or unwanted media surface manifolds which do not actually convey any anatomic description. On one hand, a complex medial medial geometry complicates modelling organ populations for statistical analysis or correspondence mapping. On the other hand, hinders easy definition of tubular coordinates providing correspondence across different volumes, which constitutes a main advantage of medial representations over other volumetric models. Any method that reaches a compromise between the number of medial structures, their stability against noise in the boundary and reconstruction capability would constitute an excellent basis for using medial representations in the medical imaging field.

We describe a new method for medial computation for volumetric data based on ridge operators and blowup of singularity points that shows a good balance between the above characteristics. Aiming at its use in medical applications, we provide a hybrid CPU-GPU parallel implementation for standard PC's. In addition, we present a comparison of the stability of several medial surface methods against the presence of spurious branches and their capability for reconstructing the original volume. The comparison bases on a validation protocol that includes a database of synthetic 3D volumes with ground truth medial surfaces that cover several topology families to provide realistic scenarios of medial surface computation.

Our experiments compare energy based, morphologic approaches and Voronoi mesh methods and show the benefits of using blowup resolution of medial branches in ridge-based approaches. Morphological methods present a complex medial branching with high instability under deformation of the volume boundary. Voronoi methods achieve competitive results but require several pre-processing steps prone to introduce errors when dealing with volumetric medical data. In addition, some of them are prone to distort medial topology. Energy based methods complemented with resolution of singularities achieve a good balance between branching stability, simplicity and capability for reconstructing volume boundary finest details. Such details might be good indicators of an illness first stages and, thus, a medial map able to capture such variations in shape without introducing unnecessary complexity will be a solid basis for early diagnosis and treatment progress assessment.

An important concern for the use of methodologies in real clinical settings is their computational cost. In this context, energy based methods are easier to parallelize in modern hardware than morphological methodologies. Morphological methodologies are based on an iterative removal of simple voxels that do not alter the volume topology. The removal of simple voxels depends on accessing an ordered list where the best candidate for removal is stored first. Since the removal of a voxel from the object, changes the local topology on its neighborhood, the voxels in the vicinity have to be reevaluated and inserted in the list if needed. It follows that voxels can only be removed one by one, and they are tested several times, as their neighbors are removed. This limits the parallelization of the method without deep changes in the algorithm. On the side of voronoi methods, the performance of CMrep depends on the number of triangles present on the mesh. In consequence, the decimation factor applied to the mesh is a key value in time vs. accuracy scenarios. The Scale Axis Transform

scales well with triangle size, with its performance depending on the parameters used in the computation.

The presented hybrid approach featuring GPU convolution has similar performance in comparison to a pure CPU multicore implementation. However, this has a cost in the form of considerable high memory usage. For instance, the multicore+GPU approach peaks at 5GB RAM on average, whereas the pure multicore method requires up to 14 GB RAM to run. Moreover,we face restrictions in the form of limited device memory, together with data transfers overhead. For this reason, the GPU implementation is not as optimal as it could be. Finally, not all volumes fit on device memory, so this approach is not always available. Still, we feel that the hybrid approach is a good compromise between speed and memory requirements and its improvement is a topic in our future research.
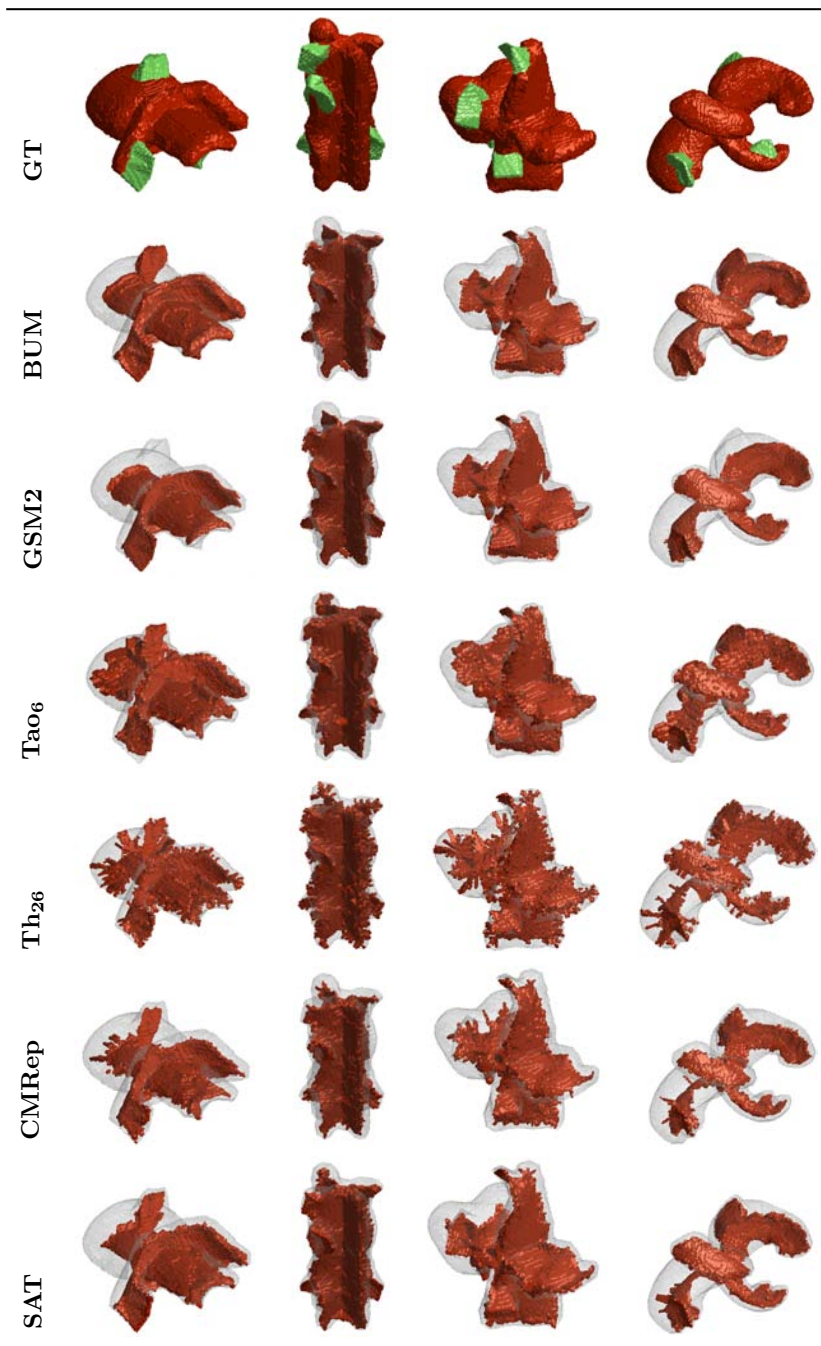
Figure 3.7: Assessment of medial stability. First row shows the deformed synthetic volumes, 2nd and 3rd computed medial surfaces and stability scores.
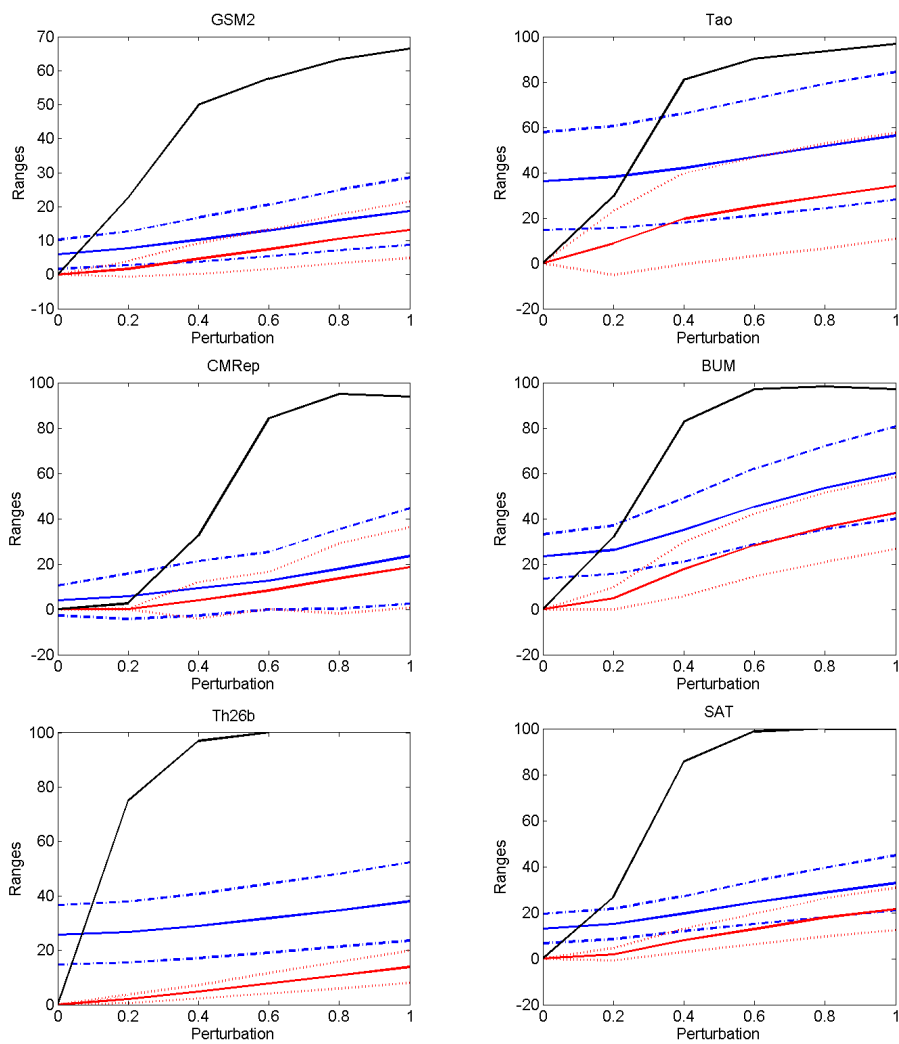
Figure 3.8: Medial stability scores and detection rates, energy-based methods on left images, morphological thinning on middle images and Voronoi-like on right images.
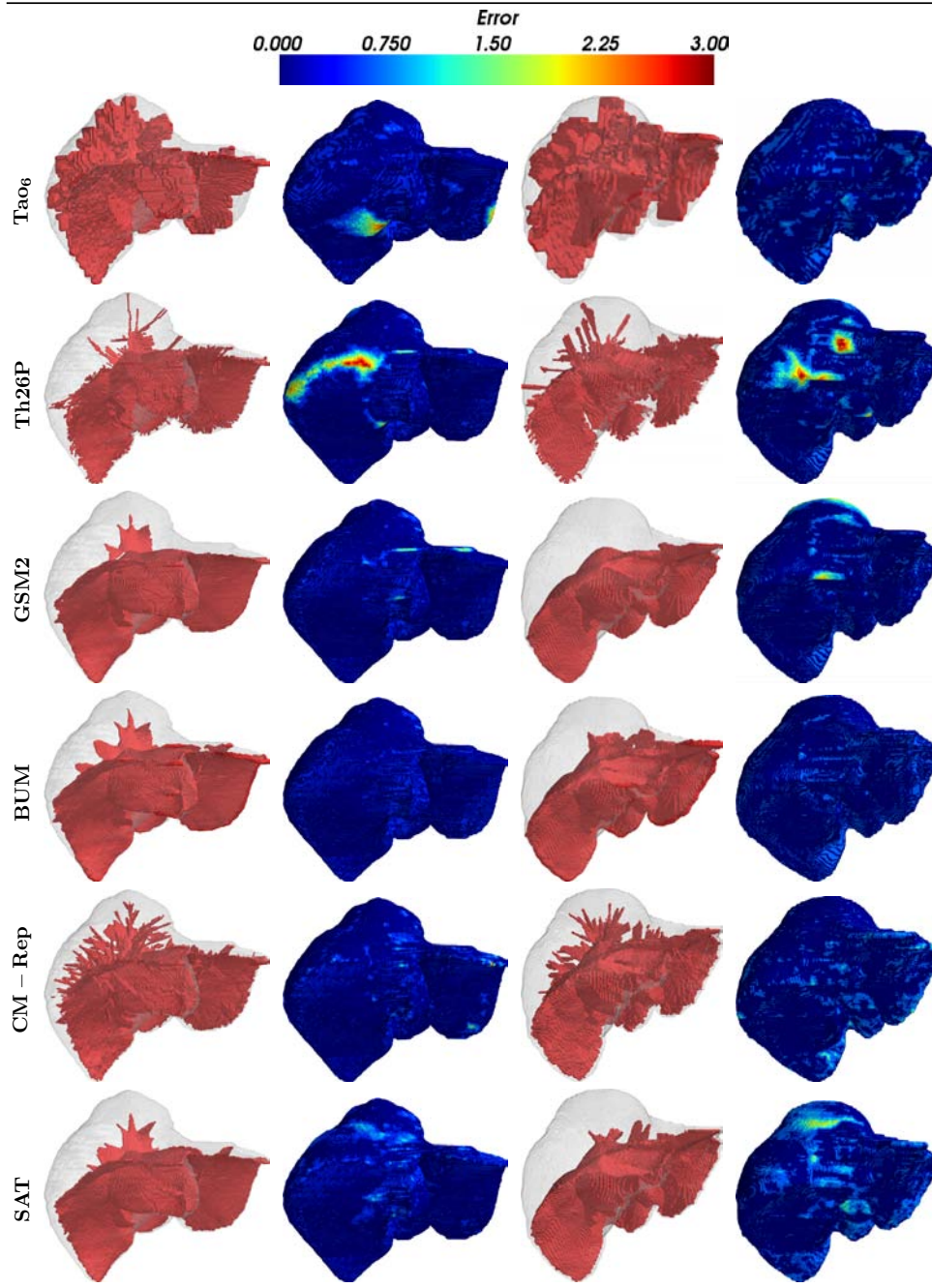
Figure 3.9: Reconstruction Power for Clinical Applications. Volumes reconstructed using computed medial surfaces and distance error between reconstructed and original liver volumes.
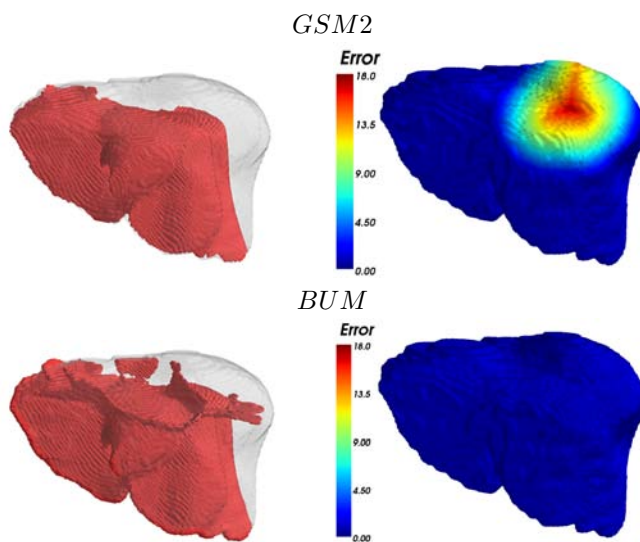
Figure 3.10: Benefits of BUM for restoring medial junctions. Medial surfaces and distance errors for $GSM2$, leftmost images, and BUM, rightmost images.

Figure 3.11: SAT generated artifacts in liver natural folds. Left: medial surface (red) lying outside of liver boundary (white) near the falciform ligament. Right: sliced volume with artifacts shown in blue.

Chapter 4

Volumetric Anatomical Coordinates via Harmonic Maps and Medial Information

In clinical practice, clinicians routinely integrate and navigate through multiple data by identifying regions and anatomical structures present in any subject. In practical terms, they mentally perform a co-registration, based on physiological landmarks common to all subjects, assigning the same parameters to anatomically equivalent points. A coordinate system based on anatomical or functional landmarks can mimic the natural clinical language used to describe anatomical structures and will allow an accurate positioning in the anatomy of each subject regardless of the imaging modality.

The assignment of surface coordinate systems defining regular meshes was originally employed in the area of computer graphics [106, 104, 14]. Most of these methods are based on harmonic functions producing conformal (angle preserving) coordinate systems. While these coordinates can be defined in spherical or disk-like shapes, they are difficult to generalize to domains with more complex topology including handles or holes such as toroidal shapes [104]. Because of this, its usage in medical imaging has been limited to organs homomorphic to the sphere like the brain [103, 88]. Additionally, these methods, honoring its computer graphics origins, have been traditionally computed over polygonal mesh domains. This is detrimental to medical imaging techniques: the medical imaging data is defined in discrete voxel domains. Voxel value contains the mean intensity of the organ in the volume defined by the voxel, and this value is heavily linked to organ function. It follows that restricting the coordinate systems to the surface of a polygonal mesh can only encode shape, but no functional information. While shape itself can be an important cue in diagnoses, internal lesions might appear without affecting external shape.

In this chapter we present the following contributions to the field of volumetric parameterization and definition of coordinate systems:

1. a method that extends current harmonic parameterizations to 3D domains and directly works on the discrete voxel image domain the level curves of the pa-

rameterization define a volumetric mesh.

2. a method for correction of unhomogenous coordinates.

Second, our method allows using flexible boundary conditions defined over anatomical structures of complex geometry. Finally our examples illustrate the potential of our methodology to the parameterization of the liver and cochlear anatomy.

4.1 Parameterization via harmonic mapping

A parameterization φ, is a one-to-one map between a manifold $\mathcal{M}$ and a surface $\mathcal{S}$, typically the plane, the disk or sphere.

$$\varphi : \mathcal{M} \to \mathcal{S} \tag{4.1}$$

The parameterization of the manifold onto the surface $\mathcal{S}$ implies that the coordinates that define the surface will need to be stretched or shrink in order to adapt to $\mathcal{M}$ thus introducing distortions on the mapping. According to the distortions that the parameterization induces, they can be classified [28] in:

1. Isometric: a parameterization is called isometric if any arc on $\mathcal{M}$ has the same length on $\mathcal{S}$. The tensor matrix is preserved, i.e. equal length and angle.

2. Conformal: if the angles between any pair of arcs is the same in $\mathcal{M}$ and $\mathcal{S}$, the parameterization is called conformal, or angle preserving.

3. Equiareal: when any patch of $\mathcal{M}$ has the same area in $\mathcal{S}$, then the parameterization is called equiareal.

Additionally a parameterization is isometric if and only if is also conformal and equiareal. However, even if ideally isometric parameterizations are highly desirable as they maintain length, angle and area, they can only be obtained in a very reduced subset of cases such as the mapping of the cylinder to the plane. So in many practical cases, one might want to obtain conformal or equiareal maps.

Considering for the sake of simplicity the case of a conformal map of a planar region into the plane, we can express the parameterization as a function of complex variable $w = f(z)$. The function f is analytic in a neighborhood around a point z and $f'(z) \neq 0$. Then f satisfies the Cauchy-Riemann equations with $z = x + iy$ and $w = u + iv$:

$$\frac{\partial u}{\partial x} = \frac{\partial v}{\partial y}, \frac{\partial u}{\partial y} = -\frac{\partial v}{\partial x} \tag{4.2}$$

By differentiating equations 4.2 by x and v we obtain the Laplace equations

$$\Delta u = 0, \Delta v = 0 \tag{4.3}$$

with Δ being the Laplacian operator

$$\frac{\partial^2}{\partial x^2} + \frac{\partial^2}{\partial y^2} \tag{4.4}$$

Any parameterization satisfying this Laplace equations and is of class C^2 is called an harmonic mapping. Since by definition conformal parameterizations satisfy equations 4.2, a conformal map is also an harmonic map. Harmonic maps have the advantage that can be efficiently computed by solving the elliptical Partial Differential Equations (PDE) for u and v and by the Radó-Knesser-Choquet theorem [52] it is guaranteed to be a one-to-one map if mapped to a convex regions.

Equation 4.3 plays fundamental roles in physics and many engineering problems as it's also the steady-state solution of the heat diffusion problem. The heat equation governs the propagation of heat u over time in a material with thermal diffusivity α:

$$\frac{\partial u}{\partial t} - \alpha \Delta u = 0 \tag{4.5}$$

For some problems its best to where enough time has passed, heat has reached an equilibrium state and the thermal conductivity is not relevant ($\alpha = 1$), we obtain the steady-state equation of heat, the Laplace equation 4.3. Functions u that are solution of the Laplace equation, are called Harmonic functions.

It follows that computing a parameterization from a manifold to a convex region can be reduced to solve a heat diffusion problem. In the diffusion problem, heat values will represent the coordinate values assigned to the object. Properties of harmonic functions will ensure that our coordinate systems will be generated by smooth, twice differentiable functions. Harmonic maps can be defined also over arbitrary Riemann manifolds, by means of the generalized Laplacian operator, and resulting harmonic functions preserve many properties of the harmonic functions in Euclidean spaces.

4.1.1 Heat equation over discrete volumetric shapes

As we have seen, heat equation elliptic PDEs with specific boundary conditions are a powerful tool for defining coordinate systems. Boundary Conditions (BC) take the form of constrained heat values at specified points (Dirichlet BC) , or constrained fixed values of a partial derivative at a point (Neumann BC). Dirichlet conditions constrain the values of heat (coordinate values) at some specific sites, which will be extended by the heat equation to the whole domain. This allows to write generic procedures for the computation of coordinates. Given that different boundary conditions imply completely different coordinate mappings, their setting is crucial for getting a suitable parameterization of the anatomy. The careful placing of boundary conditions in anatomical landmarks can provide the parameterization with anatomical and/or functional information as well.

Anatomical parametric mappings solve the Laplacian:

$$\Delta u = 0 \quad u_{|\mathcal{A}} = f \tag{4.6}$$

for $f = f(x, y, z)$ the coordinate values defined at anatomical specific sites $\mathcal{A}$ that have to be extended to the whole anatomical volume.

All the voxels on a binary image segmentation will constitute the domain Ω where the coordinate system will be applied. By applying the Laplace discrete operator to all image voxels, equation (4.6) can be written in matrix form as $Au = 0$. The matrix A, called graph Laplacian or adjacency matrix, encodes the neighboring relations
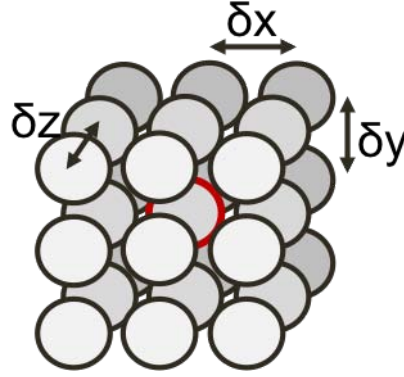
Figure 4.1: Discrete voxel lattice. Central Voxel highlighted in red. Neighbors in x, y and z axis are at distances $\delta x, \delta y, \delta z$ respectively.

between voxels that encode the discrete laplacian operator. In the voxel image lattice (see Fig. 4.1), we can approximate the discrete Laplacian by computing the second order finite differences:

$$\Delta = \partial_{xx} + \partial_{yy} + \partial_{zz} =$$
$$\frac{u_{i+1,j,k} - 2u_{i,j,k} + u_{i-1,j,k}}{\delta x^2} + \frac{u_{i,j+1,k} - 2u_{i,j,k} + u_{i,j-1,k}}{\delta y^2} + \frac{u_{i,j,k+1} - 2u_{i,j,k} + u_{i,j,k-1}}{\delta z^2}$$
$$(4.7)$$

for $u_{i,j,k}$ any voxel in the domain of the binary segmentation Ω.

The graph laplacian A of the domain D corresponding to a binary segmentation can be computed using the following algorithm 1.

> **input** : D=Voxels of the anatomical domain.
> **output**: Adj=Adjacency matrix.
> Adj$\leftarrow$ Empty matrix of $\#D \times \#D$;
> **for** $v : Voxels \in D$ **do**
> $\quad$ **for** $n : Neighbors\ of\ v$ **do**
> $\quad\quad$ | $Adj(v,n) \leftarrow -1$;
> $\quad$ **end**
> $\quad$ $Adj(v,v) \leftarrow \#Neighbors$;
> **end**

Algorithm 1: Computation of adjacency matrix for an anatomical domain D

Boundary conditions are introduced by setting the values of u to specific values at voxels belonging to the anatomical sites $\mathcal{A}$. Those values will act as origin of coordinates and represent the Dirichlet boundary values of our bounday value problem. The solution to the Laplacian with Dirichlet anatomical conditions is obtained by solving

the system of equations $Au = b$, with b being a row matrix encoding the boundary values and computed as shown in 2.

    input : $\mathcal{A}$=Voxels with boundary condition
    input : f=boundary value for each voxel of $\mathcal{A}$
    input : *Adj* graph laplacian matrix
    output: b=b matrix
    $b \leftarrow$ default values according $\mathcal{A}$; **for** *f_i: each different value of f* **do**
        for *v: any voxel with boundary value f_i* **do**
            for *r: rows of b where $Adj(x, v) = -1$ for any x* **do**
                $b[r] \leftarrow b[r] - f_i$;
            end
        end
    end

Algorithm 2: Computation of the b matrix encoding the boundary conditions of the system of equations

It is not uncommon to find CT scans with in plane resolutions of 512x512 and hundreds of slices. A large organ such as the liver will occupy great part of the volume. Using 27-connected neighborhood, the matrix A of a 3D liver can have millions of rows. Although A is sparse by definition, solving the system of equations with standard techniques might be unfeasible (A^{-1} is not generally sparse). Given that A is symmetric and positive definite we can use Preconditioned Conjugate Gradient method using the Incomplete Cholesky Factorization of A as preconditioner [43]. This allows solving the system iteratively in short time and with low memory footprint.

4.2   Anatomical boundary conditions

Coordinate systems defined locally to the anatomy of the organ might be more useful that global image, but their usefulness is heavily dependent of the anatomical places $\mathcal{A}$ used as boundary conditions while solving the PDE. Good selection of $\mathcal{A}$ is a key step into producing useful anatomical coordinate systems. By selecting the proper origins of coordinates, the parameterizations might add further insight in the organ from functional or clinical perspectives.

4.2.1   Hepatic coordinate system

The classification in liver territories given by Couinaud, is not only of high clinical relevance, but reflects also the functional nature of the liver, since it separates the liver into left and right (functional) hemi-livers based on specific landmarks in the liver.

Given that the liver segmentations have no internal holes, the organ is homeomorphic to the sphere. Consequently, we parameterize the volumes using spherical coordinates (latitude, longitude) and adding a third radial or depth coordinate in order to reach the interior points. Boundary conditions are used at specific anatomical
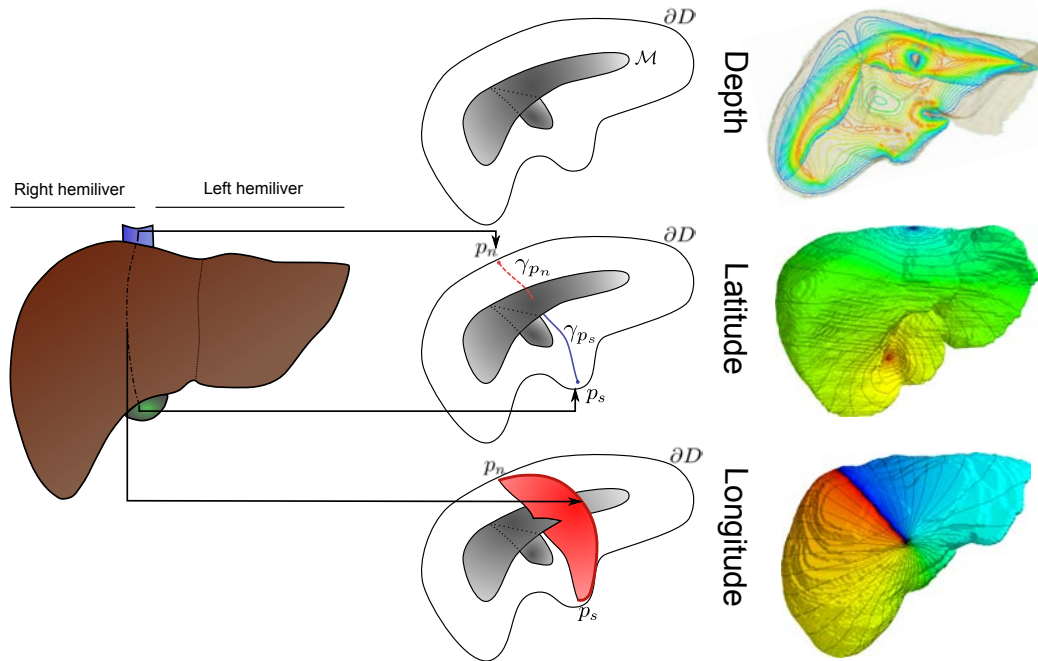
Figure 4.2: Liver boundary conditions for functional parameterization of the three coordinates.

landmarks, with values for latitude coordinates in $\in [-\pi, \pi]$, longitude in the range $\in [0, 2\pi]$ and radial or depth values in the range $\in [0, 1]$.

A main requirement for providing a good reference system for the parameterized liver is to select adequate landmarks as origins of coordinates. Although the liver has some anatomical landmarks, it is often much more useful for clinical applications to consider its functional characterization [21], given by a specific set of landmarks that are related to the functional anatomy. Boundary conditions will be set according to the functional structure of the liver.

For spherical objects, the radial coordinate can be defined from the heat flowing from the volume center of mass to the external boundary. However, for generic shapes, the center of mass is not a good candidate for radial origin of coordinates. Medial surface is the loci of center of maximal spheres bi-tangent to the surface boundary points of the shape [10], and by definition [75], medial surfaces are always located in the center of the object, and they are an excellent candidate from where heat can spread to the surface of the object. We use the method for computation of anatomy-friendly medial surface computation presented in chapter 3. The method generates medial surfaces requiring no pruning and without of extra spurious medial surfaces. These medial surfaces provide good starting point for the radial coordinate.

Let $\mathcal{M}$ be the medial surface and ∂D the anatomical volume boundary. Then, the

Dirichlet conditions for defining the radial coordinate are given by:

$$f(x, y, z) = \begin{cases} 1, & \text{for } (x, y, z) \in \mathcal{M} \\ 0, & \text{for } (x, y, z) \in \partial D \end{cases} \tag{4.8}$$

Boundary voxels are determined by searching voxels of the object that are n-connected to background voxels [62, 75]. The definition of boundary conditions is sketched in the liver scheme of Fig. 4.2 showing in gray a medial surface of a liver schematic anatomy. An example of radial coordinate (D_ϕ) obtained over a liver volume is shown also, with three axial cuts and a color map encoding radial values.

Latitude D_γ is defined along curves radially traversing the volume and joining two separated points (poles) of the volume boundary, p_n, p_s. These two poles can be placed at different points of the surface boundary, ∂D. The specific selection of pole voxels is application dependent, but in general opposite points in the surface give best results. The gradient of the radial map is used to join the two poles p_n and p_s along two curves, $\gamma_{p_n}, \gamma_{p_s}$ that go from each pole to the medial surface. The Dirichlet conditions for defining latitude coordinate are given by:

$$f(x, y, z) = \begin{cases} \pi, & \text{for } (x, y, z) \in \gamma_{p_n} \\ -\pi, & \text{for } (x, y, z) \in \gamma_{p_s} \end{cases} \tag{4.9}$$

In the liver, good candidates for the definition of the poles are the point where the inferior vena cava enters into the liver (north pole) and the gall bladder fossa as south pole. Although not using the *polar* language, Couinaud used the same landmarks to define the separation of the liver into left and right hemiliver. The definition of boundary conditions is sketched in the liver scheme of Fig. 4.2, that shows γ_{p_n} in dashed line and γ_{p_s} in solid one, and the specific landmarks as seen on a CT scan on Fig. 4.3.

Longitude D_ρ spans from an imaginary curve, (a meridian), than runs from pole to pole. The shortest latitude path over ∂D from p_n to p_s may be used. This curve is propagated inwards along the radial gradient until it meets the latitude curves γ_{p_n}, γ_{p_s}, defining a meridian surface, that can be used to define boundary conditions for longitudinal heat propagation.

The meridian surface defines the starting of the longitudinal angular parameter. In order to force periodicity the end value of the longitude is assigned to the the neighbouring voxels lying on the meridian left hand-side. Orientation is defined by the sign of the dot product between the normal vector at the meridian surface and the vector from the current meridian voxel to the next (Fig. 4.4). If we note by MS_+ the meridian surface and by MS_- its left replica, then the Dirichlet conditions for the longitude are given by:

$$f(x, y, z) = \begin{cases} 0, & \text{for } (x, y, z) \in MS_+ \\ 2\pi, & \text{for } (x, y, z) \in MS_- \end{cases} \tag{4.10}$$

In the liver, Cantlie's line is an imaginary line (it is not a physical feature) on the surface of the liver that runs from the inferior vena cava anteriorly to the gall bladder fossa The cantlie line can be tracked using the middle hepatic vein (Fig: 4.5). This line divides the liver into two separated functional hemi-livers. This line will
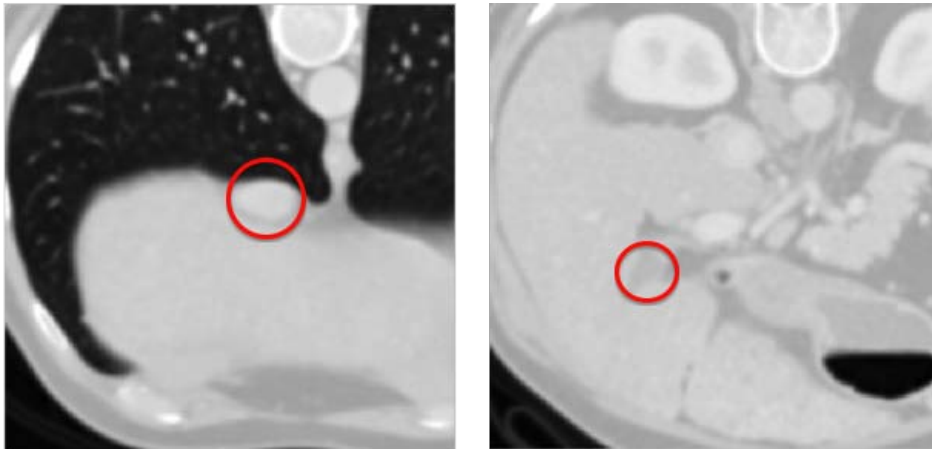
Figure 4.3: Liver boundary conditions for latitude (poles). Left: north pole in the vena cava (red mark). Right: south pole in the gall bladder fossa. The gall bladder is visible as a dark patch inside the red mark.

(a)   (b)
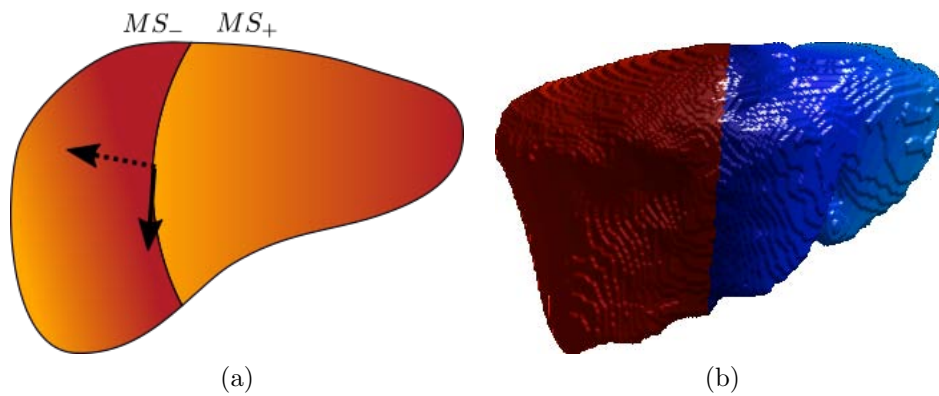
Figure 4.4: Computation of Hemiliver segments and meridian surface. Iinitialization of boundary values for meridian surface. Orientation of voxels defined by vector product of the vector from a voxel of the meridian line to the next (solid vector), and the normal at the surface (dashed vector) (a). Helimiver segments on real liver (b).

Figure 4.5: Liver boundary conditions for longitude (meridian line). The Cantlie line can be tracked by using the middle hepatic vein direction (red arrow)

define the starting meridian for the origin of longitudinal coordinate. The definition of boundary conditions is sketched in th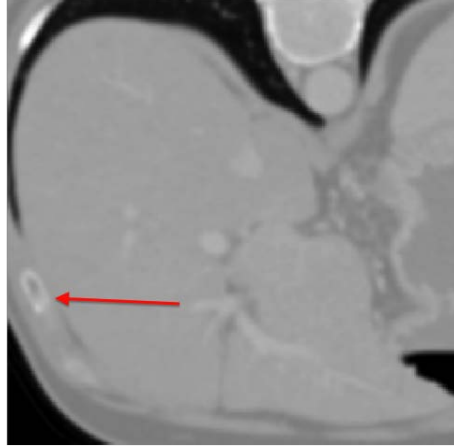e liver scheme of Fig. 4.2 that shows the meridian surface in red. The longitude is over a liver colored using latitude values and showing its level curves.

With this set of boundary conditions, parameterized livers map the functional nature of the liver of different patients. However, the propagation of heat in the latitudinal coordinate requires additional work in order to compensate a effect of the heat propagation with punctual heat sources.

Coordinate distribution inhomogenety

The fundamental solution is the solution to the heat equation corresponding to an initial point source of heat at a known position applied to a single point of known position x_0. The solution is radially symmetric to the point where heat is applied and its described by the expression:

$$\Phi(|x - x_0|) = \begin{cases} \frac{1}{d(d-2)} \frac{1}{|x-x_0|^{(d-2)}} & \text{if } d \geq 3 \\ -\frac{1}{2\pi} \log |x - x_0| & \text{if } d = 2 \end{cases} \tag{4.11}$$

for d the dimensions of the embedding space and $|x|$ the distance from the heat center. The problem solves the case where heat propagates from a single point to a large domain (Fig. 4.6). This case is analogous similar to the propagation of heat on latitudinal propagation where heat only propagates from isolated pole points. This is relevant because the propagation of heat the point changes rapidly changes and the heat at points far from it changes slowly. This a slightly undesirable behavior for the generation of coordinate systems because the level curves of the heat values will accumulate close to the boundary and will be very scarce far from them (see Fig. 4.7).

This is no surprise, since an harmonic map is also a conformal map and as such
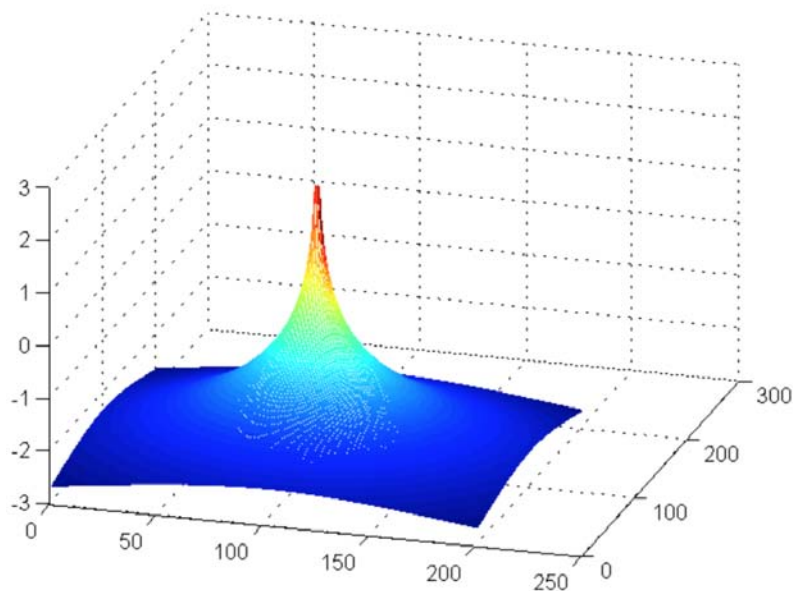
Figure 4.6: Profile of the laplacian fundamental solution in a squared domain

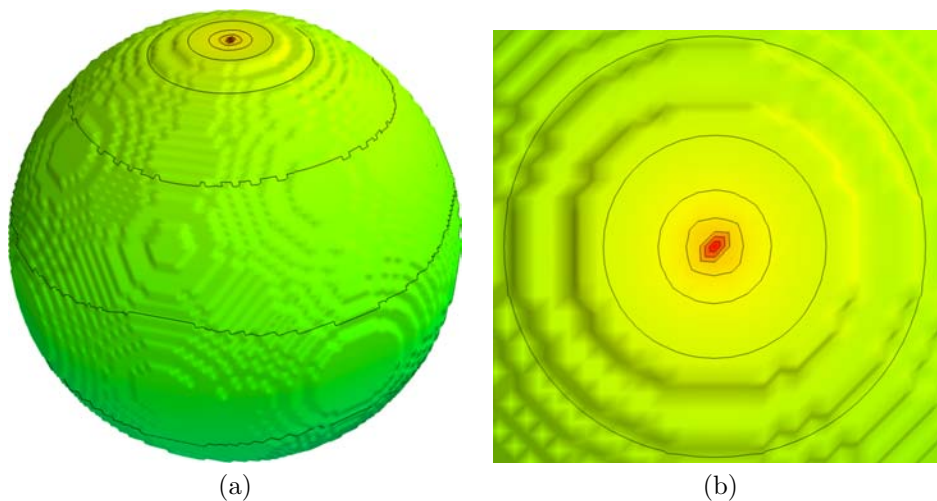(a)   (b)

Figure 4.7: Inhomogenety of level curves result on the propagation of the heat from a single point into a domain. Level curves are abundant near the pole but scarce near the equator (a). Detail of the level curves near the pole (b)

does not conserve areas. However, the slow change of heat values far from the poles might introduce a possible loss of numerical precision on that areas. A increased amount of coordinate information in areas far from punctual heat sources is desirable for better coordinate systems. This problem is silently acknowledged in many other parameterizations methodologies, and in fact many authors compute parameterizations in a two (or more) step process: initial parameterization followed by a posterior process of regularization, either using optimization processes [14], or combining multiple smaller parameterizations [6].

We consider two different methods for coordinate correction in case we find excessively separated level curves. A first approach could be using different boundary values. The simplest prevention method for reduction of inhomogenity reduction is the definition of new boundary values that are different from the fundamental solution. This step might be application dependent and not always applicable.

A second possibility is to use a correction of coordinates in a post process normalization operation. We apply an algebraic normalization to compensate for the high decreasing nature of the heat values near the poles and the plateau values, following the following expression:

$$\phi_{norm} = \frac{e^{(2\phi z_m + z_M)}}{e^{2\phi} + 1} \tag{4.12}$$

for ϕ the latitude values and z_m and z_M the minimum and maximum z values of the object. After the algebraic correction, we perform a re-normalization of the values to the range $[0, 1]$.

We the later option for the normalization of the values of the latitude coordinate, spreading the level curves of the heat distribution more and obtaining better coordinates.

Results

In order to illustrate the flexibility of our volumetric coordinates, we have parameterized four liver segmentation masks from the SLiver07 MICCAI challenge [42]. Liver lobe distributions introduce a complex convexity in their shape that is challenging for any medical application. Examples of the parameterized livers can be seen on Fig. 4.8 a and b. Our radial coordinate agrees with the definition required for medial representations and surface coordinates have been propagated inside volumes parameterizing all depth levels as depicted on Fig. 4.8 c.

Figure 4.9 shows the unwrapping of the outermost layer of the parametric space in a square, with latitude as x-coordinate, longitude as y-coordinate and radial coordinate is set to zero. In this view we can explore the relation of the liver with the surrounding organs such as the rib cage, the lungs and kidneys.

We also show how the organ-centric coordinate system can be used to quantify the variability of the liver segments. According to Couinaud's rules, the fourth segment of the liver can be found between the planes defined by the middle hepatic vein and the left hepatic vein (Fig. 4.10 - a). On the surface of the liver, the segment is limited by the falciform ligament and Cantlie's line. The hemiliver based coordinate system can be used to evaluate the variability in the width of the fourth segment. To that

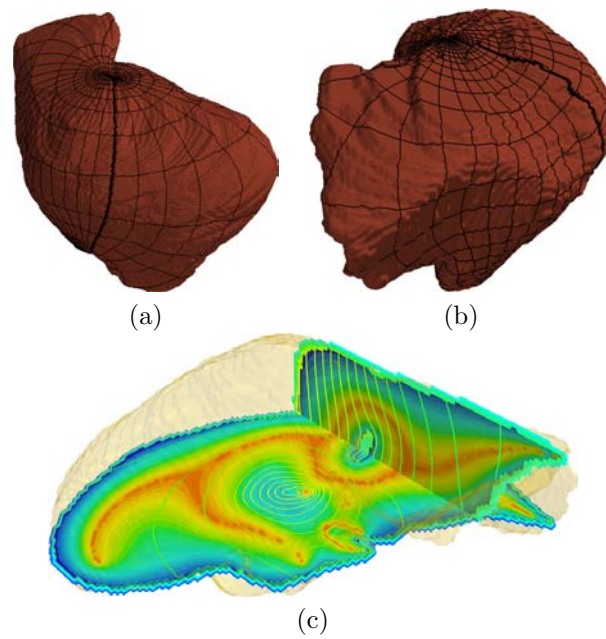(a)   (b)

(c)

Figure 4.8: Liver parameterization. Two livers parameterized (a) and (b). Section of the liver where radial, latitude and longitude are visible inside the volume (c).
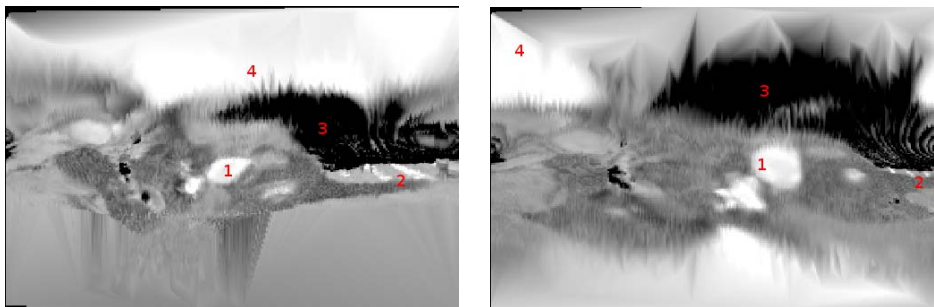

Figure 4.9: Liver unwrapped in parametric space. Vena cava (1), rib cage (2), lung parenchima (3) and kidney (4). visible inside the volume (c).
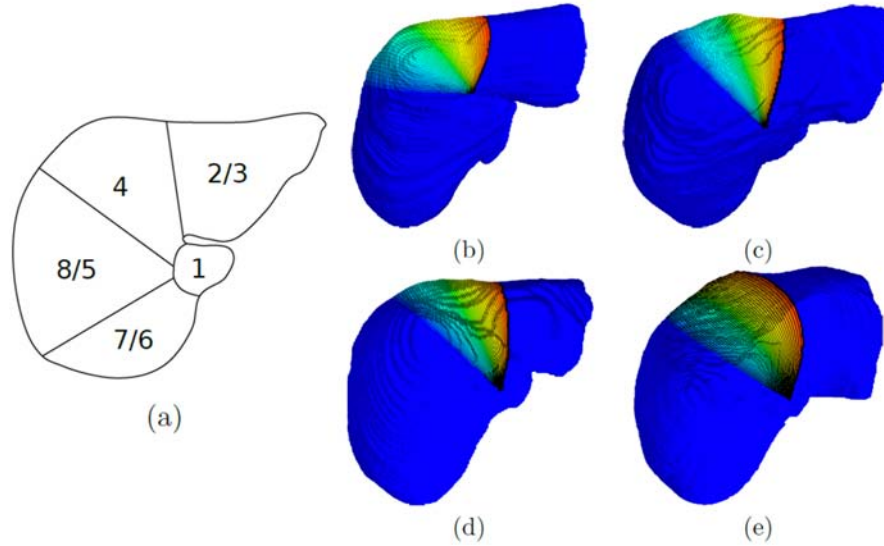
Figure 4.10: Liver segment size comparison: a) top view segment diagram, b) to e) average distance from Cantlie line to falciform ligament.

effect we have measured the longitudinal distance from Cantlie's line to the falciform ligament. The four cases depicted in Fig. 4.10b to Fig. 4.10e show the differences of the fourth segment of the liver. The values of the segment size can be seen on Table 4.1.

Liver	Segment size
Liver 1	2.13 ± 0.27
Liver 2	1.02 ± 0.21
Liver 3	1.01 ± 0.11
Liver 4	1.29 ± 0.10

Table 4.1: Fourth segment sizes (mean longitude along segment boundary)

4.2.2 Cochlear coordinate system

The cochlea is a small structure of the inner ear located in the temporal bone. It is composed of several small chambers (Fig. 4.11 - 5 and 6) filled with liquid and membranes covered in sensorineural (Fig. 4.11 - 2) structures that transform specific auditive frequencies into electrical signals for the brain to interpret.

Cochlear coordinate systems have been proposed in the past: a common cochlear framework can be very useful for evaluation of the cochlear anatomy and positioning of implanted cochlear electrode arrays. It would allow the direct comparison of measures performed within the many areas of cochlear implant research. Verbist et al. [101]

Figure 4.11: High resolution image of the cochlea: spiral ligament (1), basilar membrane (2), spiral lamina ossea (3), modiolus (4), scala timpani (5), scala vestibule (6).
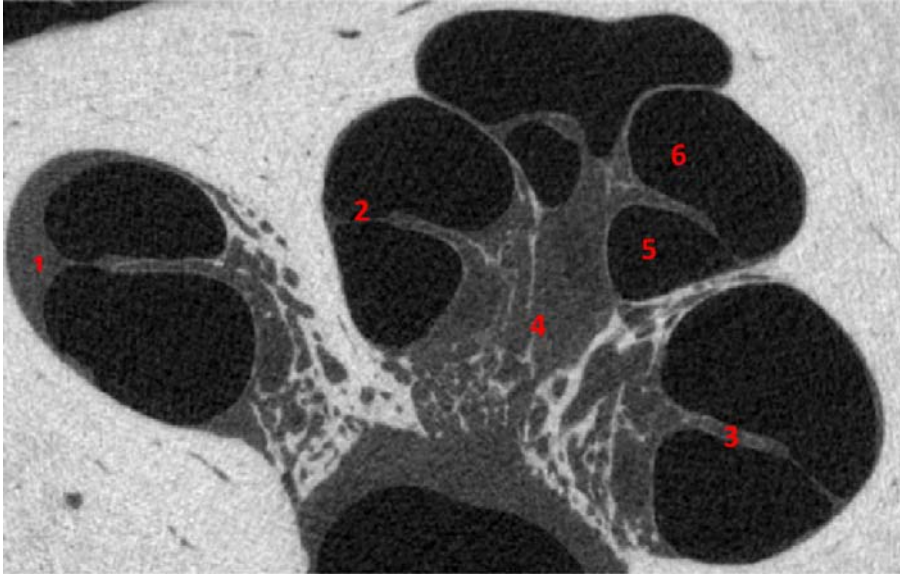
defined a set of anatomical landmarks that are also functionally linked to the way the cochlea transforms frequencies into electrical signals. This cochlear coordinate system is depicted in Figure. 4.12 and is based in a polar coordinate system. A lower "base" plain passes through the basal (wider) turn of the cochlea. A perpendicular vector to that plane that goes through the central part of the cochlea from the base to the apical turn defines the z axis. The distance from any point to the plane along the z axis is the first coordinate. The central part of the round window is the reference angle Θ_{ref} The second coordinate is the rotation Θ along the z axis, from this reference angle. Finally the third coordinate is the (perpendicular) distance ρ from the z axis. However this coordinate system does not apply as a parameterization of the cochlea. Its a conversion from Cartesian coordinates into cochlear-centric polar coordinates. The coordinates cover the inside of the cochlea as well as the outside, so in order to move through the inside of the cochlea you have to change he three components simultaneously. This indeed reduces the usefulness of the polar coordinate system.

By using some set of coordinates that are internal to the cochlea we can improve the previously presented model. The cochlea is a rolled tubular structure, so it is straightforward to use a cylinder-like coordinate system 4.13. However, the cross sectional structure of the cochlea is not a circle. As mentioned before, the cochlea has evolved into a series of separated hollow tubes (*scalae*) that merge at the apex, so the cross section is not a circle. Due to that reason the selected coordinate system for cochlear anatomy will be similar to a cylindrical one but using a medial surface of the cochlear duct instead of a longitudinal axis.

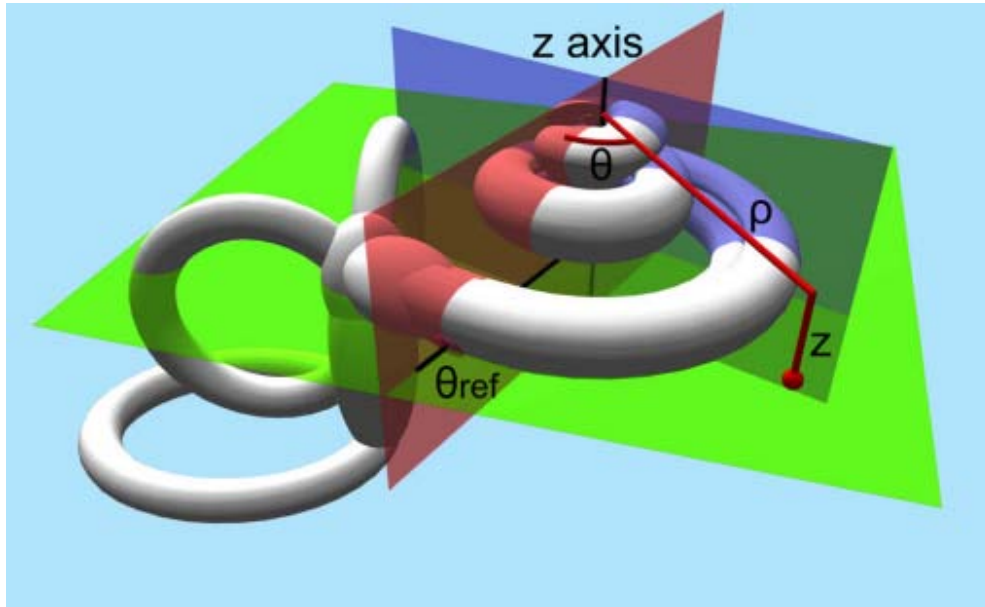Functionally, the cochlea is characterized by the presence of the basilar membrane

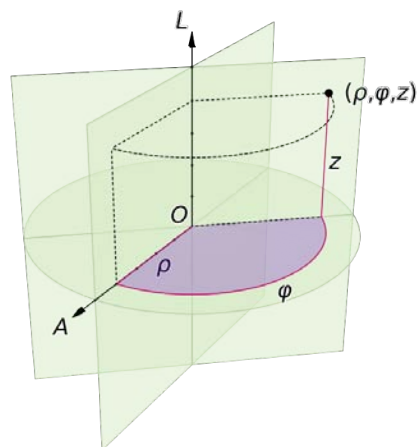**Figure 4.12:** Cochlear coordinate systems presented by Verbist et al.

Figure 4.13: Cylindrical coordinate system: Origin (O), polar axis (A) and longitudinal axis (L) (from wikipedia)

(Fig.4.11-2) along almost all of its length separating two scalae. The basilar membrane is the responsible for the transformation of the sound wave (spatial domain) into the frequency domain. Low frequencies are detected by vibrations of the basilar membrane at the near the apex, while high frequencies stimulate the basilar membrane near the proximal part of the cochlea. However, the preservation of the basilar membrane in cadaveric micro-CT samples is difficult and in many samples, the membrane is absent. It makes more sense to organize the functional parameterization of the cochlea around the lamina spiralis (Fig.4.11-3), a bone structure where the basilar membrane is anchored and that is always present in all subjects.

All things considered, we have all the necessary data to propose a functional cochlea coordinate system. We will reuse the latitude/longitude/depth concepts from the hepatic coordinate system.

Depth coordinate is defined on the same terms as in the case of the liver, given a boundary ∂D and a medial surface of the cochlea $\mathcal{M}$ and its defined by using eq. 4.8.

Latitude is defined as the coordinate spanning from the apex of the cochlea to the basal parts. Since we are interested only in the cochlea, the parameterization has to stop when the cochlea finishes at the vestibule. We can define the north pole p_n as the extreme of the apex, and the south pole p_s as the set of voxels where the cochlea connects with the vestibule. Equation 4.9 describes the Dirichlet boundary conditions for this coordinate. Note that in our formulation, the cochlear latitudinal coordinate is similar to the cylinder longitudinal coordinate. Parameterizing the length of the cochlea the, this latitudinal coordinate matches the frequency functional characteristics of the cochlea.

The definition of the longitudinal cochlear coordinate (or polar axis in cylindrical coordinates), like in the case of the liver, requires the definition of the double meridian line MS_+ and MS_- using the boundary condition values expressed in eq. 4.10. In the case of the cochlea the discontinuity in longitudinal values is set to match the extreme of the spiral lamina. In this way the longitude coordinate allows the differentiation between the different scalae of the cochlea. The delineation of the boundary for the spiral lamina ossea is performed by computing the Gaussian curvature of the segmentation boundary 4.14a. The scala edge is an area of high curvature of the segmentation. The curvature image is used as speed image in a fast-marching algorithm to obtain the highest curvature path between the north pole (apical extreme) and the south pole (round window in the basal area) 4.14b.

A schema depicting the cochlear coordinate systems is shown in in Fig. 4.15. While examples of parameterized cochleas can be seen in Fig. 4.16.

4.3   Discussion

Most of the existing implementations of harmonic mappings in medical imaging restrict to either anatomical surfaces, or the depth coordinate with boundary conditions is given at sites of limited geometric diversity. In this chapter we have presented a flexible method for parameterization and meshing of volumetric anatomical shapes, able to provide a parameterization of the depth coordinate regardless of the volume shape. The possibility of defining flexible organ-centric volumetric meshes providing
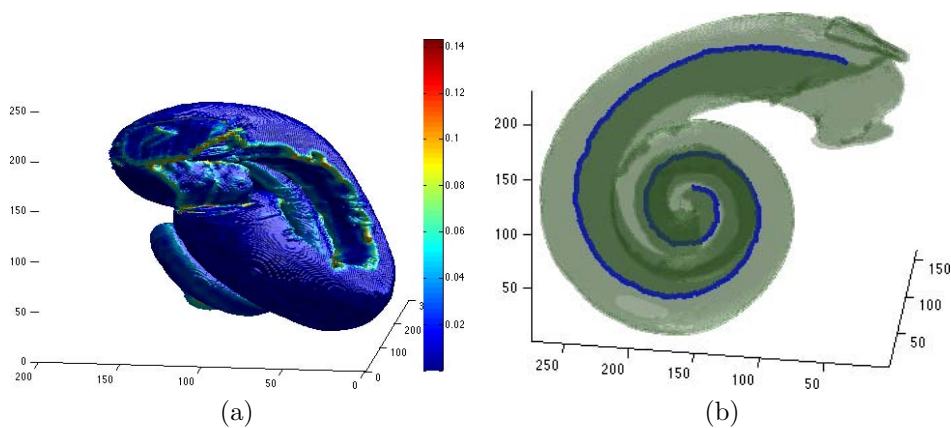
Figure 4.14: Segmentation of the spiral lamina ossea edge for BC of the longitudinal coordinate. Gaussian curvature (a). Highest curvature path (b).
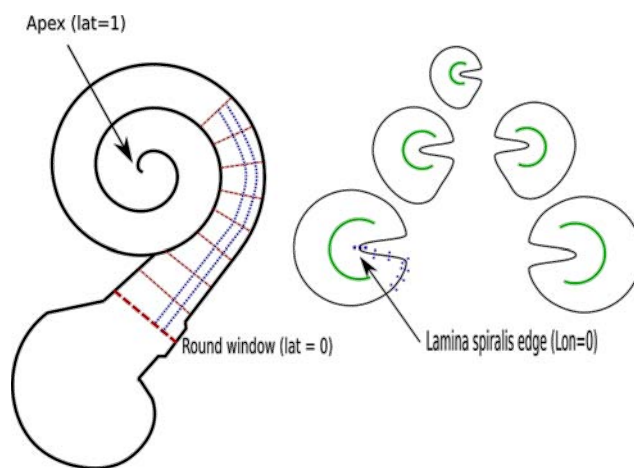
Figure 4.15: Cylindrical coordinate Boundary conditions. Left: top view showing the origin of the latitudinal coordinate (round window and apex). Latitude propagation is shown in red. Right: lateral cut displaying longitude origin at lamina spiralis's edge and longitude propagation (blue). Medial surface is shown in green.
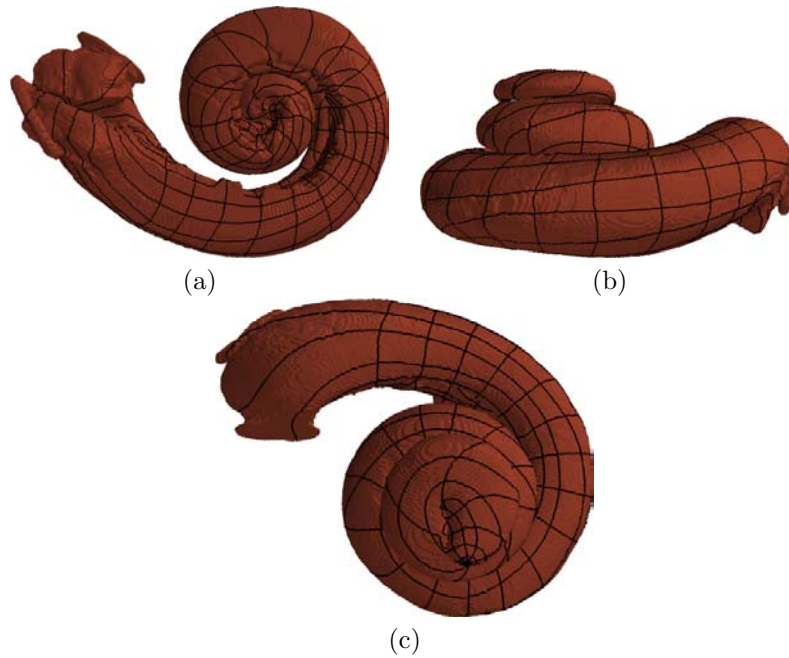
Figure 4.16: Cochlea parameterization. Inferior view (a), Lateral View (b), and top view (c).

coordinate systems will allow analysis of intra-organ structures in a domain-specific framework and comparison of their differences. This scheme also enables the comparison between different patients, even in organs with great variability without the need for explicit registration of images. In this way we propose a common parameterization for the liver anatomy based on the functional hemilivers of the organ. Results suggest a promising potential as a tool for patient specific anatomical modeling. Similarly, other parameterizations can be found for different organs as long as a good set of landmarks can be detected as origin of coordinates.

Chapter 5

Conclusions and Future Work

5.1 Conclusions

The medical literature shows that several organs anatomy can be reinterpreted from specific coordinate systems [21, 101]. Some other works suggest that even during developement the organ follows a specific spatial orientation that can be better described by a organ specific coordinates [77]. With these findings in mind its easy to see that finding automated ways to mimic these coordinate systems in organs can result in improved methods in medical imaging. While many methods try to map the surface of organs as 2D manifolds, only a few tried to tackle the problem of 3D coordinate systems. The jump from 2D to 3D requires a stable coordinate system origin for the third -or depth- coordinate.

It was hypothesized in this thesis that a method capable of provide comparison between organs and localization of tissue had potential to be helpful in many tasks of medical imaging. In order to achieve this goal in a 3D image, we needed three key elements.

- A set of functional or anatomical landmarks for the organ

- A stable origin for the depth coordinate

- A way to properly propagate the coordinate information from the landmarks and depth origin to the whole organ volume

And we provided two working examples of it applied to liver and cochlear anatomy. Our contributions in the field, to achieve these goals were the following:

- **Medial maps for anatomical surfaces** We proposed the organ's medial surface as a good candidate for origin of the depth dimension, but so far, typical methods for generation of medial surfaces in image space (voxel based) were not ideal for this use mainly due to topological issues and vulnerability to boundary noise. Methods based on meshes, while theoretically better were also problematic. We explored some strategies for current medialness energy computation. Our contribution, the GSM2 method, shows a combination of highly desirable

properties as shown on the experiments: bounded, normalized medialness response giving more homogeneous medialness values thanks to the use of structure tensor based ridgedness, and smoother (and hence, more noise resistance) medial manifold generation due to the use or oriented Gaussian operators in the method. GSM2 also has improved signal at self intersecting manifold than other medialness energy map. At the same time, one can actually store shape information on the medial surface and recover the original shape of the object with great degree of detail. The combination of these properties means that the medial manifolds generated are well suited to be used in medical applications.

- **Decoupled binarization of overlapping manifolds** Binarization of medialness maps is a delicate issue for medial manifonds generated by algorithms based on voxel intensities. Most methods use iterative localized euler characterization of a manifold region in the thinning. However, this method has any problems, specifically the high probability of generation of spikes, and other noisy elements due to boundary patterns. The developed medialness map (GSM2) is a smooth operator for medialness but if feeded into a regular binarizator can also produce some noisy manifolds. We used non-maximal suppression as a initial binarization step for the medial map. However, non maximal suppression is based on the computation of the structure tensor of the medialness map. This implies that points where there are two or more manifolds intersecting the binarization response is not well defined. Inspired by the algebraic geometry theory of singularity resolution via blow up of the singularity, we have introduced a branch resolution method (BUM) that binarized the medial surfaces in decoupled space, and our experiments show that not only the results show stability against noise in the boundary of the object is improved but also the reconstruction capability of the method is high. These methods display a good equilibrium between having the capability of defining as much anatomy as possible while being a simple medial surface. All these tests have been performed on both anatomical shapes (livers) and on a database of synthetic shapes created specifically for testing medial manifold methods. The combination of GSM2 + BUM offers a good combination for the generation of medial surfaces in anatomical organs. These, offer a good origin for a depth coordinate in the context of parameterization of the organ.

- **Database and testing protocol for medial manifold validation** We presented a extensive database of synthetic shapes for validation of the behavior of different medial surface generation algorithms. The shapes are organized according to the topology characteristics of the shape. We provide the ground truth medial surface, allowing the computation of *spikeness* metrics while we also provided distorted shapes for the evaluation of the robustness to noise of the methods.

- **3D volumetric coordinate systems** One of the goals of this thesis is the parameterization of organs using a 3D set of newer coordinates. We have developed in the 2 and 3 a method for defining origins of depth coordinates. The other landmarks for the parameterizations will be choosen based on the functional

anatomy of each organ. With this elements we demonstrated the possibility to obtain useful full 3D parameterizations of the anatomy using the Laplacian function for generation of coordinate systems over the shape of the anatomical organ. The introduction of medial surface information improves the parameterization by adding the third (depth) dimension to the coordinate systems, allowing the method to describe also the interior of the object with coordinates, an important goal in the field of medical imaging not often explored by other authors. The Laplacian / heat based formulation for the parameterization is powerful in the sense that it allows to set specific values to specific anatomical or functional landmarks, so that they have the same coordinate in many datasets.

5.2 Future Work

The methods presented in this thesis can be used on many tasks of medical imaging:

- **Multi-Organ Representation Via Medial Surfaces**

  We have barely explored the capabilities of the medial surface representation for the representation of the shape and pose of closely tied organs. The medial surface paradigm captures shape in a detailed but more compact form and can be exploited for describing relations with neighboring organs, specially in cases where the organs are close by and their shape is also influenced by the presence of the surrounding organs, position and shape.

- **Parametric Space Statistical Models**

  Creating a SSM or AAM requires careful selection of landmarks. The different samples need to be aligned before processing in order to remove rotational and scale components to clutter the statistical model. Also, point correspondence has to be maintained through all the samples. Because of this, and specially when dealing with simple shapes with just a few points, points are manually set over the datasets so that they maintain the same order on all the model samples. In the case of complex data, ensuring point correspondence might require registration strategies that as we have seen, are prone to errors, thus inducing unwanted variability in the model. By using our parameterization based on anatomical landmarks, (parametric) point correspondence can be achieved. Also, because the model is 3D volumetric based, image intensity can be added to the model.

  So, using the parametric space instead of the Cartesian coordinates, and adding voxel information just as an additional dimension to each parametric coordinate triplet, we can manage to build statistical models of the whole interior of the organ. Such models would have the possibility to generate new instances of complete volumetric organs and, by using the proper input data, generating models of parenchyma diseases.

- **Parameterization of Other Structures**

  In this thesis we have used the parameterization to generate functional coordinate systems for the liver and the cochlea. However, many more organs can

benefit from this technique. In the brain for instance we can fix specific coordinates to some areas (such as the caudate nucleus or the ventricles) and have the right and left hemisphere immediately identified by the value of one of the coordinates. The technique can target other important organs such as the heart, or other structures such as faces,

- **More Coordinate Smoothing Strategies**

  We have seen that harmonic functions have a tendency to accumulate level curves near fundamental-like boundary condition areas. The method introduced for correction of this behavior could be generalized for other anatomies and or new methods found to spread more evenly the coordinate values.

- **Conventional Registration Using Parametric Information**

  As we have seen, the cochlea is a hollow, rolled tube divided in scalae. While parameterizations can improve our capacity to compare and locate structures in a complex structure such as the cochlea , still many tasks rely on registration techniques. Registration of cochlear segmentation enriched with parametric information and a modified metric to account for the added information has shown improved results in preliminary tests in the apical part of the cochlea.

Bibliography

[1] N. Ahuja and Jen-Hui Chuang. Shape representation using a generalized potential field model. *Pattern Analysis and Machine Intelligence, IEEE Transactions on*, 19(2):169 –176, feb 1997.

[2] Nina Amenta and Marshall Bern. Surface reconstruction by voronoi filtering. *Discrete and Computational Geometry*, 22:481–504, 1998.

[3] Nina Amenta, Sunghee Choi, and Ravi Krishna Kolluri. The power crust, unions of balls, and the medial axis transform. *Computational Geometry: Theory and Applications*, 19(2-3):127–153, 2001.

[4] Nina Amenta and Sunghee et al Choi. The power crust. In *Proceedings of the 6th ACM symp. on Solid modeling and applications*, pages 249–266, 2001.

[5] D. Attali and A. Montanvert. Modeling noise for a better simplification of skeletons. In *ICIP*, pages 13–16, 1996.

[6] G. Auzias, J. Lefevre, A. Le Troter, C. Fischer, M. Perrot, J. Regis, and O. Coulon. Model-driven harmonic parameterization of the cortical surface: Hip-hop. *Medical Imaging, IEEE Transactions on*, 32(5):873–887, May 2013.

[7] Gilles B. A parallel thinning algorithm for medial surfaces. *PR*, 16(9):979–986, 1995.

[8] S. Biedron, M. Westhofen, and J. Ilgner. On the number of turns in human cochleae. *Otology and Neurotology*, 30(3):414–417, 2009.

[9] J. Bigun and G. Granlund. Optimal orientation detection of linear symmetry. In *Proc. of the IEEE 1st International Conference on Computer Vision*, pages 433–438, 1987.

[10] H. Blum. *A transformation for extracting descriptors of shape.* MIT Press, 1967.

[11] G. Bodnár and J. Schicho. Two computational techniques for singularity resolution. *Journal of Symbolic Computation*, 32(1):39–54, 2000.

[12] S. Bouix and K. Siddiqi. Divergence-based medial surfaces. In *ECCV*, pages 603–618, 2000.

[13] Sylvain Bouix, Kaleem Siddiqi, and Allen Tannenbaum. Flux driven automatic centerline extraction. *Med. Image Anal.*, 9(3):209–21, 2005.

[14] C. Brechbühler, G. Gerig, and O. Kübler. Parametrization of closed surfaces for 3-d shape description. *Comp. Vis. Imag. Unders*, 1(61):154–170, 1995.

[15] A. M. Bronstein, M. M. Bronstein, A. M. Bruckstein, and R. Kimmel. Analysis of two-dimensional non-rigid shapes. *Intl. Journal of Computer Vision*, 78(1):67–88, 2008.

[16] J.W. Bruce and P.J. Giblin. *Curves and singularities*. Cambridge Univ. Press, 1992.

[17] J. Canny. A computational approach to edge detection. *PAMI*, 8:679–698, 1986.

[18] F. Chazal and A Lieutier. The λ-medial axi. *Graphical Models*, 67(4):304–331, 2005.

[19] T. F. Cootes, C. J. Taylor, D. H. Cooper, and J. Graham. Active shape models—their training and application. *Comput. Vis. Image Underst.*, 61(1):38–59, January 1995.

[20] Timothy F. Cootes, Gareth J. Edwards, and Christopher J. Taylor. Active appearance models. In *IEEE Transactions on Pattern Analysis and Machine Intelligence*, pages 484–498. Springer, 1998.

[21] C. Couinaud. *Le foie : études anatomiques et chirurgicales*. Masson, Paris, 1957.

[22] Jessica R. Crouch, Stephen M. Pizer, Senior Member, Edward L. Chaney, Yu chi Hu, Gig S. Mageras, and Marco Zaider. Automated Finite-Element analysis for deformable registration of prostate images. *IEEE Trans. on Medical Imaging*, 26(10):1379–1390, oct 2007.

[23] Tamal K. Dey and Wulue Zhao. Approximate medial axis as a voronoi subcomplex. In *Proc. of the seventh ACM symposium on Solid modeling and applications*, pages 356–366, 2002.

[24] M. Eck, T. DeRose, T. Duchamp, H. Hoppe, M. Lounsbery, and W. Stuetzle. Multiresolution analysis of arbitrary meshes. In *Proceedings of the 22Nd Annual Conference on Computer Graphics and Interactive Techniques*, pages 173–182, 1995.

[25] Anders Eklund, Mats Andersson, and Hans Knutsson. fmri analysis on the gpu-possibilities and challenges. *Comput Methods Programs Biomed*, 105(2):145–61, Feb 2012.

[26] JeanH.D. Fasel, PietroE. Majno, and Heinz-Otto Peitgen. Liver segments: an anatomical rationale for explaining inconsistencies with couinauds eight-segment concept. *Surgical and Radiologic Anatomy*, 32(8):761–765, 2010.

[27] P. T. Fletcher and C. Lu et al. Principal Geodesic Analysis for the study of nonlinear statistics of shape. *IEEE Trans. Med. Imag.*, 23(8):995–1005, 2004.

[28] Michael S. Floater and Kai Hormann. Surface parameterization: a tutorial and survey. In *In Advances in Multiresolution for Geometric Modelling*, pages 157–186, 2005.

[29] W.T. Freeman and E.H. Adelson. The design and use of steerable filters. *IEEE Trans. Pattern Analysis and Machine Intelligence*, 13(9):891–906, 1991.

[30] Jaume Garcia, Debora Gil, Luis Badiella, Aura Hernandez-Sabate, Francesc Carreras, Sandra Pujades, and Enric Marti. A normalized framework for the design of feature spaces assessing the left ventricular function. *IEEE Transactions on Medical Imaging*, 29(3):733–745, 2010.

[31] Jaume Garcia, Debora Gil, and Aura Hernandez-Sabate. Endowing canonical geometries to cardiac structures. In *Lecture Notes in Computer Science*, volume 6364, pages 124–133, 2010.

[32] P.J. Giblin, B.B. Kimia, and A.J. Pollitt. Transitions of the 3d medial axis under a one-parameter family of deformations. *IEEE Trans. on Pattern Analysis and Machine Intelligence*, 31(5):900–918, 2009.

[33] J. Giesen, B. Miklos, M. Pauly, and C. Wormser. The scale axis transform. In *SCG*, pages 106–115, 2009.

[34] D. Gil, J. Garcia-Barnes, and A. A. Hernandez. Manifold parametrization of the left ventricle for a statistical modelling of its complete anatomy. In *SPIE*, pages 304–314, 2010.

[35] Debora Gil and Petia Radeva. Extending anisotropic operators to recover smooth shapes. *Comput. Vis. Image Underst.*, 99(1):110–125, July 2005.

[36] J. Gomes and O. Faugeras. Reconciling distance functions and level sets. *Journal of Visual Communication and Image Representation*, 11:209–223, 2000.

[37] R. C. Gonzalez and R. E. Woods, editors. *Digital Image Processing (third edition)*. Addison-Wesley, 1992.

[38] A. Gray. *Tubes*. Birkhäuser, 2004.

[39] X. Gu, Yalin Wang, T.F. Chan, P.M. Thompson, and Shing-Tung Yau. Genus zero surface conformal mapping and its application to brain surface mapping. *Medical Imaging, IEEE Transactions on*, 23(8):949–958, 2004.

[40] R. Haralick. Ridges and valleys on digital images. *CVGIP*, 22(10):28–38, 1983.

[41] H. Hauser. The hironaka theorem on resolution of singularities. *Bull Am Math Soc*, 40(3):323–403, 2003.

[42] T. Heimann and B. van Ginneken et al. Comparison and evaluation of methods for liver segmentation from CT datasets. *IEEE Trans Med Imaging*, 28(8):1251–1265, 2009.

[43] Magnus R. Hestenes and Eduard Stiefel. Methods of Conjugate Gradients for Solving Linear Systems. *Journal of Research of the National Bureau of Standards*, 49:409–436, 1952.

[44] H Hironaka. Resolution of singularities of an algebraic variety over a field of characteristic zero. *Ann. Math.*, 79:109–326, 1964.

[45] Belgihiti J., Clavien PA., Gadzijev, and et al. The brisbane 2000 terminology of hepatic anatomy and resections. *HPB*, 2:333–339, 2000.

[46] J.Hicklin and P.Moler et al. Jama: A java matrix package., 2008.

[47] Tao Ju, Matthew L. Baker, and Wah Chiu. Computing a family of skeletons of volumetric models for shape description. In *Geometric Modeling and Processing*, pages 235–247, 2007.

[48] A. Kelemen, G. Szekely, and G. Gerig. Elastic model-based segmentation of 3d neuroradiological data sets. *Trans. Med. Imaging*, 18:828–839, 1999.

[49] F. Khalifa, A. El-Baz, G. Gimel'farb, and R. Ouseph. Shape-appearance guided level-set deformable model for image segmentation. In *icpr*, 2010.

[50] T. Kiuchi, M. Kasahara, K. Uryuhara, Y. Inomata, S. Uemoto, K. Asonuma, H. Egawa, S. Fujita, M Hayashi, and K. Tanaka. Impact of graft size mismatching on graft prognosis in liver transplantation from living donors. *Transplantation*, 67(2):321–327, 1999.

[51] H.M. Kjer, J. Fagertun, S. Vera, F. Prez, M.A. Gonzlez-Ballester, and R.R. Paulsen. Shape modelling of the inner ear from micro-ct data. In *Shape Symposium 2014*, 1992.

[52] H. Kneser. Lsung der aufgabe. *Jahresbericht der Deutschen Mathematiker-Vereinigung*, 41(35):123–124, 1926.

[53] P. Lamata, S. Niederer, D.Nordsletten, and et al. An accurate, fast and robust method to generate patient-specific cubic hermite meshes. *MedIMa*, 15:801–813, 2011.

[54] L.J. Latecki, R. Lakamper, and T. Eckhardt. Shape descriptors for non-rigid shapes with a single closed contour. In *Computer Vision and Pattern Recognition, 2000. Proceedings. IEEE Conference on*, volume 1, pages 424–429, 2000.

[55] Tony Lindeberg. Feature detection with automatic scale selection. *IJCV*, 30(2):79–116, 1998.

[56] Xiaofeng Liu, Marius G. Linguraru, Jianhua Yao, and RonaldM. Summers. Organ pose distribution model and an MAP framework for automated abdominal multi-organ localization. In *Medical Imaging and Augmented Reality, Lecture Notes in Computer Science*, volume 6326, pages 393–402, 2010.

[57] LL.Dinguraru and J.A.Pura et al. Multi-organ segmentation from multi-phase abdominal CT via 4D graphs using enhancement, shape and location optimization. In *MICCAI*, volume 13, pages 89–96, 2010.

[58] C. Lo, S. Fan, C. Liu, J. Chan, B. Lam, G. Lau, and J. Wei, W.and Wong. Minimum graft size for successful living donor liver transplantation. *Transplantation*, 68(8):1112–1116, 1999.

[59] A.M. Lopez, F. Lumbreras, J. Serrat, and J.J. Villanueva. Evaluation of methods for ridge and valley detection. *IEEE Trans. Pattern Analysis and Machine Intelligence*, 21(4):327–335, 1999.

[60] J. Maillot, H. Yahia, and A. Verroust. Interactive texture mapping. In *Proceedings of the 20th Annual Conference on Computer Graphics and Interactive Techniques*, pages 27–34, 1993.

[61] J.B.Antoine Maintz and Max A. Viergever. A survey of medical image registration. *Medical Image Analysis*, 2(1):1 – 36, 1998.

[62] G. Malandain, G. Bertrand, and N. Ayache. Topological segmentation of discrete surfaces. *International Journal of Computer Vision*, 10(2):183–197, 1993.

[63] G. Malandain and S. Fernández-Vidal. Euclidean skeletons. *Image and Vision Computing*, 16(5):317–327, 1998.

[64] T. Martin and E. Cohen. Volumetric parameterization of complex objects by respecting multiple materials. In *Shape Modelling International (SMI) Conference*, pages 187–197, 2010.

[65] S. Mitchell, Johan Bosch, Boudewijn Lelieveldt, Jon van der Geest, Johan Reiber, and Milan Sonka. 3-D active appearance models: Segmentation of cardiac MR and ultrasound images. *IEEE TRANSACTIONS ON MEDICAL IMAGING*, 21(9):1167 – 1178, 2002.

[66] N.Faraj, J.-M. Thiery, and T. Boubekeur. Progressive medial axis filtration. In *SIGGRAPH*, 2013.

[67] R. Ogniewicz and M. Ilg. Voronoi skeletons: Theory and applications. In *CVPR*, pages 63–69, 1992.

[68] Kálmán Palágyi and Attila Kuba. A parallel 3d 12-subiteration thinning algorithm. *Graphical Models and Image Processing*, 61(4):199–221, 1999.

[69] H. Park, P.H. Bland, and C.R Meyer. Construction of an abdominal probabilistic atlas and its application in segmentation. *IEEE Trans Med Imaging*, 22(4):483–92, 2003.

[70] T. Peters and K. Cleary, editors. *Image-Guided Interventions: Technology and Applications*. Springer, 2008.

[71] Stephen M. Pizer, P. Thomas Fletcher, Sarang Joshi, Andrew Thall, James Z. Chen, Yonatan Fridman, Daniel S. Fritsch, A. Graham Gash, John M. Glotzer, Michael R. Jiroutek, Conglin Lu, Keith E. Muller, Gregg Tracton, Paul Yushkevich, and Edward L. Chaney. Deformable M-Reps for 3D medical image segmentation. *Int. Journal on Computer Vision*, 55(2):85–106, 2003.

[72] Stephen M. Pizer, P. Thomas Fletcher, Joshi Sarang, A. G. Gash, J. Stough, A. Thall, Gregg Tracton, and Edward L. Chaney. A method and software for segmentation of anatomic object ensembles by deformable M-Reps. *Medical Physics*, 32(5):1335–1345, 2005.

[73] Gallagher Pryor, Brett Lucey, Sandeep Maddipatla, Chris McClanahan, John Melonakos, Vishwanath Venugopalakrishnan, Krunal Patel, Pavan Yalamanchili, and James Malcolm. High-level GPU computing with jacket for MATLAB and C/C++. In *Proceedings of SPIE - The International Society for Optical Engineering*, pages 806005–806005–6, 2011.

[74] C. Pudney. Distance-ordered homotopic thinning: A skeletonization algorithm for 3D digital images. *Computer Vision and Image Understanding*, 72(2):404–13, 1998.

[75] C. Pudney. Distance-ordered homotopic thinning: A skeletonization algorithm for 3D digital images. *Comp. Vis. Imag. Underst.*, 72(2):404–13, 1998.

[76] Casero R., Burton R.A.B., Quinn T.A., Bollensdorff C., Hales P., Schneider J.E., Kohl P., and Grau V. Towards high-resolution cardiac atlases: ventricular anatomy descriptors for a standardized reference frame. In *Statistical Atlases and Computational Models of the Heart, First International Workshop, STACOM 2010, and Cardiac Electrophysiological Simulation Challenge, CESC 2010, Held in Conjunction with MICCAI 2010*, pages 75–84, Beijing, China, 2010.

[77] J. Regis, Mangin J.F., T. Ochiai, V. Frouin, D. Riviere, A. Cachia, M. Tamura, and Samson. Y. Sulcal root generic model: a hypothesis to overcome the variability of the human cortex folding patterns. *Neurologia medico-chirurgica*, 45(1):1–17, 2005.

[78] M. Reyes and M.A. González Ballester et al. Anatomical variability of organs via principal factor analysis from the construction of an abdominal probabilistic atlas. In *ISBI*, pages 682–685, 2009.

[79] Nadathur Satish, Mark Harris, and Michael Garland. Designing efficient sorting algorithms for manycore GPUs. In *Intern. Symp. on Parallel and Distributed Processing*, pages 1–10, 2009.

[80] William J. Schroeder, Jonathan A. Zarge, and William E. Lorensen. Decimation of triangle meshes. In *Computer Graphics (SIGGRAPH '92 Proceedings*, pages 65–70, 1992.

[81] Damian J. Sheehy, Cecil G. Armstrong, and Desmond J. Robinson. Shape description by medial surface construction. *IEEE Transactions on Visualization and Computer Graphics*, 2:62–72, 1996.

[82] J. Shi and C. Tomasi. Good features to track. In *Proceedings CVPR '94., 1994 IEEE Computer Society Conference on*, pages 593–600, 1994.

[83] Kaleem Siddiqi, Sylvain Bouix, Allen Tannenbaum, and Steven W. Zucker. Hamilton-Jacobi skeletons. *Int. Journal Computer Vision*, 48(3):215–231, 2002.

[84] Kaleem Siddiqi, Juan Zhang, Diego Macrini, Ali Shokoufandeh, Sylvain Bouix, and Sven Dickinson. Retrieving articulated 3-d models using medial surfaces. *Machine Vision and Applications*, 19(4):261–275, 2008.

[85] M. Spivak. *A Comprehensive Introduction to Differential Geometry (3rd Edition)*. Publish or Perish, 1999.

[86] M. Spivak. *A Comprehensive Introduction to Differential Geometry, vol. 1*. Publish or Perish, Inc, 1999.

[87] Joshua V. Stough, Robert E. Broadhurst, Stephen M. Pizer, and Edward L. Chaney. Regional appearance in deformable model segmentation. In *Proc. of the 20th int. conf. on Information processing in medical imaging*, volume 4584, pages 532–543, 2007.

[88] M. Styner and G. et al Gerig. Statistical shape analysis of neuroanatomical structures based on medial models. *Med Image Anal.*, 7(3):207–220, 09 2003.

[89] M. Styner and J. A. et al Lieberman. Boundary and medial shape analysis of the hippocampus in schizophrenia. *MIA*, 8(3):197–203, 2004.

[90] H. Sun and A. F. Frangi et al. Automatic cardiac mri segmentation using a biventricular deformable medial model. In *MICCAI*, volume 6361, pages 468–475. Springer, 2010.

[91] H. Sun, A. F. Frangi, H. Wang, and et al. Automatic cardiac mri segmentation using a biventricular deformable medial model. In *MICCAI*, volume 6361, pages 468–475. Springer, 2010.

[92] Hui Sun, Brian B. Avants, Alejandro F. Frangi, Federico Sukno, James C. Gee, and Paul A. Yushkevich. Cardiac medial modeling and time-course heart wall thickness analysis. In *MICCAI Lecture Notes on Computer Science*, volume 5242, pages 766–773, 2008.

[93] Hui Sun, AlejandroF. Frangi, Hongzhi Wang, FedericoM. Sukno, Catalina Tobon-Gomez, and Paul A. Yushkevich. Automatic cardiac mri segmentation using a biventricular deformable medial model. In *MICCAI 2010*, volume 6361 of *LNCS*, pages 468–475, 2010.

[94] Stina Svensson, Ingela Nyström, and Gabriella Sanniti di Baja. Curve skeletonization of surface-like objects in 3d images guided by voxel classification. *Pattern Recognition Letters*, 23(12):1419–1426, 2002.

[95] T. Terriberry and G. Gerig. A continuous 3-d medial shape model with branching. In *1st MICCAI Workshop on Mathematical Foundations of Computational Anatomy: Geometrical, Statistical and Registration Methods for Modeling Biological Shape Variability*, 2006.

[96] James T. Todd. The visual perception of 3d shape. In *Trends in Cognitive Science*, pages 115–125. Elsevier, 2004.

[97] S. Vera, M. A. González Ballester, and D. Gil. A medial map capturing the essential geometry of organs. In *Proceedings of ISBI*. IEEE, 2012.

[98] Sergio Vera, Debora Gil, Agnés Borràs, Marius G. Linguraru, and Miguel A. González Ballester. Geometric steerable medial maps. *Machine Visions and Applications*, in press.

[99] Sergio Vera, Debora Gil, Agnès Borràs, Xavi Sánchez, Frederic Pérez, Marius George Linguraru, and Miguel A. González Ballester. Computation and evaluation of medial surfaces for shape representation of abdominal organs. In *Lecture Notes on Computer Science*. Springer, 2010.

[100] Sergio Vera and Miguel A. et al González. Optimal medial surface generation for anatomical volume representations. In *Lecture Notes on Computer Science*, volume 7601, pages 265–273, 2012.

[101] Berit M Verbist, Margaret W Skinner, Lawrence T Cohen, Patricia A Leake, Chris James, Colette Boëx, Timothy A Holden, Charles C Finley, Peter S Roland, J Thomas Roland, Matt Haller, Jim F Patrick, Claude N Jolly, Mike A Faltys, Jeroen J Briaire, and Johan H M Frijns. Consensus panel on a cochlear coordinate system applicable in histologic, physiologic, and radiologic studies of the human cochlea. *Otol Neurotol*, 31(5):722–30, 2010.

[102] Yalin Wang, Xianfeng Gu, Kiralee M. Hayashi, Tony F. Chan, Paul M. Thompson, and Shing-Tung Yau. Brain surface parameterization using riemann surface structure. In *Proce. of the 8th international conference on Medical image computing and computer-assisted intervention*, MICCAI'05, pages 657–665, 2005.

[103] Yalin Wang, Xianfeng Gu, Paul M Thompson, and Shing-Tung Yau. 3D harmonic mapping and tetrahedral meshing of brain imaging data. In *Proceeding of Medical Imaging Computing and Computer Assisted Intervention (MICCAI), St. Malo, France*, 2004.

[104] Xianfeng David Gu Wei Zeng, Jing Hua. Symmetric conformal mapping for surface matching and registration. *International Journal of CAD/CAM*, 1(9):103–109, 2009.

[105] F. Wilcoxon. Individual comparisons by ranking methods. *Biometrics Bulletin*, 1(6):80–83, 1945.

[106] S-T. Yau X. Gu. Global conformal surface parametrization. In *Proceedings of the 2003 Eurographics/ACM SIGGRAPH Symposium on Geometry Processing*, pages 127–137, 2003.

[107] Huanhuan Xu, Wuyi Yu, Shiyuan Gu, and Xin Li. Biharmonic volumetric mapping using fundamental solutions. *IEEE Transactions on Visualization and Computer Graphics*, 19(5):787–798, 2013.

[108] J. Yao and R.M. Summers. Statistical location model for abdominal organ localization. In *Med Image Comput Comput Assist Interv*, volume 12(Pt 2), pages 9–17, 2009.

[109] P.A. Yushkevich. Continuous medial representation of brain structures using the biharmonic PDE. *NeuroImage*, 45(1):99–110, 2009.

[110] P.A. Yushkevich, H. Zhang, and J.C. Gee. Continuous medial representation for anatomical structures. *IEEE Trans. Medical Imaging*, 25(12):1547–64, 2006.

[111] PaulA. Yushkevich, Hui Zhang, TonyJ. Simon, and James C. Gee. Structure-specific statistical mapping of white matter tracts. *NeuroImage*, 41(2):448–461, 2008.

[112] Barbara Zitov and Jan Flusser. Image registration methods: a survey. *Image and Vision Computing*, 21(11):977 – 1000, 2003.

Publications

Journals

- D. Gil, **S. Vera**, A. Borràs, A. Andaluz and M. A. González Ballester. Efficient Computation of Medial Surfaces Including Resolution of Branching Singularities. Submitted to *Medical Image Analysis.*

- K. Rhode, P. Bhagirath, P. Claus, Z. Chen, Z. Karimaghaloo, Hyon-Mok Sohn, L. Lara Rodriguez, **S. Vera**, X. Albà, A. Hennemuth, H. Peitgen, T. Arbel, M. A. González Ballester, A. Frangi, M. Götte, R. Razavi, T. Schaeffter and R. Karim. Evaluation of state-of-the-art segmentation algorithms for left ventricle infarct from Late Gadolinium Enhancement MR images. Submitted to *Medical Image Analysis.*

- H.M. Kjer, J. Fagertun, **S. Vera**, D. Gil, M. A. González Ballester and R.R. Paulsen. Free-form image registration of human cochlear CT data using skeleton similarity as anatomical prior. *Pattern Recognition Letters Special Iissue on Skeleton Methods and Applications*, 2015.

- **S. Vera**, D. Gil, A. Borràs, M. Linguraru and M.A. González Ballester. Geometric steerable medial maps. *Machine vision and applications*, 24 (6), 1255-1266, 2013.

- F. Perez, J. Huguet, R. Aguilar, L. Lara, I. Larrabide, M. C. Villa-Uriol, J. Lpez, J. M. Macho, A. Rigo, J. Rossell, **S. Vera**, E. Vivas, J. Fernndez, A. Arbona, A. Frangi, J. Herrero Jover, and M. A. Gonzlez Ballester. RADStation3G: A platform for cardiovascular image analysis integrating PACS, 3D+t visualization and grid computing. *Computer Methods and Programs in Biomedicine*, 110(3):399-410, 2012.

- **S. Vera**, D. Gil, A. Lopez and M. A. González Ballester. Multilocal Creaseness Measure. *Insight Journal. 01/2012; 2012 January-December.*

Conference Proceedings

- H. M. Kjer, **S. Vera**, J. Fagertun, M. A. Gonzlez-Ballester, R. R. Paulsen. Predicting Detailed Inner Ear Anatomy from Clinical Pre-Op CT. *Proceedings of CARS 2015.*

- N. Mangado, M. Ceresa, N. Duchateau, H. Dejea, H. M. Kjer, R. R. Paulsen, **S. Vera**, P. Mistrik, J. Herrero, M. A. Gonzlez Ballester. Automatic Generation of a Computational Model for Monopolar Stimulation of Cochlear Implants. *Proceedings of CARS 2015.*

- N. Mangado, N. Duchateau, M. Ceresa, H. M. Kjer, **S. Vera**, P. Mistrik, J. Herrero, M. A. Gonzlez Ballester. Patient-Specific Virtual Insertion of Electrode Array for Electrical Simulations of Cochlear Implants. *Proceedings of CARS 2015.*

- **S. Vera**, M. A. Gonzlez Ballester. D. Gil. A Novel Cochlear Reference Frame Based on the Laplace Equation. *Proceedings of CARS 2015.*

- E. Ruiz, H. M. Kjer, **S. Vera**, M. Ceresa, R. Paulsen. M. A. Gonzlez-Ballester. Random Walks with Shape Prior for Cochlea Segmentation. *Proceedings of CARS 2015.*

- N. Duchateau, N. Mangado, M. Ceresa, P. Mistrik, **S. Vera**, M. A. Gonzlez-Ballester. Virtual Cochlear Electrode Insertion via Parallel Transport Frame. *Proceedings of ISBI 2015.*

- **S. Vera**, F. Perez, C. Balust, R. Trueba, R. Calvo, X. Mazaira, A. Danasingh, L. Barazzetti, M. Reyes, M. Ceresa, J. Fagertum, H. M. Kjer, R. Paulsen, M. A. González Ballester. Patient Specific Simulation for Planning of Cochlear Implantation Surgery. *MICCAI 2014, Workshop on Clinical Image-based Procedures: Translational Research in Medical Imaging.*

- J. Cerrolaza, **S. Vera**, A. Bagué, M. Ceresa, P. Migliorelli, M. Linguraru and M. A. González Ballester. Hierarchical Shape Modeling Of The Cochlea And Surrounding Risk Structures For Minimally Invasive Cochlear Implant Surgery. *MICCAI 2014, Workshop on Clinical Image-based Procedures: Translational Research in Medical Imaging.*

- M. Ceresa, N. Mangado, H. Dejea, N. Carranza, P. Mistrik, H. M. Kjer, **S. Vera**, R. Paulsen and M. A. González Ballester. Patient-Specific Simulation of Implant Placement and Function for Cochlear Implantation Surgery Planning . *MICCAI 2014.*

- H. M Kjer, J. Fagertun, **S. Vera**, M. A. González Ballester and R. Paulsen. Shape Modelling of the inner ear from micro-CT data. *Shape 2014: Symposium on Statistical Shape Models and Applications.*

- **S. Vera**, M. A. González Ballester and D. Gil. Anatomical parameterization for volumetric meshing of the liver *SPIE Medical Imaging 2014.*

- M. Ares, S. Royo, J. Vidal, L. Campderrós, D. Panyella, F. Perez, **S. Vera** and M. A. González Ballester. 3D Scanning System for In-Vivo Imaging of Human Body. *Fringe 2013.*

- **S. Vera**, M. A. González Ballester and D. Gil. Volumetric Anatomical Parameterization and Meshing for Inter-patient Liver Coordinate System Definition. *MICCAI 2013, Workshop on Mesh Processing in Medical Image Analysis 2013.*

- F. Perez, **S. Vera**, G. Fernandez-Esparrach, H. Córdova, R. San José , J. Herrero and M. A. González Ballester. Surgical Workflow Analysis, Design and Development of an Image-Based Navigation System for Endoscopic interventions *MICCAI 2013, Workshop on Clinical Image-based Procedures: Translational Research in Medical Imaging.*

- M. Ceresa, F. Perez, **S. Vera**, N. Carranza, J. Herrero Jover, P. Mistrik and M. A. Gonzalez Ballester. Functional simulation of the cochlea for implant optimization. *IEEE EMBC 2013.*

- **S. Vera**, F. Perez, L. Lara, M. Ceresa, N. Carranza, J. Herrero Jover and M. A González Ballester. Automated annotation removal in agar plates. *IEEE EMBC 2013.*

- A. Borràs, D. Gil, **S. Vera** and M. A. González Ballester. A Validation Benchmark for Assessment of Medial Surface Quality for Medical Applications. *ICVS 2013.*

- L. Lara, **S. Vera**, F. Perez, N. Lanconelli, R. Morisi, B. Donini, D. Turco, C. Corsi, C. Lamberti, G. Gavidia, M. Bordone, E. Soudah, N. Curzen, J. Rosengarten, J. Morgan, J. Herrero and M. A. González Ballester. Supervised Learning Modelization and Segmentation of Cardiac Scar in Delayed Enhanced MRI. *MICCAI 2012, Workshop on Statistical Atlases and Computational Modeling of the Heart.*

- **S. Vera**, D. Gil, A. Borràs, X. Sánchez, F. Perez, M. Linguraru, M. A González Ballester. Computation and evaluation of medial surfaces for shape representation of abdominal organs. *MICCAI 2012, Workshop on Abdominal Imaging. Computational and Clinical Applications.*

- F. Perez, **S. Vera**, L. Lara, M. Ares, S. Royo, L. Campderrós, D. Panyella, J. Herrero and M. A González. Quantitative Evaluation of the Effectiveness of Cosmetic Treatments and Aesthetic Surgical Interventions. *CARS 2012.*

- L. Lara, **S. Vera**, F. Perez, N. Lanconelli, R. Morisi, M. Bordone, G. Gavidia, E. Soduah, N. Curzen, J. Herrero and M. A. González. Cardiac Scar Detection, Segmentation and Quantification in MRI Images for ICD Treatment Planning. *CARS 2012.*

- **S. Vera**, M. A. González and D. Gil. A medial map capturing the essential geometry of organs. *ISBI 2012.*

- **S. Vera**, M. A. González, M. Linguraru and D. Gil. Optimal Medial Surface Generation for Anatomical Volume Representations. *MICCAI 2011, Workshop on Abdominal Imaging. Computational and Clinical Applications.*

Projects

- Fisiologica (Plan Nacional): Integration of anatomical and functional data using normalised coordinate maps based on physiological landmarks.

- HEAR-EU (FP7): High resolution statistical models of the cochlea for improvement of cochlear implantation surgery.

- CHIRON (Artemis): Integrated Healthcare approach for home, mobile and clinical environments.

- Care4Me (ITEA): Increase quality and productivity in the healthcare cycle by using advanced medical imaging and decision support methods while combining them with different knowledge sources.

- MICROACC1O (ACC1Ó): Development of an hardware / software Automated counter of bacterial colony formation units in agar plates.

- 3DI (ACC1Ó): Development of a hardware/software of a 3D color camera for plastic surgery and cosmetics.